AD-A077 712 CALSPAN ADVANCED TECHNOLOGY CENTER BUFFALO NY AERODYN--ETC F/G 21/5
AERODYNAMIC AND ACOUSTIC INVESTIGATIONS OF AXIAL FLOW FAN AND C--ETC(U)
AUG 79 G F HOMICZ , J A LORDI , G R LUDWIG F33615-76-C-2092
UNCLASSIFIED CALSPAN-XE-5933-A-103 AFAPL-TR-79-2061 NL

1 OF 2
AD A077712

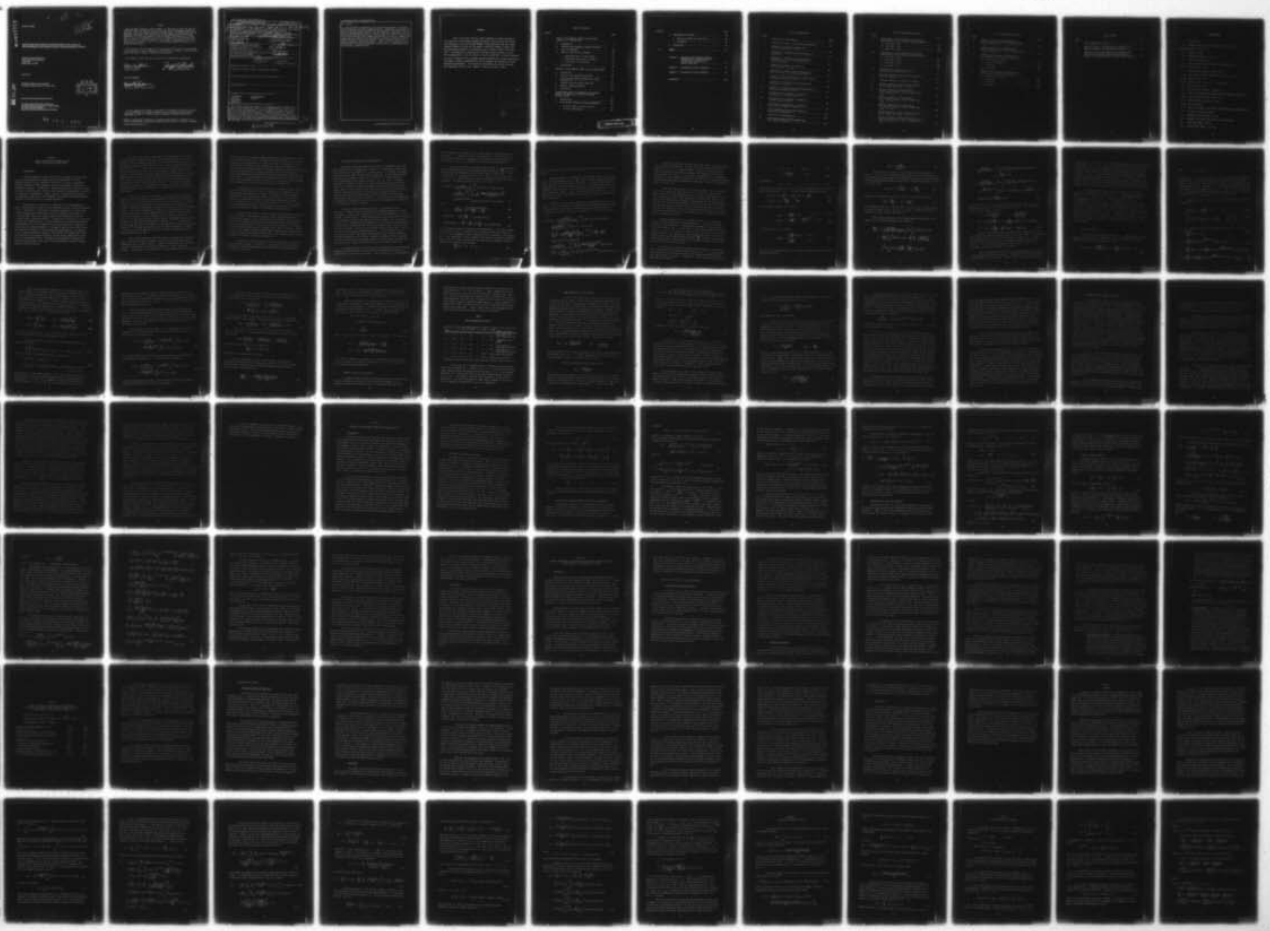

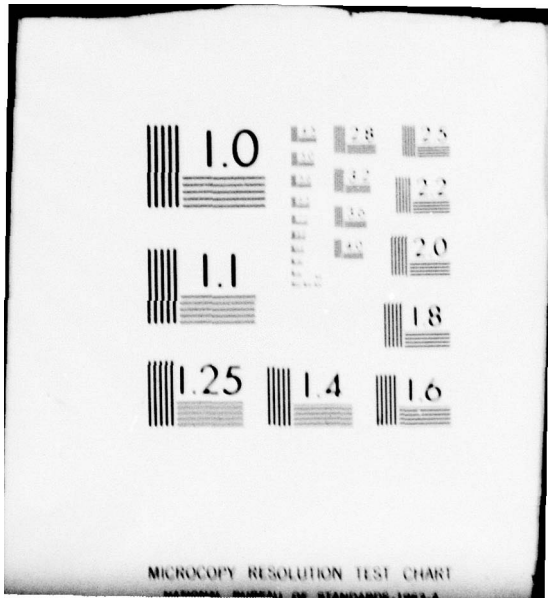
1.0
1.1
1.25
1.4
1.6
2.0
2.2
2.5
MICROCOPY RESOLUTION TEST CHART

AD A077712

AFAPL-TR-79-2061

LEVEL II

AERODYNAMIC AND ACOUSTIC INVESTIGATIONS OF AXIAL FLOW FAN AND COMPRESSOR BLADE ROWS, INCLUDING THREE-DIMENSIONAL EFFECTS

Aerodynamic Research Department
Calspan Advanced Technology Center
P.O. Box 400
Buffalo, New York 14225

August 1979

DDC
RECEIVED
DEC 6 1979
A

DDC FILE COPY

TECHNICAL REPORT AFAPL-TR-79-2061
Final Report for Period 1 June 1976 – 31 April 1979

Approved for public release; distribution unlimited.

AIR FORCE AERO-PROPULSION LABORATORY
AIR FORCE WRIGHT AERONAUTICAL LABORATORIES
AIR FORCE SYSTEMS COMMAND
WRIGHT-PATTERSON AIR FORCE BASE, OHIO 45433

79 12 6 086

NOTICE

When Government drawings, specifications, or other data are used for any purpose other than in connection with a definitely related Government procurement operation, the United States Government thereby incurs no responsibility nor any obligation whatsoever; and the fact that the government may have formulated, furnished, or in any way supplied the said drawings, specifications, or other data, is not to be regarded by implication or otherwise as in any manner licensing the holder or any other person or corporation, or conveying any rights or permission to manufacture, use, or sell any patented invention that may in any way be related thereto.

This report has been reviewed by the Information Office (OI) and is releasable to the National Technical Information Service (NTIS). At NTIS, it will be available to the general public, including foreign nations.

This technical report has been reviewed and is approved for publication.

Marvin A. Stibich
MARVIN A. STIBICH
Project Engineer

Joseph C. Hurst
JOSEPH C. HURST, Major, USAF
Chief, Components Branch

FOR THE COMMANDER

Ernest C. Simpson
ERNEST C. SIMPSON
Director, Turbine Engine Division

"If your address has changed, if you wish to be removed from our mailing list, or if the addressee is no longer employed by your organization please notify AFAPL/TBC ,W-PAFB, OH 45433 to help us maintain a current mailing list".

Copies of this report should not be returned unless return is required by security considerations, contractual obligations, or notice on a specific document.

AIR FORCE/56780/16 November 1979 — 60

SECURITY CLASSIFICATION OF THIS PAGE (When Data Entered)

REPORT DOCUMENTATION PAGE

READ INSTRUCTIONS BEFORE COMPLETING FORM

1. REPORT NUMBER: AFAPL-TR-79-2061	2. GOVT ACCESSION NO.
3. RECIPIENT'S CATALOG NUMBER	
4. TITLE (and Subtitle): AERODYNAMIC AND ACOUSTIC INVESTIGATIONS OF AXIAL FLOW FAN AND COMPRESSOR BLADE ROWS, INCLUDING THREE-DIMENSIONAL EFFECTS • CALSPAN	5. TYPE OF REPORT & PERIOD COVERED: Final Report 6/1/76 - 4/31/79
6. PERFORMING ORG. REPORT NUMBER: AE-5933-A-103	
7. AUTHOR(s): Gregory F. Homicz, John A. Lordi, Gary R. Ludwig	8. CONTRACT OR GRANT NUMBER(s): F33615-76-C-2092
9. PERFORMING ORGANIZATION NAME AND ADDRESS: Aerodynamic Research Department, Calspan Corporation, P. O. Box 400, Buffalo, New York 14225	10. PROGRAM ELEMENT, PROJECT, TASK AREA & WORK UNIT NUMBERS: 3066 04 24
11. CONTROLLING OFFICE NAME AND ADDRESS: U.S. Air Force Aero-Propulsion Laboratory /TBC, Air Force Systems Command, Wright-Patterson AFB, Ohio 45433	12. REPORT DATE: August 1979
	13. NUMBER OF PAGES: 146
14. MONITORING AGENCY NAME & ADDRESS (if different from Controlling Office)	15. SECURITY CLASS. (of this report): Unclassified
	15a. DECLASSIFICATION DOWNGRADING SCHEDULE

16. DISTRIBUTION STATEMENT (of this Report)

Approved for public release; distribution unlimited.

17. DISTRIBUTION STATEMENT (of the abstract entered in Block 20, if different from Report)

18. SUPPLEMENTARY NOTES

19. KEY WORDS (Continue on reverse side if necessary and identify by block number)

AERODYNAMICS
ACOUSTICS
JET ENGINES
COMPRESSOR
FLUID MECHANICS
FLUTTER

20. ABSTRACT (Continue on reverse side if necessary and identify by block number)

This report presents the results of a program designed to study the influence of three-dimensional effects on the aerodynamics and acoustics of axial flow fans and compressors. To avoid numerical solutions of the full nonlinear three-dimensional equations, a linearized analysis is employed. This is first applied to the determination of the steady loading on a three-dimensional annular blade row with a prescribed camber line in inviscid compressible flow. The blades are represented by pressure dipole singularities

over

DD FORM 1 JAN 73 1473 EDITION OF 1 NOV 65 IS OBSOLETE

SECURITY CLASSIFICATION OF THIS PAGE (When Data Entered)

391214

20. (Cont'd)

in a lifting-surface formulation, and a collocation procedure is presented for inverting the resulting integral equation. Comparisons are presented between the present results and those of two-dimensional strip theory and an inverse three-dimensional theory. Next the analysis is extended to the case of unsteady flow through the rotor, such as might be caused by inflow distortion or blade flutter. The integral equation for this case is somewhat more complicated, but appears to be solvable by a suitable extension of the procedure developed in the steady problem. Finally, further comparisons are presented between a theoretical model of rotor-stator interaction noise developed under a previous program and a current series of measurements made in an annular cascade facility.

FOREWORD

This is the final technical report prepared by Calspan Corporation on a portion of a multi-phase program sponsored by the Air Force Aero-Propulsion Laboratory, Air Force Systems Command, Wright-Patterson AFB, Ohio under Contract F33615-76-C-2092, for the period 1 June 1976 through 31 April 1979. The work reported herein was performed as part of Phases I and II of Project 3066, "Investigation of Rotating Stall and Turbine Heat Transfer in Axial Flow Turbomachinery", with Mr. Marvin A. Stibich, AFAPL/TBC, as Project Engineer. Dr. Gary R. Ludwig of the Aerodynamic Research Department of Calspan Corporation had overall technical responsibility for the program, and carried out the experimental measurements. The theoretical aerodynamic and acoustic analyses were performed jointly by Drs. Gregory F. Homicz and John A. Lordi.

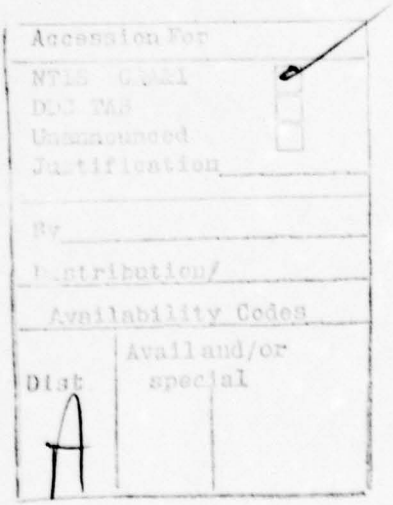

TABLE OF CONTENTS

SECTION		PAGE
I	DIRECT LIFTING-SURFACE THEORY FOR THE STEADY LOADING ON AN ANNULAR ROTOR	1
	A. INTRODUCTION	1
	B. FLOW MODEL AND GOVERNING INTEGRAL EQUATION	4
	C. SOLUTION PROCEDURE	11
	D. NUMERICAL RESULTS AND DISCUSSION	18
	1. Comparisons With 2-D Strip Theory	20
	2. Comparisons With Inverse 3-D Theory	25
	3. Convergence of Calculations	27
	E. CONCLUSIONS	28
II	UNSTEADY LIFTING-SURFACE THEORY FOR AN ANNULAR ROTOR	32
	A. INTRODUCTION	32
	B. FLOW MODEL AND GOVERNING EQUATIONS	33
	C. SOLUTIONS FOR PRESSURE MONOPOLE AND DIPOLE SINGULARITIES	34
	D. PRESSURE FIELD FOR ENTIRE BLADE ROW	37
	E. UNSTEADY INTEGRAL EQUATION	39
	F. CONCLUSIONS	47
III	FURTHER COMPARISONS OF APPROXIMATE ROTOR-STATOR INTERACTION THEORY WITH ACOUSTIC DATA FROM ANNULAR CASCADE	48
	A. INTRODUCTION	48
	B. ROTOR-STATOR INTERACTION NOISE MEASUREMENTS	49
	1. Rotating Annular Cascade Facility	49
	2. Acoustic Measurements	50

PRECEDING PAGE BLANK

SECTION		PAGE
	C. COMPARISONS WITH THEORY	59
	1. Theoretical Model and Input Data	59
	2. Discussion	60
	D. CONCLUSIONS	65
IV	SUMMARY	67
	APPENDIX A. EQUIVALENCE OF PRESSURE DIPOLE AND HORSESHOE VORTEX REPRESENTATIONS OF THE STEADY LOADING ON AN ANNULAR BLADE ROW	71
	APPENDIX B. EVALUATION OF RADIAL INTEGRALS	79
	APPENDIX C. EVALUATION OF AXIAL INTEGRALS	81
	REFERENCES	129

LIST OF ILLUSTRATIONS

FIGURE		PAGE
1	Blade Row and Duct Geometry	87
2	Camber Line Geometry in Blade-Fixed Coordinates	88
3	Comparison of Present 3-D Theory and 2-D Strip Theory for Cases 1-3	89
4	Comparison of Chordwise Load Distributions at Mid-Annulus	90
5	Comparison of Chordwise Load Distribution at Mid-Annulus for Case 3 With Isolated Flat Plate Distribution	91
6	Comparison of Present 3-D Theory and 2-D Strip Theory for Case 4	92
7	Comparison of Chordwise Load Distributions at Hub, Mid-Annulus, and Tip Radii for Case 4	93
8	Comparison of Present Theory with Design Values of Okurounmu and McCune for Case 5	94
9	Comparison of Chordwise Load Distributions at Mid-Annulus for Case 5	95
10	Comparison of Present Theory With Design Values of Okurounmu and McCune for Case 6	96
11	Convergence of Calculations vs. Number of Azimuthal Modes for Cases 1 and 4	97
12	Convergence of Calculations vs. Number of Azimuthal Modes for Case 5	98
13	Convergence of Calculations vs. Number of Radial Modes for Cases 1, 4 and 5	99
14	Test Configuration for Acoustic Studies of Rotor-Stator Interaction	100
15	Acoustic Test Instrumentation	101
16	Oscilloscope Records of Noise Signal from Rotor-Stator Interaction	102

LIST OF ILLUSTRATIONS (Cont'd.)

FIGURE		PAGE
17	Uncorrected 1/3 Octave Spectrum of Outer Wall Sound Pressure Level from Rotor-Stator Interaction	
	(a) Rotor RPM = 1140	103
	(b) Rotor RPM = 1150	104
	(c) Rotor RPM = 1160.5	105
18	Uncorrected 1/3 Octave Spectrum of Outer Wall Sound Pressure Level from Rotor-Stator Interaction	
	(a) Rotor RPM = 1695.5	106
	(b) Rotor RPM = 1700.5	107
	(c) Rotor RPM = 1710.5	108
	(d) Rotor RPM = 1716	109
19	Background Noise Correction Applied to Measured Sound Pressure Levels	110
20	Measured Frequency Response of Multifilters in Real Time Analyzer	111
21	Frequency Response of Condenser Microphone	112
22	RMS Wall Pressure at Blade Passage Frequency, Stator Stagger Angle δ_{SM} = 37.2 deg	113
23	RMS Wall Pressure at Second Harmonic of Blade Passage Frequency, Stator Stagger Angle, δ_{SM} = 37.2 deg	114
24	RMS Wall Pressure at Fourth Harmonic of Blade Passage Frequency, Stator Stagger Angle, δ_{SM} = 37.2 deg	115
25	RMS Wall Pressure at Fifth Harmonic of Blade Passage Frequency, Stator Stagger Angle, δ_{SM} = 37.2 deg	116
26	RMS Wall Pressure at Blade Passage Frequency, Stator Stagger Angle δ_{SM} = 28.2 deg	117
27	RMS Wall Pressure at Second and Third Harmonics of Blade Passage Frequency, Stator Stagger Angle, δ_{SM} = 28.2 deg	118

LIST OF ILLUSTRATIONS (Cont'd.)

FIGURE		PAGE
28	RMS Wall Pressure at Fourth Harmonic of Blade Passage Frequency, Stator Stagger Angle, δ_{SM} = 28.2 deg	119
29	RMS Wall Pressure at Fifth Harmonic of Blade Passage Frequency, Stator Stagger Angle, δ_{SM} = 28.2 deg	120
30	Comparison of Theoretically Predicted SPL With Experiment; Stator Stagger Angle = 28.2°	
	(a) Blade Passage Frequency	121
	(b) 2nd and 3rd Harmonics	122
	(c) 4th Harmonic	123
	(d) 5th Harmonic	124
31	Comparison of Theoretically Predicted SPL With Experiment; Stator Stagger Angle = 37.2°	
	(a) Blade Passage Frequency	125
	(b) 2nd Harmonic	126
	(c) 4th Harmonic	127
	(d) 5th Harmonic	128

LIST OF TABLES

TABLE		PAGE
1	Input Parameters for Cases 1-6	19
2	Sample of Acoustic Data Reduction for Spectrum With Multiple Harmonics of Blade Passage Frequency	56
3	Sample of Acoustic Data Reduction for Spectrum With Two Adjacent Third-Octave Bands Responding Nearly Equally to the Same Harmonic of Blade Passage Frequency..	57

NOMENCLATURE

a	sound speed
a_{ij}	loading coefficients in expansion of $\Delta\hat{p}$, Eqn. (12)
A_{mBk}, B_{mBk}	defined in Eqn. (7a, b)
B	number of blades
b_{nl}	camber line slope at (σ_n , x_l)
c	local blade chord (Fig. 2)
c_a	axial projection of blade chord, a constant (Fig. 2)
$C^{\pm}, S^{\pm}$	defined in Eqn. (11b)
C'	axial integrals defined in Eqn. (14a, e)
C'_{mBk}	axial cosine integrals defined in Eqn. (14b, c, f, g)
d_j, e_j	defined in Eqn. (18)
$f(r), g(r)$	defined in Eqns. (55) and (59), respectively
h	hub/tip ratio, r_H / r_T
$H(x)$	Heaviside step function, $\frac{1}{2}[\,sgn(x) + 1\,]$
i, j	indices of chordwise and spanwise loading functions, respectively
$I^{\pm}_{mBk}$	radial integrals defined in Eqn. (13)
I_n, K_n	modified Bessel functions of order n
K_{mBk}	radial eigenvalue
l, n	indices of chordwise and spanwise collocation points, respectively
$L(\sigma)$	sectional lift per unit span
L_θ	tangential blade spacing, $2\pi r / B$
m, k	azimuthal and radial duct mode indices, respectively
M	axial Mach number, $U / a_{-\infty}$
M_R	relative Mach number, $U_R / a_{-\infty}$

$M_{(\sigma)}$	sectional pitching moment about mid-chord, positive clockwise
NI, NJ NK, NM	term at which i, j, k, and m series are truncated, respectively
NL, NN	number of chordwise and spanwise collocation points, respectively
η_{CL}	function describing the blade camber line
p	perturbation pressure; also used in Section II to denote integral shift in azimuthal mode number caused by inter-blade phase shift, Eqn. (49b)
$\hat{p}$	nondimensional perturbation pressure, $p/\frac{1}{2}\rho_{-\infty}U^2$
r, θ, z	cylindrical polar coordinates (Fig. 1)
R_{mBk}	orthonormal radial eigenfunctions
s, n	local streamwise and normal coordinates (Fig. 2)
$\hat{S}$	nondimensional streamwise coordinate, Eqn. (10)
$sgn(x)$	sign function, ± 1 for $x \gtrless 0$
S^i_{mBk}	axial sine integrals defined in Eqns. (14d, h)
U	uniform axial velocity
U_R	relative free-stream velocity, $U\sqrt{1+\left(\frac{\omega r}{U}\right)^2}$
v	perturbation velocity
V_{mBk}	defined in Eqn. (2c)
x	nondimensional axial coordinate, Eqn. (5b)
α	angle of attack
β, β_R	$(1+M^2)^{1/2}$ and $(1-M_R^2)^{1/2}$, respectively
Γ	sectional circulation, positive counter-clockwise in Fig. 2
$\delta(x)$	Dirac delta function
Δ_B, Δ_D	turning angles in blade and duct-fixed coordinates, respectively; Eqns. (29) and (30)
ζ	helical coordinate, $\theta - \frac{\omega}{U}z$

η_T $c_a / 2r_T$

Λ_{mBk} defined in Eqn. (2b)

λ_{mBk} defined in Eqn. (2a) for steady analysis of Section I; defined in Eqn. (44) for unsteady analysis of Section II.

μ_B inter-blade phase shift, Eqn. (49a)

ρ density

σ nondimensional radial coordinate, r / r_T

ϕ $\cos^{-1} \chi$

ϕ_T $\omega r_T / U$

ψ undisturbed flow angle, $\tan^{-1}\left(\frac{\omega r}{U}\right)$

ω rotor angular velocity in steady analysis of Section I; harmonic excitation frequency in unsteady analysis of Section II.

Ω rotor angular velocity in unsteady analysis of Section II.

Subscripts

H evaluated at hub

T evaluated at tip

o source coordinate on surface, e.g., χ_o , σ_o ; also used in Section II to denote conditions at undisturbed state.

$\pm\infty$ conditions at $\bar{x} = \pm\infty$

Superscripts

$\hat{(\ )}$ dimensionless quantity

SECTION I

DIRECT LIFTING-SURFACE THEORY FOR THE STEADY LOADING ON AN ANNULAR ROTOR

A. INTRODUCTION

Increased emphasis on reduction of the size, weight, and noise output of axial flow turbomachinery demands improved understanding of the flow through high-speed fan and compressor blade rows. The task of calculating the fully nonlinear, three-dimensional, viscous flow through a blade row is a formidable one indeed. Consequently, some approximations are required in order to obtain a tractable model, the most familiar being the idealization of inviscid flow through a two-dimensional cascade. However, as more detailed questions are asked about modern blade row performance, the essentially three-dimensional character of the flow takes on increased importance.

This section is a report on our development of a three-dimensional, direct lifting-surface solution for the linearized, inviscid, steady flow through a rotor. Specifically, it presents a collocation procedure for inverting the linear integral equation which relates the local loading on the blades to a prescribed camber line; this integral equation had been derived as part of our effort under a previous contract.[1] Although such an analysis is in principle limited to low pressure ratios, it holds the promise of increasing our physical understanding of the rotor flowfield at a cost well below that of numerically solving the full nonlinear equations. The present approach also contains important features not present in the two-dimensional approximation. For example, it does include disturbances induced by the trailing vortex wakes which result from variations in the blade circulation, and the results reported below show this to be an important effect. The analysis and techniques developed here should also prove useful in the study of three-dimensional, unsteady loading, treated in the next section.

The study of linearized, compressible three-dimensional flow through an annular blade row began with the early work of McCune, who initially considered only the disturbance generated by the blades' thickness distribution.[2-4] Okurounmu and McCune[5] extended the analysis to treat the loading problem wherein the circulation, $\Gamma(r)$, is specified. Initially, they modeled each blade as a radially-oriented line vortex of variable spanwise strength, and were able to obtain useful expressions for the overall static and total pressure rise, and change in axial velocity. They later generalized this work to include finite chord effects in a lifting-surface type analysis, with the blades modeled as a distribution of these radially-oriented vortices.[6-7] Again, only the design problem was considered, i.e., computing the camber line required to produce a prescribed loading; this can be reduced to an integration over the known vortex distribution.

Just as in isolated airfoil theory, the solution to the off-design problem, in which one seeks the loading produced by blades with a prescribed camber line, is more difficult because it requires the inversion of an integral equation. McCune and Dharwadkar[8] considered this problem in the context of a Prandtl lifting-line approximation, using the vortex type of analysis presented in Ref. 5. This work represented the extension to subsonic flow of Falcao's earlier investigation of the incompressible case.[9] Namba[10,11] was the first to treat the off-design, or direct, problem using a lifting-surface type of analysis. He used pressure dipole singularities to represent the blade loading, in contrast to the vortex representation of McCune, et al.[5-8] Salaun later applied a pressure dipole representation to the prediction of the unsteady blade loading.[12,13] Although not concerned with the steady problem per se, Salaun briefly discussed it in Appendix D of Ref. 13; however, no numerical results were obtained for this case.

Thus, the present work, which also employs a pressure dipole approach, most closely parallels that of Namba; in fact, the basic flow model and the assumptions made are almost identical. However, we found that our form of the resulting integral equation differed from Namba's in several significant respects. Accordingly, a major portion of our effort under the previous contract[1]

was spent in trying to reconcile these differences, or barring that, to decide which formulation was correct. We undertook a detailed review of all the steps leading to the formulation of the integral equation. In particular, it was verified that our pressure monopole and dipole singularity solutions do, in fact, satisfy the governing partial differential equation, and that our expressions for the pressure and velocity fields associated with the entire blade row exhibit the appropriate discontinuities across the blade surfaces and trailing vortex wakes. It was also shown that the pressure and velocity fields satisfy global mass and momentum balances in the duct. On this basis, it was concluded that our formulation of the integral equation is the correct one.

This review of the linearized analysis was reported in detail in Ref. 1. During the current contract, we have also found that our formulation of the problem agrees with that given by Salaun. In addition, Salaun's ingenious manipulation of the infinite series which arise provided us with the link necessary to demonstrate the analytical equivalence between the horseshoe vortex representation of the blades used by McCune et al.,[5-8] and the pressure dipole representation used here. This equivalence is discussed in Appendix A, and further supports the validity of the present integral equation.

The major effort under the current contract has been spent in developing an efficient means of inverting the integral equation governing the direct lifting-surface problem. As will be seen below, the method of solution is the second feature distinguishing the present investigation from that of Namba.[11] The procedure adopted here is felt to be a more direct extension of the kernel-function methods frequently used in isolated airfoil theory. Moreover, the form assumed for the unknown loading allows analytical expressions to be derived for the required spanwise and chordwise integrations, thus affording greater accuracy and improved efficiency in terms of computer time.

Sub-section B briefly reviews the basic flow model and introduces the governing integral equation. Sub-section C describes the solution procedure, and numerical results and comparisons with other theories are presented and discussed in Sub-section D.

B. FLOW MODEL AND GOVERNING INTEGRAL EQUATION

The model assumes the blade row is housed in an infinitely long, hard-walled annular duct of constant hub/tip ratio, h , containing a uniform subsonic axial flow at Mach number M , as shown in Fig. 1. The flow is assumed to be inviscid and steady in blade-fixed coordinates. In this reference frame, the inflow has a relative velocity $U_R = [U^2+(\omega r)^2]^{1/2}$, and follows the helical undisturbed stream surfaces defined by $\zeta = \theta - \frac{\omega}{U} z$ = constant. The blades are assumed to produce only small perturbations about this undisturbed flow, allowing the linearized boundary conditions to be applied along these surfaces. The inviscid and small perturbation assumptions further imply that the disturbance flowfield is irrotational, and hence isentropic. We restrict ourselves here to considering only the case where the undisturbed relative Mach number at the tip is subsonic. This ensures that all disturbances will damp out far upstream of the rotor, and that far downstream only those due to the trailing vortices will remain.

Since the problem has been linearized, the disturbance fields produced by blade thickness and loading may be determined separately and then superimposed. However, this separation is not as straightforward as it is for a planar, isolated airfoil. In the thickness part of the rotor problem, the blades must be cambered to achieve the condition of zero loading. This zero-loading camber line, or "thickness-induced camber", can be calculated as an integral over the known source distribution once the blade thickness and the operating conditions are prescribed. This point is discussed at more length in Refs. 1 and 14; the latter contains sample calculations as well. In the idealized case of infinitely thin blades, the present loading analysis can be applied directly without consideration of this effect. However, for blades of finite thickness, the analysis assumes that the thickness-induced camber has been calculated and that the geometric camber is measured from this zero-loading camber line.

As mentioned earlier, the derivation of the governing integral equation appears in a previous report,[1] and so will not be repeated here except for a brief outline to introduce some concepts. The first step is in the manipulation

of the linearized flow equations into a single equation for the perturbation pressure, p . A singular solution to this equation, or Green's function, is then found which physically represents an idealized point force/volume acting on the fluid. This will be referred to as the pressure dipole solution.

To obtain the pressure field for the entire blade row, these singularities are distributed along the undisturbed stream surfaces $\zeta_j = \frac{2\pi j}{B}$, $j = 0, 1 \ldots B-1$, with the dipole's strength equal to the local loading, $\Delta p(r_0, s_0)$. On a blade surface, s_0 is uniquely related to z_0 , and so we set $\Delta p(r_0, s_0(z_0)) = \Delta p(r_0, z_0)$, and transform the chordwise integration to one over the axial coordinate. The resulting expression, Eqn. (134) in Ref. 1, is:

$$p(r,\theta,z) = \frac{\omega B}{\pi \beta^2 U (1-\bar{h}^2) r_T^2} \int_0^{C_a} \int_{\bar{h}}^{1} r_0 \, \Delta p(r_0, z_0) \, H(z-z_0) \, dz_0 \, dr_0$$

$$+ \frac{B}{4\pi \beta^2 r_T^2} \int_0^{C_a} \int_{r_H}^{r_T} \sum_{m=-\infty}^{\infty} \sum_{k=1}^{\infty} \frac{R_{mBk}(\sigma) R_{mBk}(\sigma_0) e^{imB\zeta}}{\omega \lambda_{mBk} / U}$$

$$\cdot e^{\Lambda_{mBk}(z, z_0)(z-z_0)} V_{mBk}(r_0, z, z_0) \, \Delta p(r_0, z_0) \, dz_0 \, dr_0 \qquad (1)$$

where

$$\lambda_{mBk} = \frac{|mB| U}{\omega r_T \beta^2} \sqrt{\beta^2 \left(\frac{K_{mBk}}{mB}\right)^2 - \left(\frac{\omega r_T}{a_\infty}\right)^2} \qquad (2a)$$

$$\Lambda_{mBk}(z, z_0) = \frac{\omega}{U} \left[\frac{imB}{\beta^2} - \lambda_{mBk} \, sgn(z - z_0)\right] \qquad (2b)$$

$$V_{mBk}(r, z, z_0) = \frac{imB}{r} - \frac{\omega^2 r}{U^2} \left[imB \frac{M^2}{\beta^2} - \lambda_{mBk} \, sgn(z - z_0)\right] \qquad (2c)$$

and the remaining symbols are defined in the Nomenclature. It has been assumed for convenience in Eqn. (1) that the axial projection of the blade chord, C_a in Fig. 2, is independent of radius, though this is not essential to the analysis. Eqn. (1) has been shown to yield a pressure field which is continuous everywhere except across the blades, and satisfies the same hard-wall boundary condition imposed on the pressure dipole solution,

$$\frac{\partial p}{\partial r} = 0 \quad \text{at} \quad r = r_H, r_T \qquad (3)$$

Eqn. (3) is equivalent to requiring that the radial velocity vanish at the hub and tip.

The above result is a superposition of duct modes which are sinusoidal in θ with a fundamental period $\frac{2\pi}{B}$, have a complex exponential dependence on z, and whose radial variation is described by the radial eigenfunctions R_{mBk} and their associated eigenvalues, K_{mBk}. The R_{mBk} denote linear combinations of Bessel functions of the first and second kind which satisfy Eqn. (3). Their argument is actually $K_{mBk}\,r$, which is written here simply as σ for the sake of brevity. These functions are described at length by McCune[2-4] and Tyler and Sofrin.[15]

Knowing ϕ, the normal component of the disturbance velocity, v_n, (see Fig. 2) can be obtained by integrating the corresponding momentum equation from upstream infinity along the undisturbed helical streamline through (r, θ, z). This result, obtained by combining Eqns. (145) and (164) of Ref. 1, is:

$$
\begin{aligned}
v_n(r,\zeta,\Xi) &= \frac{B\left(\frac{\omega r}{U}\right)^2}{\pi \rho_{-\infty} U_R\, r\, \beta^2 (1-M_z^2)\, r_T^2} \int_0^{c_a}\int_{r_H}^{r_T} r_0\, \Delta p(r_0,\Xi_0)\, H(\Xi-\Xi_0)\, d\Xi_0\, dr_0 \\
&- \frac{B\left[1+\left(\frac{\omega r}{U}\right)^2\right]^{1/2}}{2\pi \rho_{-\infty} U r} \left\{ \int_0^{c_a} \Delta p(r,\Xi_0)\, H(\Xi-\Xi_0)\, d\Xi_0 \right. \\
&- \sum_{m=-\infty,\, m\neq 0}^{\infty} \sum_{k=1}^{\infty} \frac{R_{mBk}(\sigma)\, e^{imB\zeta}}{(mB)^2\left[\left(\frac{K_{mBk}}{mB}\right)^2+\left(\frac{\omega r_T}{U}\right)^2\right]} \int_0^{c_a}\int_{r_H}^{r_T} \left(r_0 \frac{\partial^2 \Delta p}{\partial r_0^2} + \frac{\partial \Delta p}{\partial r_0}\right) \\
&\left. \cdot R_{mBk}(\sigma_0)\, H(\Xi-\Xi_0)\, d\Xi_0\, dr_0 \right\} \\
&+ \frac{B}{4\pi \beta^2 r_T^2 \rho_{-\infty} U_R} \int_{r_H}^{r_T}\int_0^{c_a} \sum_{m=-\infty,\, m\neq 0}^{\infty} \sum_{k=1}^{\infty} \frac{R_{mBk}(\sigma) R_{mBk}(\sigma_0) e^{imB\zeta}}{\frac{\omega \lambda_{mBk}}{U}} V_{mBk}(r_0,\Xi,\Xi_0) \\
&\cdot \left\{ \frac{\omega r}{U} - \frac{imB}{r\,\lambda_{mBk}(\Xi,\Xi_0)} \left[1+\left(\frac{\omega r}{U}\right)^2\right] \right\} e^{\lambda_{mBk}(\Xi,\Xi_0)(\Xi-\Xi_0)}\, \Delta p(r_0,\Xi_0)\, d\Xi_0\, dr_0
\end{aligned}
\tag{4}
$$

Note that the terms in the first four lines of Eqn. (4) are identically zero upstream of the blade row. The first two lines represent contributions from the $m=0$, $K=0$, or plane wave mode. The next term, which involves radial derivatives of the loading, represents the influence of the trailing vortex pattern. For fixed ζ, this term is independent of z downstream of the blade row, which reflects the fact that the vortices are convected downstream without attenuation along the undisturbed streamlines. This will be referred to below as the wake term.

In the last group of terms, since we have assumed $M_R < 1$ everywhere, one can easily show that λ_{mBk} from Eqn. (2a) is always real and positive. Hence, these terms rapidly attenuate as one moves away from the blade row, and will be referred to below as the exponentially decaying terms. When the tip relative Mach number becomes supersonic, certain modes will propagate undamped down the duct. This was first noted by McCune,[2-4] who was thus able to relate the resulting acoustic radiation directly to the blade thickness distribution. Such modes are identical in form to the propagating duct acoustic modes studied by Tyler and Sofrin,[15] which have since formed the basis for numerous investigations of turbomachinery noise.

The above expression for v_n was shown in Ref. 1 to be continuous across the blade surfaces, as is required physically. As part of this demonstration, it was found useful to integrate the exponentially decaying terms by parts with respect to z_o. At that time, it was anticipated that this altered form for v_n, Eqn. (172) of Ref. 1, would be used as the basis for the desired integral equation. This approach was later abandoned for several reasons, the principal one being the added complication that $\frac{\partial \Delta p}{\partial z_o}$ appears in the integrand rather than Δp itself, and the former can be expected to exhibit singularities at both the leading and trailing edges.

To convert Eqn. (4) into the desired integral equation, the right-hand side is specialized to the reference blade surface, $\zeta = 0$. It is also convenient for machine calculations to rationalize the resulting expression so that only real arithmetic is involved. From here on, we will work with the following dimensionless coordinates,

$$\sigma = r/r_T \qquad \lambda \le \sigma \le 1 \tag{5a}$$

$$\chi = \frac{z - c_a/2}{c_a/2} \qquad -1 \le \chi \le 1 \tag{5b}$$

and parameters,

$$\phi_T = \omega r_T / U \qquad \eta_T = c_a / 2 r_T \tag{6a}$$

One can express the aspect ratio and a solidity parameter based on the constant axial chord projection, c_a, in terms of these dimensionless groups:

$$\text{Aspect ratio} = \frac{r_T - r_r}{c_a} = \frac{r_T}{c_a}(1 - \lambda) = \frac{1 - \lambda}{2\eta_T} \tag{6b}$$

$$\text{Solidity at tip} = \frac{B c_a}{2\pi r_T} = \frac{B \eta_T}{\pi} \tag{6c}$$

As a convenient shorthand, we also define

$$A_{mBk} = \left(\frac{K_{mBk}}{mB}\right)^2 + \phi_T^2 \qquad m \neq 0 \tag{7a}$$

$$\beta_{mBk} = \left[\left(\frac{K_{mBk}}{mB}\right)^2 - \left(\frac{\phi_T M}{\beta}\right)^2\right]^{1/2} \qquad m \neq 0 \tag{7b}$$

in terms of which λ_{mBk} becomes

$$\lambda_{mBk} = \begin{cases} \dfrac{mB}{\beta \phi_T}\,\beta_{mBk} & m \neq 0 \\ \dfrac{K_{0k}}{\beta \phi_T} & m = 0 \end{cases} \tag{7c}$$

The loading is nondimensionalized by the dynamic pressure associated with the uniform axial velocity,

$$\Delta\hat{p} = \frac{\Delta p}{\frac{1}{2}\rho_{-\infty} U^2} \tag{8}$$

The left-hand side of Eqn. (4) is related to the blade geometry as follows. Let $\eta_{CL}(S,r)$ denote the function describing the blade camber line as a function of streamwise and radial coordinates (see Fig. 2), after accounting for any thickness-induced camber as noted above. Then the blade boundary condition requires that

$$v_n(\zeta = 0) = U_R \frac{\partial \eta_{CL}}{\partial S}\Big)_r = U_R \frac{\partial \hat{\eta}_{CL}}{\partial \hat{S}}\Big)_\sigma \tag{9}$$

where we have nondimensionalized η_{CL} and S by the local semi-chord:

$$\hat{\eta}_{CL} = \frac{\eta_{CL}}{c/2} \qquad \hat{S} = \frac{S - c/2}{c/2} \tag{10}$$

On the reference blade $z = S\cos\psi$, where $\psi = \tan^{-1}(\phi_T \sigma)$ is the local undisturbed flow angle (Fig. 2), and $c_a = c\cos\psi$. It then follows from the definitions in Eqns. (5) and (10) that $\hat{S} = x$.

With the above definitions, the integral equation relating the blade camber line to the unknown loading can be written as:

$$\frac{\partial \hat{\eta}_{CL}}{\partial \hat{S}}\Big)_\sigma = \frac{B\eta_T \phi_T^2 \sigma}{2\pi\beta^2(1-h^2)(1+\phi_T^2\sigma^2)} \int_{-1}^{x} dx_0 \int_h^1 d\sigma_0\, \Delta\hat{p}(\sigma_0, x_0)\,\sigma_0$$

$$- \frac{B\eta_T}{4\pi\sigma}\left\{\int_{-1}^{x} \Delta\hat{p}(\sigma, x_0)\,dx_0 - 2\sum_{m=1}^{\infty}\sum_{k=1}^{\infty} \frac{R_{mBk}(\sigma)}{(mB)^2 A_{mBk}}\right.$$

$$\left. \cdot \int_{-1}^{x} dx_0 \int_h^1 d\sigma_0 \left(\sigma_0 \frac{\partial^2 \Delta\hat{p}}{\partial \sigma_0^2} + \frac{\partial \Delta\hat{p}}{\partial \sigma_0}\right) R_{mBk}(\sigma_0)\right\}$$

$$+\frac{B\eta_T\phi_T^2\sigma}{8\pi\beta^2(1+\phi_T^2\sigma^2)}\int_{-1}^{+1}d\xi_0\int_{\xi}^{1}d\sigma_0\sum_{K=1}^{\infty}R_{0K}(\sigma)R_{0K}(\sigma_0)\sigma_0\Delta\hat{\Phi}(\sigma_0,\xi_0)\,\mathrm{sgn}(\xi-\xi_0)$$

$$\cdot e^{-\frac{K_{0K}\eta_T}{\beta}|\xi-\xi_0|}$$

$$+\frac{B\eta_T\phi_T^2}{4\pi\beta^2(1+\phi_T^2\sigma^2)}\int_{-1}^{+1}d\xi_0\int_{\xi}^{1}d\sigma_0\sum_{m=1}^{\infty}\sum_{K=1}^{\infty}R_{mBK}(\sigma)R_{mBK}(\sigma_0)\Delta\hat{\Phi}(\sigma_0,\xi_0)$$

$$\cdot e^{-\frac{mB\eta_T}{\beta}\beta_{mBK}|\xi-\xi_0|}\left\{\left[C^+\sigma_0+C^-\sigma_0^{-1}\right]\mathrm{sgn}(\xi-\xi_0)\cos\frac{mB\phi_T\eta_T}{\beta^2}(\xi-\xi_0)\right.$$

$$\left.+\left[S^+\sigma_0+S^-\sigma_0^{-1}\right]\sin\frac{mB\phi_T\eta_T}{\beta^2}(\xi-\xi_0)\right\} \qquad (11a)$$

To facilitate the solution procedure described next, like powers of σ_0 have been grouped together in the exponentially decaying terms. The coefficients of $\sigma_0^{\pm 1}$ in these terms are given by:

$$C^+ = \sigma - \frac{\beta^2(1+\phi_T^2\sigma^2)}{\sigma A_{mBK}} \qquad C^- = -\frac{\beta^2(1+\phi_T^2\sigma^2)}{\phi_T^2\sigma A_{mBK}}$$

$$S^+ = -\phi_T\beta\left[\frac{M^2\beta_2^2}{\sigma\beta^4}+\sigma\left(1+\frac{\beta_2^2}{\beta^2\phi_T^2\sigma^2}\right)\beta_{mBK}^2\right]\Big/A_{mBK}\,\beta_{mBK}$$

$$S^- = +\phi_T\beta\left[\frac{\beta_2^2}{\sigma\beta^2\phi_T^2}-\frac{\sigma}{\phi_T^2}\beta_{mBK}^2\right]\Big/A_{mBK}\,\beta_{mBK} \qquad (11b)$$

As noted in the Introduction, and discussed more extensively in Ref. 1, this integral equation does not agree with that derived by Namba. The differences can be traced back to the solution for the pressure field, Eqn. (1). Namba's expression for ϕ (Ref. 11, Eqn. (15)), quotes a different form for the $m=0$, $K=0$ term, and also contains a "scale factor", $\Lambda(\rho)$ in his terminology, which does not appear in our result.

Before proceeding to solve Eqn. (11), the singularities which can arise in the integrand warrant some discussion. In the form in which the wake terms first appeared, Eqn. (161) of Ref. 1, the m and K series could be shown to

diverge when $\sigma_o = \sigma$ and $x_o < x$. An analogous singularity occurs in isolated airfoil theory, Ref. 16, Eqn. (7-28a); both are produced by the trailing vorticity. As pointed out in Ref. 16, an integration by parts along the span will reduce the order of the singularity so that it can be evaluated using a Cauchy principal value. In Ref. 1, this process was carried one step further by integrating by parts twice along the span, and making use of Eqn. (3) at the limits. This leads to the form shown above, which involves only uniformly convergent series. The price one pays is that now the integrand involves radial derivatives of the unknown $\Delta\hat{\varphi}$; however, this is easily handled by the present solution procedure.

In the last group of terms, convergence of the m and k series is assured by the exponential decay with $|x - x_o|$. However, this mechanism is absent at $x_o = x$, where the terms proportional to $\sin \frac{mB\Phi_T \eta_T}{\beta^2}(x - x_o)$ vanish identically, but the $m = 0$ terms and those proportional to $\cos \frac{mB\Phi_T \eta_T}{\beta^2}(x - x_o)$ remain finite. If in addtion, $\sigma_o = \sigma$, the latter terms form divergent series. However, the only dependence on x_o that remains is through the $\operatorname{sgn}(x - x_o)$, so that the axial integrations can be interpreted in the Cauchy principal value sense. Physically, this singularity arises from the bound vorticity at (x_o, σ_o) . As pointed out in Ref. 16, if an analytical expression for the integrals can be found, the principal value interpretation is automatically satisfied. This is the case here, as shown below and in Appendix C.

C. SOLUTION PROCEDURE

In order to solve the integral equation, it is assumed that the unknown loading can be expanded in a finite series of suitably chosen chordwise and spanwise loading functions. Specifically, we set

$$\Delta\hat{\varphi}(\sigma_o, x_o) = \sqrt{\frac{1-x_o}{1+x_o}} \sum_{j=1}^{NJ} a_{1,j}\, \sigma_o^{j-1} + \sum_{i=2}^{NI} \sum_{j=1}^{NJ} a_{i,j}\, \sigma_o^{j-1} \sin(i-1)\Phi_o \tag{12}$$

where

$$\phi_0 = \cos^{-1} x_0$$

and the a_{ij}, $i = 1, 2 \ldots NI$, $j = 1, 2 \ldots NJ$, are constants to be determined by the solution. The chordwise functions are the same as those often used in subsonic airfoil theory. They automatically satisfy the Kutta condition at the trailing edge, $x_0 = +1$, and the $i = 1$ term exhibits the appropriate square root singularity at the leading edge, $x_0 = -1$. The polynomial variation in σ_0 allows simple treatment of the boundary condition in Eqn. (3), as well as the radial derivatives in the wake term, as will be seen shortly.

Substitution of Eqn. (12) into Eqn. (11a) leads to radial integrations of the form:

$$\int_h^1 \sigma_0^j \, d\sigma_0 = \frac{1 - h^{j+1}}{j+1} \equiv I^j \qquad j = 0, 1 \ldots \tag{13a}$$

$$\int_h^1 \sigma_0^j \, R_{m\beta k}(K_{m\beta k}\sigma_0) \, d\sigma_0 \equiv I^j_{m\beta k} \qquad \begin{matrix} j = -1, 0, 1 \ldots \\ m = 0 \ldots \infty \\ k = 1 \ldots \infty \end{matrix} \tag{13b}$$

the axial integrations which result are more complex; for $i = 1$ they are:

$$\int_{-1}^{x} \sqrt{\frac{1-x_0}{1+x_0}} \, dx_0 \equiv C'(x) \tag{14a}$$

$$\int_{-1}^{+1} \sqrt{\frac{1-x_0}{1+x_0}} \, \mathrm{sgn}(x - x_0) \, e^{-\frac{K_{\beta k}}{\beta}\eta_T |x - x_0|} \, dx_0 \equiv C'_{\beta k}(x) \tag{14b}$$

$$\int_{-1}^{+1} \sqrt{\frac{1-x_0}{1+x_0}} \, \mathrm{sgn}(x - x_0) \cos\frac{m\beta\phi_0\eta_T}{\beta^2}(x - x_0) \, e^{-\frac{m\beta\eta_T}{\beta}\beta_{m\beta k}|x - x_0|} \, dx_0 \equiv C'_{m\beta k}(x) \tag{14c}$$

$$\int_{-1}^{+1} \sqrt{\frac{1-x_0}{1+x_0}} \sin\frac{m\beta\phi_0\eta_T}{\beta^2}(x - x_0) \, e^{-\frac{m\beta\eta_T}{\beta}\beta_{m\beta k}|x - x_0|} \, dx_0 \equiv S'_{m\beta k}(x) \tag{14d}$$

and for $i \geq 2$ they are:

$$\int_{-1}^{x} \sin(i-1)\phi_o \, dz_o \equiv C^i(x) \tag{14e}$$

$$\int_{-1}^{+1} \sin(i-1)\phi_o \, \mathrm{sgn}(z-z_o)\, e^{-\frac{\kappa_{ok}\eta_r}{\beta}|z-z_o|} \, dz_o \equiv C^i_{ok}(x) \tag{14f}$$

$$\int_{-1}^{+1} \sin(i-1)\phi_o \, \mathrm{sgn}(z-z_o) \cos\frac{m\beta\phi_r\eta_r}{\beta^2}(x-z_o)\, e^{-\frac{m\beta\eta_r}{\beta}\beta_{m\theta k}|z-z_o|} \, dz_o \equiv C^i_{m\theta k}(x) \tag{14g}$$

$$\int_{-1}^{+1} \sin(i-1)\phi_o \sin\frac{m\beta\phi_r\eta_r}{\beta^2}(z-z_o)\, e^{-\frac{m\beta\eta_r}{\beta}\beta_{m\theta k}|z-z_o|} \, dz_o \equiv S^i_{m\theta k}(x) \tag{14h}$$

where it is understood that $\sin(i-1)\phi_o = \sin[(i-1)\cos^{-1}x_o]$. It so happens that both the radial and axial integrations defined in Eqns. (13) and (14) can be performed analytically, which is a great advantage over schemes requiring numerical quadrature. The resulting expressions are given in Appendices B and C; for the present, it is assumed that these quantities are all known.

Next we choose a set of collocation points $[\sigma_n, x_\ell]$, $n = 1,2 \ldots NN$ $\ell = 1,2 \ldots NL$, at which to evaluate Eqn. (11), and define

$$b_{n\ell} = \frac{\partial \hat{\eta}_{cL}}{\partial \hat{S}}(\sigma_n, x_\ell) \tag{15}$$

Substituting Eqns. (12) - (15) into Eqn. (11) reduces the integral equation to the following set of simultaneous linear algebraic equations for the a_{ij}'s :

$$\sum_{i=1}^{NI}\sum_{j=1}^{NJ} U_{ij}(\sigma_n, x_\ell)\, a_{ij} = b_{n\ell} \qquad n = 1,2 \ldots NN \quad \ell = 1,2 \ldots NL \tag{16}$$

where $NN \times NL = NI \times NJ$ for the system to be determinant. The elements of the matrix U represent the dimensionless upwash produced at point (σ_n , x_l) by the (i , j) loading function. These are given by:

$$U_{ij}(\sigma_n , x_l) = \frac{B \eta_T \phi_T^2 \sigma_n}{2\pi \beta^2 (1 - M^2)(1 + \phi_T^2 \sigma_n^2)} C^i(x_l) I^j$$

$$- \frac{B \eta_T}{4\pi \sigma_n} \left[C^i(x_l) \sigma_n^{j-1} - 2(j-1)^2 C^i(x_l) \sum_{m=1}^{NM} \sum_{k=1}^{NK} \frac{R_{mBk}(\sigma_n) I^{j-2}_{mBk}}{(mB)^2 A_{mBk}} \right]$$

$$+ \frac{B \eta_T \phi_T^2 \sigma_n}{8\pi \beta^2 (1 + \phi_T^2 \sigma_n^2)} \sum_{k=1}^{NK} C^i_{0k}(x_l) R_{0k}(\sigma_n) I^j_{0k}$$

$$+ \frac{B \eta_T \phi_T^2}{4\pi \beta^2 (1 + \phi_T^2 \sigma_n^2)} \sum_{m=1}^{NM} \sum_{k=1}^{NK} R_{mBk}(\sigma_n) \left[\left(C^+(\sigma_n) I^j_{mBk} + C^-(\sigma_n) I^{j-2}_{mBk} \right) C^i_{mBk}(x_l) \right.$$

$$\left. + \left(S^+(\sigma_n) I^j_{mBk} + S^-(\sigma_n) I^{j-2}_{mBk} \right) S^i_{mBk}(x_l) \right] \qquad (17)$$

where NM and NK are the terms at which the m and k series are truncated, respectively.

In writing Eqn. (17), use has been made of the following simplification in the wake term. For each (i, j), it becomes

$$-2 \sum_{m=1}^{\infty} \sum_{k=1}^{\infty} \frac{R_{mBk}(\sigma)}{(mB)^2 A_{mBk}} a_{ij} C^i(x) \left[(j-1)(j-2) I^{j-2}_{mBk} + (j-1) I^{j-2}_{mBk} \right]$$

$$= -2 a_{ij} (j-1)^2 C^i(x) \sum_{m=1}^{\infty} \sum_{k=1}^{\infty} \frac{R_{mBk}(\sigma)}{(mB)^2 A_{mBk}} I^{j-2}_{mBk}$$

This term is seen to vanish identically for the uniform spanwise loading function, $j = 1$, as it should, since there is no trailing vorticity in this case.

Before solving the matrix equation in (16), one more feature of the solution needs to be considered; namely, the hard-wall boundary condition in Eqn. (3) requires that $\Delta\hat{p}$ have zero spanwise derivative at the hub and tip. This condition can be enforced automatically as follows. If Eqn. (12) is differentiated with respect to σ_o, and the resulting expression set equal to zero at $\sigma_o = h$ and 1, two equations involving the a_{ij} will follow. Simultaneous satisfaction of these two equations will, in general, depend on α_o. But if it is required that they be satisfied for all $|\alpha_o| \leq 1$, and for each i individually, then $a_{i,NJ-1}$ and $a_{i,NJ}$ can be solved for uniquely:

$$a_{i,NJ-1} = \sum_{j=2}^{NJ-2} d_j a_{ij} \qquad d_j = -\frac{(j-1)(1-h^{j-NJ})}{(NJ-2)(1-h^{-1})} \tag{18a}$$

$$a_{i,NJ} = \sum_{j=2}^{NJ-2} e_j a_{ij} \qquad e_j = -\frac{(j-1)(1-h^{j-NJ+1})}{(NJ-1)(1-h)} \tag{18b}$$

In effect, for each value of i Eqn. (3) has been used to express two of the radial coefficients in terms of the remaining $(NJ-2)$.

Upon substituting Eqn. (18) into (16), one obtains an altered matrix equation of the form:

$$\sum_{i=1}^{NI} \sum_{j=1}^{NJ-2} U'_{ij}(\sigma_n, \alpha_\ell)\, a_{ij} = b_{n\ell} \qquad n = 1,2 \ldots NN \quad \ell = 1,2 \ldots NL \tag{19a}$$

where the elements of the modified matrix U' are given by:

$$U'_{ij}(\sigma_n, \alpha_\ell) = U_{ij}(\sigma_n, \alpha_\ell) \qquad j = 1$$

$$U'_{ij}(\sigma_n, \alpha_\ell) = U_{ij}(\sigma_n, \alpha_\ell) + d_j U_{i,NJ-1}(\sigma_n, \alpha_\ell) + e_j U_{i,NJ}(\sigma_n, \alpha_\ell) \tag{19b}$$
$$2 \leq j \leq NJ-2$$

Note that the $j = 1$ terms remain unaffected, since they satisfy the required condition trivially. Since the number of unknowns in Eqn. (19a) has effectively been reduced to $NI \times (NJ-2)$, the number of collocation points should be reduced accordingly. In view of how Eqn. (18) was derived, the most logical

approach would be to reduce the number of spanwise stations in order to get $NN \times NL = NI \times (NJ-2)$. Once having set up the matrix equation, its solution was carried out by using Gaussian elimination with pivoting for the cases reported here. This yields a_{ij} for all i and $j = 1 \ldots NJ-2$; the $a_{i,NJ-1}$ and $a_{i,NJ}$ are then obtained from Eqn. (18).

The local loading at any point on the blade is calculated from Eqn. (12). The form of that equation also allows simple analytical expressions to be derived for the sectional lift and moment coefficients, the overall torque and axial force coefficients, the static and total pressure rise, and the turning produced by the rotor. The integrations involved are elementary, and so only the results will be quoted.

The sectional lift on the blade $L(\sigma)$ is perpendicular to the local undisturbed flow, and considered positive when in the $+n$ direction (Fig. 2). We define the lift coefficient as

$$C_L(\sigma) \equiv \frac{L(\sigma)}{\frac{1}{2}\rho_\infty U^2 C_a} = \frac{[1+(\phi_T \sigma)^2]^{1/2}}{2} \int_{-1}^{+1} \Delta\hat{p}(\sigma, x)\, dx$$

$$= \frac{\pi[1+(\phi_T \sigma)^2]^{1/2}}{2} \sum_{j=1}^{NJ} \sigma^{j-1}\left(a_{1j} + \frac{1}{2} a_{2j}\right) \tag{20}$$

The pitching moment $M(\sigma)$ is taken about the blade mid-chord and considered positive when clockwise (Fig. 2). Its coefficient is defined as

$$C_M(\sigma) \equiv \frac{M(\sigma)}{\frac{1}{2}\rho_\infty U^2 C_a^2} = \left[\frac{1+(\phi_T \sigma)^2}{4}\right] \int_{-1}^{+1} x\, \Delta\hat{p}(\sigma, x)\, dx$$

$$= -\frac{\pi[1+(\phi_T \sigma)^2]}{8} \sum_{j=1}^{NJ} \sigma^{j-1}\left(a_{1j} - \frac{1}{2} a_{3j}\right) \tag{21}$$

Just as in isolated airfoil theory, we see that only the first few chordwise load functions contribute to the net lift and moment.

The overall torque exerted on the fluid by the complete blade row, T, is considered positive when counter-clockwise as one looks downstream (Fig. 1). We define the torque coefficient as:

$$C_T \equiv \frac{T}{\frac{1}{2}\rho_{-\infty} U^2 C_a r_T^2} = B \int_h^1 \frac{\sigma C_L(\sigma)\, d\sigma}{[1+(\phi_T \sigma)^2]^{1/2}}$$

$$= \frac{\pi B}{2} \sum_{j=1}^{NJ} (a_{1j} + \frac{1}{2} a_{2j}) \left(\frac{1 - h^{j+1}}{j+1} \right) \tag{22}$$

The axial force exerted by the blade row on the fluid, F_z is considered positive when it points upstream. The analogous coefficient is obtained from:

$$C_{F_z} \equiv \frac{F_z}{\frac{1}{2}\rho_{-\infty} U^2 C_a r_T} = B \phi_T \int_h^1 \frac{\sigma C_L(\sigma)\, d\sigma}{[1+(\phi_T \sigma)^2]^{1/2}} = \phi_T C_T \tag{23}$$

The net static pressure rise across the row can be evalauted from Eqn. (1) at $z = \pm \infty$, and when normalized by the dynamic pressure of the axial flow becomes

$$C_{p_s} = \frac{p_\infty - p_{-\infty}}{\frac{1}{2}\rho_{-\infty} U^2} = \frac{2 \phi_T \eta_T C_T}{\pi B^2 (1-h^2)} = \frac{2 \eta_T C_{F_z}}{\pi B^2 (1-h^2)} \tag{24}$$

The static pressure ratio is easily shown to be:

$$\frac{p_\infty}{p_{-\infty}} = 1 + \frac{\gamma}{2} M^2 C_{p_s} \tag{25}$$

where here γ is the specific heat ratio.

In duct coordinates, the rise in total enthalpy, and hence total temperature, can be related to the work done on the fluid. The total pressure ratio can then be obtained from the isentropic relations, and the result is, to first order in small quantities:

$$\frac{\langle p_{o_\infty} \rangle}{p_{o_{-\infty}}} = 1 + \frac{\gamma B \phi_T \eta_T M^2 C_L(\sigma) \cos \psi}{2\pi \left(1 + \frac{\gamma - 1}{2} M^2\right)} \tag{26}$$

The brackets on the left indicate that a circumferential average has been taken. After allowing for differences in notation, it is readily shown that Eqns. (24) and (26) are equivalent to those given in Ref. 5.

One can also express the circumferentially-averaged turning produced by the rotor in either duct or blade-fixed coordinates, Δ_D or Δ_B respectively, in terms of the above parameters. Turning is considered positive when the flow is deflected counter-clockwise in Fig. 2. To first order, $\Delta_D = -\langle v_\theta \rangle / U$ and $\Delta_D = -\langle v_n \rangle / U_R$, where v_θ can be put in terms of v_n and p through:[1]

$$v_\theta = v_n \cos\psi + v_s \sin\psi$$

$$= (1 + \phi_T^2 \sigma^2)^{-1/2} [v_n + (\phi_T \sigma) v_s] \tag{27}$$

$$v_s = -\frac{p}{\rho_{-\infty} U_R} \tag{28}$$

and p and v_n are given by Eqns. (1) and (4), respectively. The results are:

$$\Delta_D = \frac{B \eta_T C_L(\sigma)}{2\pi\sigma [1 + (\phi_T \sigma)^2]^{1/2}} = \frac{\Gamma(\sigma)}{U L_\theta(\sigma)} \tag{29}$$

$$\Delta_B = \Delta_D - \frac{\eta_T \phi_T^2 \sigma C_T}{\pi \beta^2 (1 - h^2) [1 + (\phi_T \sigma)^2]} \tag{30}$$

It is seen that, whereas Δ_D depends only on conditions at the local radius, Δ_B is influenced by the overall torque as well. Eqn. (30) is equivalent to that cited by McCune and Dharwadkar.[8]

D. NUMERICAL RESULTS AND DISCUSSION

A computer program implementing the solution procedure described above has been developed using double precision arithmetic throughout so as to minimize the influence of round-off error. Six cases have been run to test

the program over a broad range of operating conditions, as specified by the input parameters B , h , M , ϕ_T and η_T . Table 1 summarizes the values used for each case, along with a brief description of the specified camber line. The first three cases were designed to test the present theory against a two-dimensional strip theory at a high hub/tip ratio, where one would expect strip theory to provide a reasonable approximation. A similar comparison is drawn in Case 4 for a low hub/tip ratio, for which three-dimensional effects are much more significant. Finally, Cases 5 and 6 provide comparisons with the inverse three-dimensional theory of Okurounmu and McCune.[6,7]

TABLE 1

INPUT PARAMETERS FOR CASES 1-6

Case #	B	$h = \frac{r_H}{r_T}$	Axial Mach # M	$\phi_T = \frac{\omega r_T}{U}$	$\eta_T = \frac{c_a}{2r_T}$	Camber Line Shape
1	50	0.8	0.5	1.0	0.03	Flat plate at 5° local angle of attack
2	50	0.8	0.5	1.0	0.03	10% parabolic-arc camber
3	50	0.8	0.5	1.0	0.06	Flat plate at 5° local angle of attack
4	30	0.5	0.5	1.0	0.05	Flat plate at 5° local angle of attack
5	40	0.8	0.5	1.497	0.0833	Free vortex design
6	40	0.8	0.5	1.497	0.0833	20% variation in Γ

In each case, NI = 5 chordwise and NJ = 5 spanwise loading functions were used to represent $\Delta\hat{p}$. Along the chord, NL = 5 collocation stations were equally-spaced between the leading and trailing edges, $\chi = \pm 1$; in the spanwise direction, NN = 3 collocation stations were equally-spaced between the hub and tip, σ = h, 1. The number of azimuthal modes included in the calculation, NM, was 10 in all cases; the number of radial modes included, NK, was set at 20 or 30 depending on whether h was 0.8 or 0.5, respectively.

1. Comparisons With 2-D Strip Theory

In Case 1, the camber line was specified to be a flat plate at each radial station; however, a radial twist is imparted to the blades such as to hold the local angle of attack, α_{3D}, constant at +5 degrees. The high hub/tip ratio in this case suggests that the loading might be reasonably well predicted by application of a two-dimensional strip theory. However, caution must be exercised in making such comparisons; as pointed out by McCune and Dharwadkar,[8] two-dimensional cascade theory defines the "undisturbed" flow velocity as the vector mean of the inflow and outflow velocities, whereas in the present three-dimensional theory, it is defined to be the inflow velocity, U_R. Since the difference between these reference directions does not depend on axial position, it amounts to using a different angle of attack in the two-dimensional theory, α_{2D}, than would be used in the three-dimensional theory, α_{3D}, though the physical blade geometry and inflow velocity are the same. The difference between the two angles is proportional to the net turning across the row, which in turn can be related to the sectional loading:

$$\alpha_{2D} = \alpha_{3D} - \frac{\bar{C}_L B \Gamma_T \beta_R^2}{4\pi\sigma\beta^2} \qquad \bar{C}_L \equiv \frac{L}{\frac{1}{2}\rho_\infty U_R^2 C} \tag{31}$$

The lift coefficient $\bar{C}_L$ is more convenient to work with in a strip theory than that defined in Eqn. (20). It is easily shown that to first order in the perturbation scheme, the two are related by $\bar{C}_L = C_L \cos^3\psi$.

Now the two-dimensional theory predicts that

$$\bar{C}_L = \frac{2\pi K_\alpha \alpha_{2D}}{\beta_R} \tag{32}$$

where the factor K_α is defined as the ratio of the lift on a blade in cascade to the lift on the same blade operated as an isolated airfoil. For flat plate blades in incompressible flow, this factor has been expressed in closed form by Pistolesi[17] as a function of the stagger angle, γ, and solidity, $\frac{c}{t_g}$:

$$K_\alpha = \frac{2}{\pi}\left(\frac{L_\theta}{c}\right)\frac{\cosh\left[\pi\left(\frac{c}{L_\theta}\right)\cos\gamma\right] - \cos\left[\pi\left(\frac{c}{L_\theta}\right)\sin\gamma\right]}{\cos\gamma\sinh\left[\pi\left(\frac{c}{L_\theta}\right)\cos\gamma\right] + \sin\gamma\sin\left[\pi\left(\frac{c}{L_\theta}\right)\sin\gamma\right]} \quad (33)$$

The values of stagger and solidity to be used in Eqn. (33) are those in the corresponding incompressible flow. They are related to the values in the original cascade flow through the Prandtl-Glauert transformation described by Woolard:[18]

$$\begin{aligned} U_R^{INC} &= U_R & \alpha_{2D}^{INC} &= \alpha_{2D} \\ \tan\gamma^{INC} &= \frac{1}{\beta_R}\tan\gamma \\ \left(\frac{c}{L_\theta}\right)^{INC} &= \frac{\sin\gamma^{INC}}{\sin\gamma}\left(\frac{c}{L_\theta}\right) \end{aligned} \quad (34)$$

Elimination of α_{2D} between Eqns. (31) and (32) then gives:

$$\bar{C}_L = \frac{2\pi K_\alpha \alpha_{3D}}{\beta_2\left[1 + \frac{K_\alpha B \eta_T \beta_2}{2\sigma\beta^2}\right]} \quad (35)$$

A comparison of the strip theory predictions of Eqn. (35) for the conditions of Case 1 with our three-dimensional calculations is given in Fig. 5. When viewing these and subsequent results for $\bar{C}_L$ it should be kept in mind that the spanwise variation in L will be even greater, since the local dynamic pressure and chord both increase with radius. The agreement between the two calculations is seen to be quite good at mid-annulus. However, whereas the strip theory predicts a 35% increase in $\bar{C}_L$ from hub to tip, the three-dimensional results show little variation. The corresponding changes in the circulation, Γ, from hub to tip are +67% and 19%, respectively. Thus, significant trailing vortex effects can be expected despite the high hub/tip ratio.

The cascade factor K_α in Eqn. (33) was computed to be 0.96 at mid-annulus, indicating tthat the blades are operating nearly as isolated airfoils. This results from the low solidity of the blade row, which at this radius is roughly two-thirds. Hence, one would expect the chordwise load distribution to closely approximate that of an isolated flat plate. This comparison is shown

in Fig. 4, where the isolated airfoil result has been normalized by the factor K_α so as to yield the same sectional lift, i.e.,

$$\frac{\Delta p}{\frac{1}{2}\rho_\infty U_R^2} = \frac{4 K_\alpha \alpha_{2D}}{\beta_R} \tan\frac{\phi}{2} \tag{36}$$

The agreement is seen to be excellent.

In Case 2, the blades are assumed to have zero angle of attack relative to the inflow velocity and a parabolic-arc camber line; otherwise, the input parameters are the same as in Case 1. The ratio of maximum camber, μ_{MAX}, to the local chord length is take to be 0.10, and constant with radius. As in Case 1, one would expect that the high hub/tip ratio and low solidity would cause the three-dimensional results to approach those for a two-dimensional isolated airfoil. In the two-dimensional theory, the blade camber contributes to the lift coefficient in the amount

$$\bar{C}_L = \frac{2\pi K_\mu \hat{\mu}_{MAX}}{\beta_R} \qquad \hat{\mu}_{MAX} = \frac{\mu_{MAX}}{c/2} \tag{37}$$

where K_μ is the cascade correction factor for camber analogous to K_α in the case of the flat plate cascade. Unfortunately, while K_α can be expressed in closed form, K_μ cannot. But it was seen above that K_α is near unity anyway, and so it seems reasonable to assume that for these conditions K_μ is also. It should also be noted that even though $\alpha_{3D} = 0$ in this case, α_{2D} remains finite since there is still a finite turning. Thus, if the contributions from Eqns. (32) and (37) are added, and Eqn. (31) used to eliminate α_{2D}, the expression that results for $\bar{C}_L$ is

$$\bar{C}_L = \frac{2\pi \hat{\mu}_{MAX}}{\beta_R\left[1 + \frac{B\eta_T \beta_R}{2\sigma\beta^2}\right]} \tag{38}$$

The comparison between the lift coefficients predicted by Eqn. (38) and the full three-dimensional theory for Case 2 is also shown in Fig. 3. Again, good agreement is shown at mid-annulus, while the strip theory significantly overestimates the lift near the tip, and underestimates it near the hub. Having obtained the two-dimensional $\bar{C}_L$ from Eqn. (38), α_{2D} can be determined from Eqn. (31). One can then compute the corresponding chordwise load distribution, which is a superposition of the contributions from angle of attack and camber. The comparison between this prediction,

$$\frac{\Delta p}{\frac{1}{2}\rho_\infty U_R^2} = \frac{2}{\beta_R}\left[2\alpha_{2D}\tan\frac{\phi}{2} + \hat{\mu}_{MAX}\sin\phi\right] \tag{39}$$

and the three-dimensional results at mid-annulus is shown in Fig. 4, and again very good agreement is obtained.

For Case 3 η_T, and hence the solidity all across the annulus, has been doubled; the other input parameters and the camber line are the same as in Case 1. This case thus provides a better check on whether the present program correctly predicts blade interference effects. Its predictions and those from the strip theory, Eqn. (35), are also compared in Fig. 3. The higher solidity is seen to result in an overall reduction in loading, the factor K_α now being only 0.63 at mid-annulus. Again very good agreement between the two theories is exhibited at mid-annulus, with the discrepancies at other stations following the same trends seen in Cases 1 and 2. Whereas in those cases, the chordwise load distributions closely approximated those for an isolated airfoil, in this case one would expect the higher solidity (about 1.3) to alter the distribution somewhat. This is illustrated in Fig. 5 where the present results are again compared with Eqn. (36). Figs. 3 and 5 together show that the increased solidity acts to reduce the overall lift, and to shift more of the loading forward near the leading edge at the expense of that over the rear half of the blade.

The three cases discussed thus far were run to assess the agreement between the present analysis and strip theory for high hub/tip ratio. The conditions for Case 4 were chosen to exhibit more significant three-dimensional effects, with the hub/tip ratio reduced to 0.5 and the number of blades reduced

to 30; the other parameters and the camber line are the same as in Case 1. The results and comparison with strip theory are shown in Fig. 6. Both calculations show larger radial variations than in the previous cases, as expected. Again, the strip theory significantly underestimates the loading at inboard stations, and overestimates it near the tip, with good agreement at mid-annulus. However, the percentage errors relative to the three-dimensional predictions are much greater in this case than in the previous cases with high hub/tip ratio. It should be noted here that the strip theory predictions from $\sigma = 0.8$ outward are identical to those for Case 1. This occurs because the two parameters B and η_r enter the strip theory calculation only through the cascade solidity, and then only as the product $B\eta_r$, which is the same in both cases.

The local chordwise load distributions at the hub, mid-annulus, and tip radii as predicted by the three-dimensional theory are compared in Fig. 7. Surprisingly, there is seen to be very little variation between the three. No doubt this is due in large part to our having twisted the blades in such a way as to maintain the geometric angle of attack constant with radius.

In all four cases discussed thus far, it is seen that the present three-dimensional theory and a two-dimensional strip theory show good agreement only near mid-annulus. The strip theory tends to underestimate the loading near the hub and overestimate it near the tip, even when the hub/tip ratio is fairly high. McCune and Dharwadkar[8] have found the same effect in their study of the three-dimensional lifting-line approximation. In their model, each blade was represented by a single radially-oriented bound vortex. The strength of the vortex was allowed to vary radially, thus generating a trailing vortex pattern. By computing the resultant induced angle of attack at each spanwise station, McCune and Dharwadkar were thus able to correct the sectional lift predicted by strip theory to account for this three-dimensional effect. They concluded that the distribution of trailing vorticity acts in such a way as to reduce spanwise variations, which is consistent with the results presented here in Figs. 3 and 6.

2. Comparisons With Inverse 3-D Theory

The remaining two cases, 5 and 6, are of particular interest because they provide comparisons between the present work and another three-dimensional lifting-surface theory, that of Okurounmu and McCune.[6,7] In contrast to the off-design problem considered here, they solved the design problem, i.e., the determination of that camber line which will produce a specified load distribution. They presented plots of camber line slope vs. chordwise distance which we input to our program to see if the predicted load agreed with that specified in the design calculation. Two calculations were performed; the first was for a free-vortex design (Case 5), in which by definition the circulation about the blades, Γ , was constant with radius (Okurounmu and McCune refer to this as the constant-work case). In the second (Case 6), the circulation varied by 20% from hub to tip, referenced to its radius-weighted mean over the span. In both cases, the variation in design total pressure ratio across the annulus was in the range 1.10 to 1.15. The camber line slopes had been normalized by the overall static pressure rise coefficient across the rotors, as defined by Eqn. (24). This quantity was assumed to be unity in reading the curves, so that the present program should predict a value of C_{p_s} of one if the two theories are truly consistent.

For Case 5, the present program predicts a value of $C_{p_s} = 1.037$, which is considered very good in view of the accuracy with which the camber line slopes could be read from the graphs. The predicted circulation, normalized by the product of the constant axial velocity, U , and the tangential blade spacing at the tip, L_{θ_T} , is compared with the constant design value in Fig. 8. Good agreement is exhibited over the entire span. The distributions of C_L are also compared, the design values having been inferred from Eqn. (29). This quantity, rather than $\bar{C}_L$, was plotted because it reflects the true radial variation in lift.

Fig. 9 compares the chordwise load distribution at mid-annulus as predicted by the present analysis with the specified design distribution. The latter was proportional to $(1-\chi^2)^{1/2}$ at each radial station.[6,7] Good agreement

is shown over most of the chord; in principle, one should be able to reduce the discrepancies near the leading edge by increasing the number of chordwise collocation points. However, such a calculation was not felt warranted in view of the inherent inaccuracy in reading the slopes, as noted above.

Unfortunately, the results for Case 6 do not exhibit good agreement. In this case, C_{p_s} was predicted to be 1.54, or more than 50% too high. This is reflected in Fig. 10, which compares the predicted spanwise variations in Γ and C_L with those prescribed by Okurounmu and McCune; our results are significantly higher than the design distributions over the entire span.

The disagreement in this case has not yet been explained; it is too large to be reasonably ascribed to errors in reading the camber line slopes. As seen from Table 1, the inputs for Cases 5 and 6 are identical except for the blade geometry. In Case 6, this leads to significant trailing vortex effects not present in Case 5. The vortex representation of Refs. 6 and 7 uses an entirely different analytical expresssion for the wake terms than the dipole representation used here, as discussed in Appendix A. However, trailing vortex effects were by definition excluded a priori from the free-vortex design of Refs. 6 and 7. Under these circumstances, the most logical explanation for the good agreement in Case 5 and lack of agreement in Case 6 would be an error in the numerical evaluation of the wake terms.

In defense of the present calculations, it should be noted that the same number of spanwise loading functions was used to represent Δp in both Cases 5 and 6; in fact, the matrix equations which were solved in each case, Eqn. (19), were identical except for the column vector of known slopes on the right-hand side. Thus, trailing vorticity had the same opportunity to influence the results of Case 5 as Case 6, although in the former it correctly proved unimportant. If an error were present in our evaluation of these terms, it is difficult to see how it could produce significant discrepancies in one case and not the other. It is hoped to shed further light on this question in the future.

3. Convergence of Calculations

An investigation has been carried out on the effect of varying the number of azimuthal and radial modes included in the calculation, NM and NK. The static pressure rise coefficient defined in Eqn. (24) was chosen as a representative indicator of the overall convergence of the calculations. The convergence of C_{p_s} with NM is shown in Fig. 11 for Cases 1 and 4. The value at $NM = 10$ was chosen as a reference, and NK was held constant at a value of 20 for Case 1 and 30 for Case 4. It is seen that the convergence is fairly rapid, and that as few as 4 azimuthal modes give reasonably accurate results. Also, the greater three-dimensionality in Case 4 appears to aid the convergence in Fig. 11, but whether this would hold true in general is hard to say. Fig. 12 shows the convergence for Case 5 with $NK = 20$; here the actual values of C_{p_s} are plotted because the relative variations are much greater, and the "correct" or design value was known a priori. It appears that in this case, which has a solidity more than double that of Cases 1 or 4, at least 9 or 10 terms are needed to get the error in C_{p_s} below 10%.

The convergence of the calculations with NK is shown in Fig. 13 for Cases 1, 4 and 5. The value of NM was held constant at 10 in all runs. Noting the different scale factors on each curve, it is seen that for comparable accuracy one must include many more radial modes in the highly three-dimensional Case 4 than the more two-dimensional Case 1, which is intuitively satisfying. The highest solidity case, Case 5, again exhibits the slowest convergence.

It should be kept in mind that the convergence of more localized quantities, e.g., the sectional lift, L, or the local load distribution, Δp, can be expected to be slower than that exhibited for C_{p_s}. For Cases 1, 4 and 5, these appear to have converged within 1% with respect to NK. Cases 1 and 4 had also converged to this extent with respect to NM, although Case 5 still exhibited variations on the order of 8-9% between $NM = 9$ and 10. At present, the program storage is limited to $NM \leq 10$, and its modification to allow further increases in NM for this one case does not seem warranted at this time.

In summary, it appears that the inclusion of 10 azimuthal modes and between 20 and 30 radial modes, depending on hub/tip ratio, provides sufficient accuracy for most purposes, at least with regard to measures of overall performance. Of course, this conclusion may have to be modified for parameters significantly outside the range covered in Table 1. Qualitatively, it appears that high solidity aggravates the convergence of both the azimuthal and radial mode series. Low hub/tip ratio cases require more radial modes, as expected, but may have a small advantageous effect on the convergence of the azimuthal mode series.

The computer running times required for Cases 1-6 varied between 10 and 20 minutes on an IBM 360/65, using the G compiler. It is estimated that the running time on an IBM 370 would be reduced by a factor of 6 or 7. By far the majority of time is spent in evaluating the axial integrals. The time needed for their evaluation is primarily dictated by the number of integrals which can be done analytically before round-off error becomes a problem (see Appendix C). As a result, the running time can be expected to increase along with the solidity. As noted in connection with Cases 5 and 6, however, the coefficient matrix in Eqn. (19) depends only on the first five parameters in Table 1. The program has provision for storing the matrix on tape, so that subsequent calculations for the same operating conditions, but different blade camber lines, can be performed in a matter of seconds.

E. CONCLUSIONS

A method has been presented for computing the steady loading on a three-dimensional annular blade row in compressible flow, given the blade camber line. A kernel-function procedure is used to solve the integral equation relating the unknown loading to the camber line slope. The greatest advantage of the solution procedure presented here is that it allows analytical expressions to be derived for both the spanwise and chordwise integrals which are required. It also allows the various aerodynamic and performance parameters of the rotor to be expressed as simple algebraic functions of the loading expansion coefficients.

Calculations made thus far have concentrated on comparing the present predictions against those of two-dimensional strip theory, as well as the three-dimensional inverse lifting-surface theory of Okurounmu and McCune.[6,7] Good agreement between the three-dimensional and strip theories occurs only near mid-annulus, even for a moderately high hub/tip ratio. For low-solidity blade rows, it is also demonstrated that the present analysis predicts chordwise loading distributions at mid-annulus which are in excellent agreement with those of isolated thin-airfoil theory, for blades with both angle of attack and camber. The three-dimensional theory predicts loadings which are significantly higher near the hub and lower near the tip than the strip theory, thus giving much lower radial variations. Such behavior can be attributed to the induced angle of attack distribution generated by the trailing vortex wakes, which is not accounted for in strip theory; this smoothing appears to be the principle effect of three-dimensionality, at least for subsonic relative Mach numbers.

Comparison with the inverse three-dimensional theory of Okurounmu and McCune[6,7] shows good agreement over the whole span for the case in which the circulation is constant with radius. The chordwise load distribution at mid-annulus also compared well with the variation prescribed by them. However, for blades designed to produce a linear variation in circulation from hub to tip, the present theory predicts loadings which are significantly higher than the design distribution. It is hoped to resolve this discrepancy in the future.

When coupled with the analogous treatment of the disturbance flowfield produced by blade thickness,[2-4,14] the loading analysis presented here should provide an efficient means of studying three-dimensional effects in turbomachinery rows. The program should prove particularly advantageous for evaluating alternate blade camber lines at a given operating condition. The coefficient matrix in Eqn. (19) then needs to be evaluated and inverted only once, so that results for additional blade camber lines can be obtained in a matter of seconds, whereas a finite-difference solution, for example, would require a whole new calculation for each case. Thus, the program could serve to narrow down the number of candidate blade profiles before going to a finite-difference solution of the full nonlinear equations. It could also prove useful in providing

better initial conditions to a difference scheme, allowing the latter to converge in fewer iterations. Some development work remains, however. In particular, the effect of varying the position and number of the collocation points, and hence the number of terms in the expansion of the unknown loading, should be investigated. Also, the assumption of constant axial chord projection should be relaxed to allow application to a wider variety of blade geometries.

Initially, it was planned to extend the reported lifting-surface analysis to supersonic tip speeds. However, it has been decided instead to proceed with the extension to unsteady flow at subsonic tip speeds, for the following reasons. In previous linearized treatments of both the thickness[2-4] and inverse-loading[5-7] problems, a transonic resonance has been shown to occur at supersonic tip speeds. The amplitude of each duct acoustic mode is predicted to become infinite at its cut-off condition, though in reality the effects of viscosity and nonlinearities in the flow would prevent this from happening. Attempts have been made to incorporate viscous[2-4] and nonlinear effects[6,7] into the linearized model in an approximate, ad hoc fashion. Although the resonant modes can be successfully limited in this way, their resultant amplitudes are very much dependent on the particular assumptions made concerning the damping and/or nonlinear effects.

A more rigorous approach to the problem at supersonic tip speeds would retain the nonlinearities in the governing equations to be solved, rather than trying to approximate them in a linearized analysis. This of course requires numerical solution procedures, such as finite-difference techniques. Three-dimensional relaxation solutions of the transonic nonlinear small-disturbance equations, which are capable of including weak shocks in the flow, have been obtained for subsonic, but supercritical, flow through a rotor.[19] Efforts are currently underway to extend this technique to numerical computations for supersonic relative inflows.[20] Such an approach not only avoids the problem of transonic resonance, but is also extendable to the full nonlinear equations of motion, including the possibility of strong shock waves. A computer code for solving the full three-dimensional Euler equations for the steady flow through a rotor is presently being developed at Calspan under another program.[21]

For the above reasons, it was felt that a more useful extension of the linearized three-dimensional analysis would be to the study of subsonic unsteady flow through a rotor. The use of small-perturbation analyses in the study of the blades' aeroacoustic response to inflow distortion and to the problem of blade flutter is well established. This effort is described in Section II.

SECTION II

UNSTEADY LIFTING-SURFACE THEORY FOR AN ANNULAR ROTOR

A. INTRODUCTION

The previous section dealt with the prediction of the steady loading on an annular rotor for which the blade camber line has been specified. In this problem, the flow is viewed as stationary in blade-fixed coordinates on the assumption that the rotor is isolated, is operating in a uniform inflow, and consists of perfectly rigid blades. In practice of course, such conditions are never perfectly realized. The close proximity of other blade rows, as well as non-uniformities in the incoming air, give rise to distorted inflows which generate unsteady blade forces. These in turn can lead to degradations in performance. Also, vibrations of the blades themselves can sometimes couple to the resulting unsteady aerodynamic field in such a way as to lead to serious aeroelastic problems. Unsteady aerodynamic loads, whether from inflow distortion or blade flutter, also act as efficient acoustic sources, and hence their reduction is one means of reducing engine noise.

With the above applications in mind, work was begun on the formulation of an unsteady three-dimensional lifting-surface theory for an annular blade row. Namba[28] also has extended his analysis of the steady flow case to treat the unsteady problem. Kobayashi[29] later applied Namba's analysis to the study of pure tone fan noise due to inflow distortion. However, the same scale factor appears in this formulation as was included in the steady problem. As mentioned in Section I-B, we have found no justification for its presence, and hence feel the numerical results in Refs. 28 and 29 must be viewed with caution. Salaun[12,13] has also presented a lifting-surface theory for the unsteady case, as noted earlier, and we have shown that our expression for the pressure field generated by the blade row is in agreement with his. We are hopeful that the application of the techniques developed earlier for the steady problem will lead to an efficient inversion of the unsteady integral equation as well.

Section II-B below presents the assumptions made in the analysis and the governing partial differential equation. In Section II-C, solutions to the equation are given corresponding to unsteady pressure monopole (source) and dipole (force) singularities. The latter are used in Section II-D to develop the pressure field for the entire blade row. This is used in Section II-E to derive the governing integral equation, whose features are then discussed relative to the proposed solution procedure. Wherever possible, the notation has been kept consistent with that used in Section I for the steady case, with a few exceptions which will be noted as they arise.

B. FLOW MODEL AND GOVERNING EQUATIONS

The same geometry is assumed for the present case as had been used in our earlier study of the steady load problem. That is, the blade row is assumed to be housed in an infinitely long, hard-walled annular duct of constant hub/tip ratio, h , containing a uniform, inviscid, subsonic axial flow at Mach number M , as shown in Fig. 1. Any inflow distortions are viewed as small perturbations about this undisturbed state. The blades rotate with a constant angular velocity, which in this analysis is denoted Ω , rather than ω as used previously. In keeping with the usual convention, the latter symbol will be used for the harmonic time dependence below. Since the blade boundary conditions are more easily expressed in blade-fixed coordinates, we again express the governing equations in these terms. In this frame, the steady undisturbed inflow has a velocity $U_R = [U^2 + (\Omega r)^2]^{1/2}$, and follows the helical stream surfaces defined by $\xi = \theta - \frac{\Omega}{U} z$ = constant. The unsteady flow is assumed to be a small perturbation about this flow, so the disturbance field will be irrotational and isentropic. The linearization again allows us to apply the blade boundary conditions along the undisturbed stream surfaces, so that to first order in the perturbation scheme, blade thickness and camber do not affect the unsteady loads. We also assume that the undisturbed relative Mach number is subsonic all along the span.

The linearized three-dimensional equations of motion in blade-fixed coordinates can then be reduced to the following single equation for the perturbation pressure, p :

$$\mathcal{L}(p) = \nabla \cdot \vec{F}_B \tag{40a}$$

where the operator $\mathcal{L}$ is defined as $\left(\frac{\Omega r}{a_o}\right)^2$

$$\mathcal{L} = [1-M^2]\frac{\partial^2}{\partial x^2} + \left[1-\left(\frac{\Omega r}{a_o}\right)^2\right]\frac{\partial^2}{r^2\partial\theta^2} + \frac{1}{r}\frac{\partial}{\partial r}\left(r\frac{\partial}{\partial r}\right) \tag{40b}$$

$$- \frac{2M\Omega}{a_o}\frac{\partial^2}{\partial x\partial\theta} - \frac{2M}{a_o}\frac{\partial^2}{\partial x\partial t} - \frac{2\Omega}{a_o^2}\frac{\partial^2}{\partial\theta\partial t} - \frac{1}{a_o^2}\frac{\partial^2}{\partial t^2}$$

$\vec{F}_B$ is the force per unit volume exerted by the blade row on the fluid, and a_o is the undisturbed sound speed. (As will be seen shortly, the flow at upstream infinity will no longer be undisturbed, due to the presence of acoustic waves. Accordingly, in this section we will use the subscript $(\ )_o$ to denote conditions at the reference state.) The hard-wall boundary condition at the hub and tip, $v_r = 0$, can again be expressed as

$$\frac{\partial p}{\partial r} = 0 \qquad \text{at} \qquad r = r_H,\ r_T \tag{41}$$

Equations (40) and (41) are the same as those solved in the steady flow case, except for the addition of the three unsteady terms at the end of (40b).

C. SOLUTIONS FOR PRESSURE MONOPOLE AND DIPOLE SINGULARITIES

If we assume a harmonic $e^{i\omega t}$ time dependence for the excitation, whether it be due to blade flutter or inlet distortion, the pressure and velocity fields will also be harmonic at the same frequency because of the linearization of the equations. Then the first step in the solution of Eqn. (40) is to obtain the so-called pressure monopole solution, p_M , which

satisfies:

$$\mathcal{L}(p_M) = \frac{1}{r}\,\delta(\theta-\theta_0)\,\delta(r-r_0)\,\delta(z-z_0)\,e^{i\omega t} \tag{42}$$

subject to the hard-wall boundary condition in Eqn. (41).
This is obtained along the same lines as were followed for the steady flow problem[1], and the result is:

$$p_M = \frac{-e^{i\omega t}}{4\pi\beta^2 r_T^2} \sum_{n=-\infty}^{\infty} e^{in(\theta-\theta_0)} \sum_{k=0}^{\infty} \frac{R_{nk}(\sigma)\,R_{nk}(\sigma_0)}{\lambda_{nk}} \cdot e^{i\left(\frac{M}{\beta}\right)^2\left(\frac{n\Omega+\omega}{U}\right)(z-z_0) - \lambda_{nk}|z-z_0|} \tag{43}$$

where now,

$$\lambda_{nk} = \begin{cases} \dfrac{1}{\beta^2 r_T}\left[(\beta K_{nk})^2 - \left(\dfrac{n\Omega+\omega}{a_0} r_T\right)^2\right]^{1/2} & \text{below cut-off} \\ \dfrac{i\,\mathrm{sgn}(n\Omega+\omega)}{\beta^2 r_T}\left[\left(\dfrac{n\Omega+\omega}{a_0} r_T\right)^2 - (\beta K_{nk})^2\right]^{1/2} & \text{above cut-off} \end{cases} \tag{44}$$

As before, $\beta^2 = 1-M^2$, $\sigma = \frac{r}{r_T}$, and n and k are the azimuthal and radial duct mode indices, respectively. R_{nk} and K_{nk} are the corresponding radial eigenfunctions and eigenvalues which satisfy Eqn. (41).

In the analogous steady flow expression, Eqn. (81) of Ref. 1, it was found that since K_{nk} is always greater than n^{2-4}, then for subsonic relative Mach numbers, $\left(\frac{K_{nk}}{n}\right)^2 > \left(\frac{\Omega r_T}{\beta a_0}\right)^2$. As a result, all modes were below cut-off, with the exception of the $n=0$, $k=0$ mode. In contrast, a notable feature of the above solution is that a given mode may or may not propagate undamped down the duct, depending on whether $\left(\frac{n\Omega+\omega}{a_0} r_T\right)^2$ is greater or less than $(\beta K_{nk})^2$. For modes below cut-off, the signs in the complex exponential of Eqn. (43) were chosen so that such modes will decay, rather than grow, with distance from the singularity. For propagating modes, i.e., those above cut-off, the choice is dictated by the requirement that the group velocity of the mode, which is the velocity at which energy is carried in the flow, always

be away from the singularity. Alternatively, a small damping term can be added to the left side of Eqn. (42), which results in even the modes above cut-off having a small real part in the complex exponential of Eqn. (43). The correct sign choice is then made by requiring that this part always be negative, after which taking the limit of zero damping leads again to Eqn. (43).

Right at cut-off, $\lambda_{nk} = 0$, i.e.

$$(K_{nk})^2 = \left(\frac{n\Omega + \omega}{\beta a_o} r_T \right)^2 \tag{45}$$

and Eqn. (43) exhibits singular behavior. However, at this condition, the derivation leading up to (43) is no longer valid, so this situation must be treated as a special case. The solution for such a mode is,

$$\left[A_{nk} + B_{nk}(z - z_o) + \frac{e^{-in\theta_o} R_{nk}(\sigma_o)}{4\pi\beta^2 r_T^2} |z - z_o| \right] R_{nk}(\sigma) \tag{46}$$
$$\cdot e^{i\left[\omega t + n\theta + \left(\frac{M}{\beta}\right)^2 \left(\frac{n\Omega + \omega}{U}\right)(z - z_o)\right]}$$

where A_{nk} and B_{nk} are undetermined constants. This indeterminate nature of the solution is evidently the result of attempting to excite a linear system at one of its resonant points. Although interesting, such a situation is not likely to arise in practice. This is because the set of K_{nk} in Eqn. (45) depends only on the hub/tip ratio, blade number, and inter-blade phase angle, whereas the right-hand side is a function also of the rotor speed, excitation frequency, and axial Mach number.

Another interesting feature to note is that the $n = k = 0$ term in Eqn. (43) can be written in the same form as the others. This was not true in the steady case, where this mode had an entirely different type of structure. Nor can the correct steady term be obtained from that in Eqn. (43) by simply setting $\omega = 0$. This anomaly is explained by recognizing from Eqn. (44) that in the unsteady case λ_{oo} remains finite despite the fact that $K_{oo} = 0$, whereas in the steady problem λ_{oo} vanishes. Hence, in the unsteady case, this mode is always above cut-off, but in the steady case, it is always right at the cut-off condition. The correct form of this mode in the steady problem

should thus follow by specializing Eqn. (46) to $\omega = n = k = 0$, and we have shown that this is indeed the case.

The next step is to obtain an expression corresponding to a pressure dipole singularity, i.e., the solution to

$$\mathcal{L}(p_D) = \nabla \cdot \left[\frac{\hat{n}}{r} \delta(\theta - \theta_o) \delta(r - r_o) \delta(z - z_o) e^{i\omega t} \right] \tag{47}$$

where $\hat{n}$ is the unit vector perpendicular to the local undisturbed stream direction, as shown in Fig. 2. This is obtained by differentiating the monopole solution along this direction in source coordinates:

$$p_D = \frac{\partial p_M}{\partial n_o} = \frac{1}{\sqrt{1 + \left(\frac{\Omega r_o}{U}\right)^2}} \left(\frac{1}{r_o} \frac{\partial}{\partial \theta_o} - \frac{\Omega r_o}{U} \frac{\partial}{\partial z_o} \right) p_M$$

$$= \frac{e^{i\omega t}}{4\pi \beta^2 r_T^2 \sqrt{1 + \left(\frac{\Omega r_o}{U}\right)^2}} \sum_{n=-\infty}^{\infty} e^{in(\theta - \theta_o)} \sum_{k=0}^{\infty} \frac{R_{nk}(\sigma) R_{nk}(\sigma_o)}{\lambda_{nk}}$$

$$\cdot \left\{ i \left[\frac{n}{r_o} - \left(\frac{M}{\beta}\right)^2 \left(\frac{\Omega r_o}{U}\right) \left(\frac{n\Omega + \omega}{U}\right) \right] + \left(\frac{\Omega r_o}{U}\right) \lambda_{nk} \operatorname{sgn}(z - z_o) \right\}$$

$$\cdot e^{i \left(\frac{M}{\beta}\right)^2 \left(\frac{n\Omega + \omega}{U}\right)(z - z_o) - \lambda_{nk} |z - z_o|} \tag{48}$$

Physically, the pressure dipole solution represents the pressure field generated by a unit amplitude harmonic force concentrated at the point (r_o, θ_o, z_o) In the next sub-section, we use it to build up the pressure field for the entire blade row by superposition.

D. PRESSURE FIELD FOR ENTIRE BLADE ROW

The solution to Eqn. (40) for the entire blade row is next obtained by distributing the pressure dipole singularities along the undisturbed stream surfaces $\zeta = \frac{2\pi t}{B}$ in Fig. 2, with an amplitude equal to the local unsteady force exerted by the blade on the flow. In general, we must allow for a phase

difference between the loading on successive blades; denoting the local loading on the jth blade by Δp_j, we have

$$\Delta p_j = e^{ij\mu_B} \Delta p_0 \qquad j = 0, 1 \ldots B-1 \tag{49a}$$

where μ_B is the inter-blade phase shift, and Δp_0 the loading on the zeroth or reference blade. Periodicity requires that

$$B\mu_B = 2\pi p$$

or

$$\mu_B = \frac{2\pi p}{B} \qquad p = 0, 1 \ldots B-1 \tag{49b}$$

Higher values of p would simply reproduce the same phase shifts, e.g., $p = B$ is physically equivalent to $p = 0$, so we need consider only those values of p indicated in Eqn. (49b). Note however, that in any given calculation p, and hence μ_B, will assume a unique value.

By superposition, the pressure field for the entire blade row may be written as

$$p(r, z, \theta, t) = \sum_{j=0}^{B-1} \int_{r_H}^{r_T} \int_0^{C(r)} p_0\left(r, z, \theta, t; r_0, z_0, \theta_0 = \frac{2\pi j}{B} + \frac{\Omega z_0}{U}\right) \cdot e^{ij\mu_B} \Delta p(r_0, s_0)\, dr_0\, ds_0 \tag{50}$$

where we have set $\Delta p_0 = \Delta p$. Substituting for p_0 and μ_B, and transforming the streamwise integration to one over the axial coordinate using

$$S_0 = \sqrt{1 + \left(\frac{\Omega r_0}{U}\right)^2}\; z_0$$

we obtain

$$p(r, \theta, z, t) = \frac{B e^{i\omega t}}{4\pi\beta^2 r_T^2} \int_{r_H}^{r_T} dr_0 \int_0^{C_a} dz_0 \sum_{m=-\infty}^{\infty} \sum_{k=0}^{\infty} \frac{R_{nk}(\sigma) R_{nk}(\sigma_0)}{\lambda_{nk}} \cdot \left\{ i\left[\frac{n}{r_0} - \left(\frac{M}{\beta}\right)^2 \left(\frac{\Omega r_0}{U}\right)\left(\frac{n\Omega + \omega}{U}\right)\right] + \left(\frac{\Omega r_0}{U}\right) \lambda_{nk}\, \mathrm{sgn}(z - z_0) \right\} \Delta p(r_0, z_0) \cdot e^{in\left(\theta - \frac{\Omega}{U} z_0\right) + i\left(\frac{M}{\beta}\right)^2 \left(\frac{n\Omega + \omega}{U}\right)(z - z_0) - \lambda_{nk}|z - z_0|} \tag{51}$$

where now $n = mB + p$

In writing this result, it was assumed for convenience that the axial projection of the blade chord, $c_a = c / \sqrt{1+(\frac{\Omega r}{U})^2}$ was a constant independent of radius (Fig. 2). Also note that the same symbol φ has been used to denote both the unsteady pressure and the integral shift in azimuthal mode number caused by the phase shift between blades; when used below its meaning should be clear from the context in which it appears.

E. UNSTEADY INTEGRAL EQUATION

The desired integral equation relates the unknown loading, Δp, to v_n, the velocity component along the n direction in Fig. 2. It is this velocity which is most easily related to the excitation, whether inflow distortion or blade flutter, through the surface tangency condition. The expression for v_n may be derived from the normal component of the momentum equation:

$$\frac{\partial v_n}{\partial t} + U_R \frac{\partial v_n}{\partial s} = -\frac{1}{\rho_o}\left(\frac{\partial p}{\partial n} - F_B\right) \tag{52a}$$

which, for harmonic time dependence reduces to

$$U_R \frac{\partial v_n}{\partial s} + i\omega v_n = -\frac{1}{\rho_o}\left(\frac{\partial p}{\partial n} - F_B\right) \tag{52b}$$

where it is understood that the variables now refer only to their spatial amplitudes. This equation may be integrated from upstream infinity along the undisturbed stream direction, S. The constant of integration which must be supplied is the value of v_n at upstream infinity. Following the same line of reasoning given after Eqn. (44), we imagine that a small amount of dissipation is present in the system while performing the integration, which insures that $v_n(-\infty) = 0$. The limit of zero dissipation is then taken in the result, which reads

$$v_n(S) = -\frac{1}{\rho_o U_R}\int_{-\infty}^{S} e^{i\frac{\omega}{U_R}(S'-S)}\left(\frac{\partial p}{\partial n} - F_B\right) ds'$$

$$= -\frac{1}{\rho_0 U}\int_{-\infty}^{z} e^{i\frac{\omega}{U}(z'-z)}\left(\frac{\partial p}{\partial n} - F_B\right) dz' \qquad (53)$$

where the integration is to be carried out with r and n (or ζ) held constant.

The normal derivative of the pressure is obtained from Eqn. (51) as

$$\frac{\partial p}{\partial n} = \frac{1}{\sqrt{1+\left(\frac{\Omega r}{U}\right)^2}}\left(\frac{1}{r}\frac{\partial p}{\partial \theta} - \frac{\Omega r}{U}\frac{\partial p}{\partial z}\right)$$

$$= \frac{-\left(\frac{\Omega r}{U}\right)^2}{\beta^2 r\sqrt{1+\left(\frac{\Omega r}{U}\right)^2}}\,\Delta p(r,z)\,e^{i n\zeta}\sum_{j=0}^{B-1}\delta\left(\zeta - \frac{2\pi j}{B}\right) H(z)\,H(C_a - z)$$

$$+ \frac{B}{4\pi\beta^2 r_T^2\sqrt{1+\left(\frac{\Omega r}{U}\right)^2}}\int_{r_H}^{r_T} dr_0 \int_0^{C_a} dz_0 \sum_{m=-\infty}^{\infty}\sum_{k=0}^{\infty}\frac{R_{nk}(\sigma)R_{nk}(\sigma_0)}{\lambda_{nk}}$$

$$\cdot\left\{\left(\frac{\Omega r}{U}\right)\left(\frac{\Omega r_0}{U}\right)\lambda_{nk}^2 - f(r)\,f(r_0) + i\,\lambda_{nk}\,\mathrm{sgn}(z-z_0)\left[\left(\frac{\Omega r_0}{U}\right)f(r)\right.\right. \qquad (54)$$

$$\left.\left. + \left(\frac{\Omega r}{U}\right)f(r_0)\right]\right\} e^{in\zeta + i\left[\frac{n\Omega}{\beta^2 U} + \left(\frac{M}{\beta}\right)^2\frac{\omega}{U}\right](z-z_0) - \lambda_{nk}|z-z_0|}\,\Delta p(r_0, z_0)$$

where $\delta(x)$ and $H(x)$ are the Dirac delta function and Heaviside step function, respectively, and

$$f(r) \equiv \frac{n}{r} - \left(\frac{M}{\beta}\right)^2\left(\frac{\Omega r}{U}\right)\left(\frac{n\Omega+\omega}{U}\right) \qquad (55)$$

The force F_B is considered positive when it points in the $+\hat{n}$ direction; for the entire blade row it can be expressed as,

$$F_B = -\Delta p(r,z)\sum_{j=0}^{B-1} e^{ij\mu_B}\,\delta(n-n_j)\,H(z)\,H(C_a-z)$$

where the minus sign in front is required by the fact that in our convention Δp is positive when $p(n=0^-)$ is greater than $p(n=0^+)$, in which case F_B is negative.

Now

$$n = \frac{r\zeta}{\sqrt{1+\left(\frac{\Omega r}{U}\right)^2}} \qquad n_j = \frac{r\left(\frac{2\pi j}{B}\right)}{\sqrt{1+\left(\frac{\Omega r}{U}\right)^2}}$$

Using this and the definition of μ_B in Eqn. (49b), we obtain

$$F_B = \frac{-\Delta p(r,z)\sqrt{1+\left(\frac{\Omega r}{U}\right)^2}}{r} e^{i\rho\zeta} \sum_{j=0}^{B-1} \delta\left(\zeta - \frac{2\pi j}{B}\right) H(z)\, H(c_a - z) \tag{56}$$

Substituting (54) and (56) into (53) gives:

$$\begin{aligned} v_n = {} & \frac{-\beta_R^2}{\rho_o U_R \beta^2 r} e^{i\rho\zeta} \sum_{j=0}^{B-1} \delta\left(\zeta - \frac{2\pi j}{B}\right) \int_o^z e^{i\frac{\omega}{U}(z'-z)} \Delta p(r,z')\, dz' \\ & + \frac{B}{4\pi\beta^2\rho_o U_R r_T^2} \int_{r_H}^{r_T} dr_o \int_o^{c_a} dz_o \int_{-\infty}^{z} dz' \sum_{m=-\infty}^{\infty} \sum_{k=0}^{\infty} \frac{R_{nk}(\sigma) R_{nk}(\sigma_o)}{\lambda_{nk}} \Delta p(r_o, z_o) \\ & \cdot \left\{ f(r) f(r_o) - \left(\frac{\Omega r}{U}\right)\left(\frac{\Omega r_o}{U}\right)\lambda_{nk}^2 - i\lambda_{nk}\, sgn(z-z_o)\left[\left(\frac{\Omega r_o}{U}\right) f(r) \right.\right. \\ & \left.\left. + \left(\frac{\Omega r}{U}\right) f(r_o)\right]\right\} e^{in\zeta + i\frac{\omega}{U}(z_o - z) + i\left(\frac{n\Omega+\omega}{\beta^2 U}\right)(z'-z_o) - \lambda_{nk}|z'-z_o|} \end{aligned} \tag{57}$$

where we've implicitly assumed $0 \le z \le c_a$, so that the Heaviside step functions in the first term could be set to unity. Since r, ζ, z_o and z are each constant during the integration over z', the latter can be done analytically. After some manipulation, the result is:

$$\begin{aligned} v_n = {} & -\frac{\beta_R^2 e^{i\rho\zeta}}{\rho_o U_R \beta^2 r} \sum_{j=0}^{B-1} \delta\left(\zeta - \frac{2\pi j}{B}\right) \int_o^z e^{i\frac{\omega}{U}(z_o - z)} \Delta p(r, z_o)\, dz_o \\ & + \frac{B}{4\pi\rho_o U_R r_T^2} \int_{r_H}^{r_T} dr_o \int_o^{c_a} dz_o \sum_{m=-\infty}^{\infty} \sum_{k=0}^{\infty} \frac{R_{nk}(\sigma) R_{nk}(\sigma_o)\, e^{in\zeta + i\frac{\omega}{U}(z_o - z)}}{\lambda_{nk}\left[\left(\frac{K_{nk}}{r_T}\right)^2 + \left(\frac{n\Omega+\omega}{U}\right)^2\right]} \end{aligned}$$

$$\cdot \left\{ 2\lambda_{nk} \left[g(r)\, g(r_o) - \frac{\left(\frac{\Omega r}{U}\right)\left(\frac{\Omega r_o}{U}\right)}{\beta^2} \left[\left(\frac{K_{nk}}{r_T}\right)^2 + \left(\frac{n\Omega+\omega}{U}\right)^2 \right] \right] H(z-z_o) \right.$$

$$- \lambda_{nk} \left[g(r)\, g(r_o) - \frac{\left(\frac{\Omega r}{U}\right)\left(\frac{\Omega r_o}{U}\right)}{\beta^2} \left[\left(\frac{K_{nk}}{r_T}\right)^2 + \left(\frac{n\Omega+\omega}{U}\right)^2 \right] \right] \operatorname{sgn}(z-z_o)$$

$$\cdot e^{i\left(\frac{n\Omega+\omega}{\beta^2 U}\right)(z-z_o) - \lambda_{nk}|z-z_o|}$$

$$- i \left[\left(\frac{n\Omega+\omega}{\beta^2 U}\right) \left[f(r) f(r_o) - \left(\frac{\Omega r}{U}\right)\left(\frac{\Omega r_o}{U}\right) \lambda_{nk}^2 \right] - \lambda_{nk}^2 \left[\left(\frac{\Omega r_o}{U}\right) f(r) + \left(\frac{\Omega r}{U}\right) f(r_o) \right] \right]$$

$$\left. \cdot e^{i\left(\frac{n\Omega+\omega}{\beta^2 U}\right)(z-z_o) - \lambda_{nk}|z-z_o|} \right\} \Delta p(r_o, z_o) \tag{58}$$

where $f(r)$ was defined in (55) and

$$g(r) \equiv \frac{n}{r} + \left(\frac{\Omega r}{U}\right)\left(\frac{n\Omega+\omega}{U}\right) \tag{59}$$

Consider the convergence of the m and k series in Eqn. (58). In the last two terms, convergence of the series is assured by the presence of the factor $e^{-\lambda_{nk}|z-z_o|}$. This is because for m (and hence n) fixed, as k becomes large, K_{nk} grows linearly with k [30]:

$$K_{nk} \sim \frac{\pi k}{1-h} \qquad k >> n, \quad n \text{ fixed} \tag{60}$$

and beyond a certain point, the modes cut-off (Eqn. (44)). From then on, λ_{nk} remains real and grows with k, thus insuring exponential convergence. Conversely, in the limit of large $|m|$ (and hence $|n|$), for k fixed, it is known that [2-4]:

$$K_{nk} \sim |n| \qquad n >> 1, \quad k \text{ fixed} \tag{61}$$

and hence,

$$\lambda_{nk} \sim \frac{\ln|\beta_R}{\beta^2 r_T} \tag{62}$$

Since we have assumed $\beta_R^2 > 0$, convergence is again assured.

Unfortunately, this exponential decay is not operative in the first group of terms under the double summation, i.e., those proportional to $H(z-z_o)$; these diverge with respect to both m and k. The first term in Eqn. (58) also poses a problem, in that it exhibits singular behavior on the blade surfaces $\zeta = \frac{2\pi j}{B}$, which is where we ultimately wish to evaluate it. Similar difficulties arose in the steady flow problem; to remove them in the present case, a procedure very much analogous to that used in Ref. 1 was followed. Namely, the same group of divergent terms was added and subtracted from the original divergent series. The added terms can ultimately be summed in the context of generalized functions to give a sequence of delta functions which exactly cancels the first term of Eqn. (58). The original minus the subtracted terms, through use of the fact that each of the R_{nk} satisfies Bessel's equation, can be rewritten in terms of the first and second radial derivatives of the R_{nk} . If two successive integrations by parts in the radial coordinate are then made, and advantage taken of the fact that both Δp and R_{nk} satisfy Eqn. (41), the result is a series which is convergent with respect to both m and k.

This group of terms, as in the steady flow case[1], represents the wakes shed by the blades. In the present case, the wakes contain both trailing vorticity produced by radial gradients in the circulation, and shed vorticity created by the fact that the circulation is now varying in time as well. Since the manipulations described above are quite similar to those used in Ref. 1, but somewhat lengthier, they are not reproduced here. The end result for v_n is:

$$v_n(r,\zeta,z) = \frac{-B\delta_{p_o}}{2\pi\rho_o U_R r}\int_o^z d\bar{z}_o\, e^{i\frac{\omega}{U}(\bar{z}_o - z)}\,\Delta p(\sigma,\bar{z}_o)$$

$$+\frac{B\left(\frac{\Omega r}{U}\right)^2\delta_{p_o}}{2\pi\rho_o U_R r}\int_o^z d\bar{z}_o\, e^{i\frac{\omega}{U}(\bar{z}_o - z)}\sum_{k=1}^{\infty}\int_h^1 d\sigma_o\,\frac{\frac{\partial}{\partial\sigma_o}\left(\sigma_o\frac{\partial\Delta p}{\partial\sigma_o}\right)R_{ok}(\sigma_o)\,R_{ok}(\sigma)}{K_{ok}^2+\left(\frac{\omega r_T}{U}\right)^2}$$

$$+\frac{B}{2\pi\rho_o U_R r}\int_{r_H}^{r_T} d r_o \int_o^z d z_o \sum_{\substack{m=-\infty \\ n\neq 0}}^{\infty} e^{in\zeta + i\frac{\omega}{U}(z_o - z)} \sum_{k=1}^{\infty} \frac{R_{nk}(\sigma)\, R_{nk}(\sigma_o)}{\left[\left(\frac{K_{nk}}{n}\right)^2 + \left(\frac{n\Omega+\omega}{nU} r_T\right)^2\right]}$$

$$\cdot \left\{\left[1 + \left(\frac{\Omega r}{U}\right)^2 + \frac{1}{n}\left(\frac{\omega r}{U}\right)\left(\frac{\Omega r}{U}\right)\right]\frac{1}{n^2}\frac{\partial}{\partial r_o}\left(r_o \frac{\partial \Delta p}{\partial r_o}\right)\right.$$

$$\left. - \frac{1}{n^2 r_o}\left[\left(\frac{\omega r_o}{U}\right)^2\left(1 + \left(\frac{\Omega r}{U}\right)^2\right) + \left(\frac{\omega r}{U}\right)\left(\frac{\omega r_o}{U}\right)\left(\frac{\Omega r}{U}\right)\left(\frac{n\Omega+\omega}{nU} r_o\right)\right]\Delta p(r_o, z_o)\right\}$$

$$- \frac{B\left[1 + \left(\frac{\Omega r}{U}\right)^2\right]}{2\pi\rho_o U_R r}\int_o^z d z_o \sum_{\substack{m=-\infty \\ n\neq 0}}^{\infty} e^{in\zeta + i\frac{\omega}{U}(z_o - z)} \sum_{k=1}^{\infty} \frac{R_{nk}(\sigma)}{\left[\left(\frac{K_{nk}}{n}\right)^2 + \left(\frac{n\Omega+\omega}{nU} r_T\right)^2\right]}$$

$$\cdot \left\{ \frac{-2\left(\frac{\omega r_o}{U}\right)\left(\frac{\Omega r_o}{U}\right)}{n^3\left[1 + \left(\frac{\Omega r_o}{U}\right)^2\right]^2} \Delta p(r_o, z_o)\, R_{nk}(\sigma_o)\Big|_{r_H}^{r_T} \right.$$

$$+ \int_{r_H}^{r_T} d r_o \frac{\left(\frac{\omega r_o}{U}\right)\left(\frac{\Omega r_o}{U}\right) R_{nk}(\sigma_o)}{n^3\left[1 + \left(\frac{\Omega r_o}{U}\right)^2\right]}\left[\frac{\partial}{\partial r_o}\left(r_o \frac{\partial \Delta p}{\partial r_o}\right) + \frac{4}{1 + \left(\frac{\Omega r_o}{U}\right)^2}\frac{\partial \Delta p}{\partial r_o}\right.$$

$$\left. + \frac{4\left[1 - \left(\frac{\Omega r_o}{U}\right)^2\right]}{\left[1 + \left(\frac{\Omega r_o}{U}\right)^2\right]^2}\frac{\Delta p}{r_o}\right]$$

$$\left. - \int_{r_H}^{r_T} d r_o \frac{\left(\frac{\omega r_o}{U}\right)\left(\frac{\Omega r_o}{U}\right) R_{nk}(\sigma_o)}{1 + \left(\frac{\Omega r_o}{U}\right)^2}\left[\frac{2}{n^2}\left(\frac{\omega r_o}{U}\right)\left(\frac{\Omega r_o}{U}\right) + \frac{1}{n^3}\left(\frac{\omega r_o}{U}\right)^2\right]\frac{\Delta p}{r_o}\right\}$$

$$- \frac{B}{4\pi\rho_o U_R}\int_{r_H}^{r_T} d r_o \int_o^{c_a} d z_o \sum_{m=-\infty}^{\infty} \sum_{k=0}^{\infty} \frac{R_{nk}(\sigma)\, R_{nk}(\sigma_o)\, e^{in\zeta}}{\lambda_{nk}\left[(K_{nk})^2 + \left(\frac{n\Omega+\omega}{U} r_T\right)^2\right]}$$

$$\cdot \left\{\lambda_{nk}\left[g(r)\, g(r_o) - \frac{\left(\frac{\Omega r}{U}\right)\left(\frac{\Omega r_o}{U}\right)}{\beta^2}\left[\left(\frac{K_{nk}}{r_T}\right)^2 + \left(\frac{n\Omega+\omega}{U}\right)^2\right]\right] \operatorname{sgn}(z - z_o)\right.$$

$$+ i\left[\left(\frac{n\Omega+\omega}{\beta^2 U}\right)\left[f(r)\, f(r_o) - \left(\frac{\Omega r}{U}\right)\left(\frac{\Omega r_o}{U}\right)\lambda_{nk}^2\right] - \lambda_{nk}^2\left[\left(\frac{\Omega r_o}{U}\right) f(r)\right.\right.$$

$$\left.\left. + \left(\frac{\Omega r}{U}\right) f(r_o)\right]\right]\right\} e^{i\left(\frac{n\Omega + M^2\omega}{\beta^2 U}\right)(z - z_o) - \lambda_{nk}|z - z_o|} \Delta p(r_o, z_o) \qquad (63)$$

where it should be recalled that $n = mB + p$ and $\lambda_{n\ell}$, $f(r)$ and $g(r)$ are defined in (44), (55) and (59), respectively.

The above expression contains only convergent series. The first two lines are the contributions to the wake from the axisymmetric modes, $n = 0$. From the relation between n and m we see that such modes can arise only from the $m = 0$ term, and then only in the special case $p = 0$ i.e., zero phase lag between blades. Accordingly, these are written with the Kronecker delta symbol, δ_{p0}, which is one when $p = 0$ and zero otherwise. The next eight lines are the contributions to the wake terms from the $|n| > 0$ modes. All of the wake terms contain the exponential factor $e^{in\zeta - i\frac{\omega}{U}(z - z_0)}$, as well as the implied $e^{i\omega t}$ time dependence. Along the undisturbed helical streamlines (ζ = constant), this can be rewritten as

$$e^{in\zeta + i\omega\left[t - \frac{(S - S_0)}{U_R}\right]}$$

Thus, an observer moving in this direction with velocity U_R senses a frozen velocity pattern from these terms. This reflects the fact that, in a linearized analysis, the wakes convect downstream unattenuated at the freestream relative velocity.

The last four lines in Eqn. (63) represent the wave field that propagates away from the rotor in both directions. This consists of both damped and undamped waves, or modes; whether a particular mode is damped or not is determined by the cut-off criterion described by Eqn. (44). The modes above cut-off represent a loss of energy through acoustic radiation. Hence, a useful by-product of the linearized analysis is that it will also predict the total flux of acoustic energy, as well as its distribution among the various propagating duct modes.

The only steps remaining in the formulation of the unsteady integral equation are to specialize Eqn. (63) to the reference blade surface, $\zeta = 0$, and to specify the normal velocity there, $v_n(r, \zeta = 0, z)$, in terms of some prescribed excitation. The latter is accomplished by requiring that at each instant the streamlines remain tangent to the blade surface. The excitation

could be an inflow distortion pattern, such as might result from the wakes of an upstream blade row or distortions in the engine inlet itself. Or, v_n could be considered to be the result of vibrations of the blades themselves, i.e., the so-called flutter problem.

In any event, once the left-hand side of Eqn. (63) is prescribed, the integral equation which results must be inverted to obtain the unknown loading amplitude, Δp . Generally speaking, at each point there will be a phase shift between the unsteady loading and the normal velocity which will depend on position, reduced frequency, and Mach number. This was not true in the steady flow problem, where by definition everything is "in phase." To account for this, Δp must now be allowed to be a complex quantity, having both real and imaginary parts. What we actually have to solve then, is two integral equations, one each from equating the real and imaginary parts of Eqn. (63).

Equation (63) is far too complicated to hope for an analytical solution, and so a numerical inversion procedure must be developed. At present, it appears an extension of the procedure applied in Section I to the steady problem should work here as well. Specifically, Δp would be expanded in the same finite series as in Eqn. (12), except that now the unknown coefficients would be complex. In addition to automatically satisfying the appropriate leading and trailing edge conditions, use of this expansion will again lead to greater efficiency in computing the axial and radial integrations in (63). The axial integrations will be of the same form as in Eqn. (14), although the form of the constant parameters will change somewhat. Thus, the analytical evaluation procedure given in Appendix C can again be used to good advantage.

The majority of terms in Eqn. (63) will also lead to radial integrations of the same form as in (13). The exceptions are those portions of the wake terms which involve reciprocal powers of $\left[1 + \left(\frac{\Omega r_0}{U} \right)^2 \right]$; however, such factors vary monotonically from hub to tip, and so should be expressible as a finite series of integral powers of $\sigma_0 = r_0 / r_T$ with a high degree of accuracy. Hence, we believe that the radial integrations could again be performed analytically, as outlined in Appendix B.

If NI x NJ terms are retained in the expansion for $\Delta\phi$, we would have a total of 2 x NI x NJ scalar unknowns. Substituting this expansion into the integral equations described above, and evaluating the resulting set of equations at an equal number of collocation points, will yield a system of 2 x NI x NJ simultaneous, linear, algebraic equations. These can again be viewed as a single matrix equation, with the elements of the coefficient matrix being expressed in terms of the axial and radial integrations discussed above. The inversion of the matrix equation could then be carried out in a straightforward manner using standard techniques.

F. CONCLUSIONS

A linearized three-dimensional analysis has been developed for studying the unsteady loading on an annular blade row in compressible flow. Pressure dipole singularities are used to represent the blades in a lifting-surface type analysis. The result is an integral equation which relates the unknown loading to the prescribed variations in normal velocity at the blade surfaces. The latter can be the result of either an inflow distortion pattern or vibrations of the blades themselves. Terms can be identified in the integral equation which represent the blade wakes. These include elements of both trailing vorticity, produced by spanwise loading gradients, and shed vorticity, which results from the temporal fluctuations in loading. The wakes can be shown to convect downstream along the helical undisturbed stream surfaces. Also included are terms which represent waves propagating unattenuated away from the blade row in both directions. This acoustic radiation field would be predicted as a by-product of the solution, with regard to both total acoustic energy flux, and its distribution among the various propagating duct modes.

The unsteady integral equation, though somewhat more complicated than the analogous steady flow equation discussed in Section I, contains axial and radial integrations of the same basic analytical form. This suggests that a suitable extension of the numerical inversion procedure developed for the steady case should work here as well, and this is the approach that is being pursued.

SECTION III

FURTHER COMPARISONS OF APPROXIMATE ROTOR-STATOR INTERACTION THEORY WITH ACOUSTIC DATA FROM ANNULAR CASCADE

A. INTRODUCTION

Under the previous contract, an approximate theoretical model was developed to predict the noise generated by rotor-stator interaction.[1] In order to assess the accuracy of this theoretical model, experimental acoustic data were obtained in an annular cascade facility upstream of a rotor-stator pair, and compared with the theoretical predictions. Unfortunately, power constraints on the rig restricted the acoustic tests to low rpm where only the fourth and higher harmonics could propagate undamped in the duct. The prediction of these tones was felt to be a rather severe test of the theory. While the theory was able to predict cut-off frequencies and follow relative trends in the data adequately, it significantly underestimated absolute levels.

Additional numerical studies using the theory showed that the prediction of such high harmonics is critically dependent on the assumed shape for the rotor blade wakes. Very small changes in assumed wake shape can lead to large changes in the predicted noise levels, particularly for the higher harmonics. The approximate theory relies on isolated airfoil data for the wake shapes. It may be that the prediction of interference noise at these high harmonics of blade passage frequency cannot be accomplished in any practical sense until we are able to predict the wake structure to a much higher degree of accuracy.

On the other hand, because of the much higher rpm at which typical aircraft fans and compressors operate, it is the fundamental blade passage frequency, and perhaps its second harmonic, which account for most of the noise problem. At such speeds, the higher harmonics fall outside the range of human hearing. The theory indicated that the first few harmonics of blade passage frequency are relatively insensitive to the shape of the rotor blade wakes and that the level of the interaction noise at these harmonics, if excited, will be

much larger than the levels of the higher harmonics. Therefore, it was felt that a more reasonable test of the theory would be to compare its predictions against data taken for the lower harmonics. This required modifying the drive mechanism in the annular cascade so that higher speeds could be achieved. The repowered rig and the experimental procedures are described in Section III-B, followed by comparisons with the theoretical predictions in Section III-C.

B. ROTOR-STATOR INTERACTION NOISE MEASUREMENTS

1. Rotating Annular Cascade Facility

As part of the work under a previous program, Contract AF33(615)-3357, an annular cascade facility was designed and fabricated. Its principal purpose is to provide fundamental experimental data during and prior to the occurrence of rotating stall in order to improve our understanding of the phenomena and for use as a guide in improving the theoretical rotating stall analysis. In addition to the study of rotating stall, the facility has also been used to provide acoustic data for comparison with theory. A detailed description of the annular cascade facility has been presented in Ref. 31. Only a brief description of the facility is given here.

The annular cascade facility consists of a test section built around the outer front casing of a J-79 jet-engine compressor with a Calspan fabricated hub. The facility includes a bell-mouth inlet on the outer casing and a bullet nose on the hub to provide a smooth flow of air to the test section. Outlet ducting is connected to an independently variable source of suction to provide the required flow through the annulus. An electrically powered two-speed axial flow fan is used as the source of suction. Continuous control of the mass flow is achieved through the use of variable inlet guide vanes to the fan and a variable damper in the fan exit flow.

The configuration of the annular cascade used for the rotor-stator interaction studies is shown in Fig. 14. The test section forms a circular annulus with an outer diameter of 29.35 inches and an inner diameter of 23.35 inches which provides a hub-to-tip ratio of 0.80. The rotor-stator stage studied is designated Rotor Set No. 1 (46 blades) and Stator Set No. 1 (54 vanes) in Ref. 31. These are modified blade rows from the fifth stage of a J-79 compressor. Their characteristics and performance when used as isolated blade rows in the annular cascade have been presented in Ref. 31. The semi-chords of the rotor and stator were 0.0604 ft. and 0.054 ft., respectively, and the axial separation of the mid-chord planes was 0.125 ft. The mid-annulus stagger angle of the rotor was 40 degrees in all tests. Two different stator stagger angles (37.2 and 28.2 degrees) were tested.

The rotor in the annular cascade is driven by a hydraulic motor. An external hydraulic pump system is used to provide power for the hydraulic motor. In the tests of Ref. 1, the hydraulic pump system was powered by a 30 horsepower electric motor. With this system, the maximum rotor speed attainable was 1450 rpm. This speed was insufficient to allow propagation of sound at the fundamental blade passage frequency. It was calculated that an increase in rotor speed from the maximum of 1450 rpm attained in the past experiments to approximately 1700 rpm should be sufficient to exceed the cut-off condition for propagation of the fundamental blade passage tone in the rotor-stator stage. Since the time that the past experiments were performed, the rotating annular cascade was modified to include a 50 horsepower hydraulic pump system in the rotor drive, and changes were made to reduce pressure losses in the hydraulic valve system used for rotor speed control. With these changes, a maximum rotor speed of 1760 rpm was attained. Acoustic tests in the modified annular cascade succeeded in exciting the fundamental as well as higher harmonics of blade passage frequency.

2. Acoustic Measurements

The Sound Pressure Levels produced by rotor-stator interaction were measured on the outer casing upstream of the rotor. In taking these data, the fan system downstream of the annular cascade was turned off and the fan was

allowed to rotate freely under the influence of the flow generated by the rotor in the annular cascade. In addition, all dampers in the downstream drive system were opened wide. It was convenient to use this wide open configuration because it was found to provide nearly constant inlet swirl angles relative to the rotor. That is, the mean axial velocity in the annular cascade increased in direct proportion to the rotor angular velocity. This feature made application of the rotor-stator interaction theory much simpler because the dimensionless steady state loss and turning performance data for the rotor also remained approximately constant with changing rotor speeds.

The instrumentation used for the acoustic tests is shown schematically in Fig. 15. A Bruel and Kjaer (B&K) condenser microphone (Type 4133) mounted with its diaphragm flush with the inner surface of the compressor casing (Fig. 14) was used to measure the rotor-stator interaction noise. The microphone was powered by a B&K Type 2604 microphone amplifier. The output from the amplifier was processed on line by a General Radio Type 1921 real time analyzer to obtain one-third octave spectra of the signals. Absolute calibration of the complete system was obtained by recording a 114 db signal from a General Radio Type 1562-A sound level calibrator on the recorder chart of the spectrum analyzer. The calibration signal was recorded at the start of a test series and again at the end of a test series to check for drift of the system. The observed drift was 0.5 db or less in all tests.

The summed output from the multifilter in the GR real time analyzer was displayed on a dual beam oscilloscope along with a reference signal from an RC oscillator. The multifilter summed output was conditioned by attentuating all one third-octave levels with center frequencies of 500 Hz and below. This was done to reduce noise at frequencies less than the fundamental blade passage frequency. Oscilloscope records of the conditioned noise signal are shown in Fig. 16. In these photographs, the lower trace is the noise signal and the upper trace is the output from the RC oscillator tuned to the same frequency as the predominant noise harmonic. The jitter in the noise signals is caused by the presence of frequencies other than the predominant harmonic. Tuning of the audio oscillator was accomplished by setting the oscilloscope trigger mechanism to fire on the audio oscillator signal and then adjusting the oscillator

frequency until a stationary noise signal was attained. In some tests, the correct frequency was difficult to determine because of the jitter in the noise signal. The correct frequency was then determined by forming a Lissajous figure from the noise and oscillator signals, and tuning the oscillator frequency until a stationary Lissajous figure was obtained. The frequency was then read on a Berkley universal counter and timer. A similar counter was used to determine the rotor speed from signals generated by a magnetic pickup and 120 tooth gear on the rotor drive shaft.

The procedure described in the previous paragraph was used to determine the frequency of the predominant pure tone noise for all tests where a strong blade row interaction signal was obtained. Thus, it was possible to identify accurately which harmonic of rotor blade passage frequency was being excited by the interaction mechanism. In the upper photograph of Fig. 16, the predominant frequency is the fundamental of blade passage frequency. In the lower photograph, both the fundamental and second harmonic of blade passage frequency are apparent.

Samples of the one-third octave spectra of the interaction noise are shown in Figs. 17 and 18. These figures are direct reproductions of the output from the spectrum analyzer. Absolute Sound Pressure Level for any one-third octave band is obtained by correcting the relative db levels for background noise, system gain, microphone response and filter characteristics. The system gain correction is independent of frequency and is noted on the lower left hand side of each figure. For the particular example of Fig. 17, system gain is corrected for by adding 80 db to all relative levels. For Fig. 18, the gain correction is 80.5 db. The remaining corrections will be discussed shortly.

Figures 17a through 17c have been chosen to illustrate the extremely sharp rise in interaction noise as rotor speed is increased over a very small range of rpm from below cutoff to above cutoff of the fourth rotor blade passage harmonic. Figure 17a corresponds to conditions slightly below cutoff. Here the noise spectrum is generated primarily by turbulent pressure fluctuations within the boundary layer on the outer wall and by the free-wheeling fan downstream of the annular cascade test section. Figs. 17b and 17c show the sharp

rise in fourth harmonic interaction noise as the rotor rpm increased to above cutoff conditions. This rise can be seen in the third octave bands centered at 3150 and 4000 Hz. Both of these third octave bands respond because the pure tone frequency is nearly mid-way between these two bands. The calculated frequency of the fourth harmonic is indicated by an arrow on the spectra; the numerical value is shown on the lower right hand side of Figs. 17a through 17c. The corresponding measured pure tone frequency is also indicated on Figs. 17b and 17c.

Figs. 18a through 18d are spectra obtained at rotor speeds sufficient to excite the fundamental blade passage frequency. Here the fundamental frequency and the second and fourth harmonics are apparent in the spectra. In Fig. 18a the fundamental frequency is predominant and smaller Sound Pressure Levels are evident at the second and fourth harmonic frequencies. When the rotor speed is increased by five rpm (Fig. 18b), the second harmonic disappears into the background noise. When the rotor speed is again increased by small amounts (Figs. 18c and 18d), the second harmonic grows rapidly while the fundamental harmonic decays. The oscilloscope records in Fig. 16 correspond to the spectra presented in Figs. 18a and 18c. The rapid growth and decay of Sound Pressure Levels at various harmonics of blade passage frequency with small changes in rotor speed was observed throughout the complete test series.

As noted earlier, the relative Sound Pressure Levels obtained from spectra such as those shown in Figs. 17 and 18 require several corrections in addition to the correction for system gain. These are as follows:

(a) Background Level Correction - The Sound Pressure Levels in the third-octave bands contain contributions from the background noise levels as well as the pure tone noise from rotor-stator interaction. The background noise level was estimated by inspection of the third-octave bands adjacent to those responding to the various harmonics of blade passage frequency. An example of the procedure is shown in Fig. 18a. In this case, the relative background level for the third-octave band centered at 1250 Hz is estimated

by drawing a straight line between the spectrum levels centered at 1000 Hz and 2000 Hz. This line intersects the 1250 Hz band at a spectrum level of 31.5 db. The spectrum level at the third-octave band centered at 1600 Hz was not used in this case because it contains some contribution from the fundamental blade passage frequency. Ignoring the spectrum level at 1600 Hz makes very little difference to the background correction in this case. If the measured spectrum level is designated S_M and the background level B_M, then the corrected spectrum level is given by

$$\text{SPL Corrected for Background} = 10 \log \left[\log^{-1} \frac{S_M}{10} - \log^{-1} \frac{B_M}{10} \right] \text{db}$$

or equivalently

$$\text{Background Correction} = 10 \log \left[1 - 10^{-(\Delta \text{db}/10)} \right] \text{db}$$

where

$$\Delta \text{db} = S_M - B_M \quad \text{db}$$

The background correction is shown as a function of Δdb in Fig. 19, which is the same as Fig. 6-3 of Ref. 32.

(b) Filter Correction - At constant rotor speed, the rotor-stator interference noise at the various harmonics of blade passage frequency are essentially pure tones at specific frequencies. If the frequency of these pure tones does not correspond to one of the center frequencies in the third-octave filters of the real time analyzer, then the measured third-octave level will be lower than the pure tone level by an amount depending on the ratio between the pure tone frequency and the third-octave center frequency. This arises because of the characteristic shape of the third-octave filter curve. The measured response of the filters in the real-time analyzer used in these tests is shown in Fig. 20. This curve is an average of the results obtained for filters with three different center frequencies, f_o. The measured noise data for a harmonic frequency, f, were corrected by using this curve to determine the attentuation of the filter at the appropriate frequency ratio, f/f_o. When two third-octave bands responded at

approximately equal levels, such as shown in Figs. 17b and 17c, both values of measured third-octave levels were used separately to estimate the correct pure tone sound pressure level (using the correct values of f/f_o for each band). In these cases, the two answers generally agreed to within 1 db or better.

(c) Microphone Response Correction - The frequency response of the B&K condenser microphone was not completely flat in the frequency range above 1000 Hz. This is shown in Fig. 21. The lower curve in this figure is the appropriate curve for the microphone flush-mounted in the annular cascade without its protection grid. The overall system gain was set by using the 114 db GR sound level calibrator at a frequency of 1000 Hz. Thus the lower curve in Fig. 21 can be used directly to correct the results for microphone response at the harmonic frequencies of interest.

Numerical examples of the data reduction technique are given in Tables 2 and 3 for the spectra presented in Figs. 18a and 17c. The example in Table 2 is for a spectrum in which several harmonics of blade passage frequency are present in separate third-octave bands. The example in Table 3 is for a spectrum in which two adjacent third-octave bands are responding at nearly equal levels to the same harmonic of blade passage frequency. In this case, the data for both third-octave bands have been analyzed to show the possible error when the pure tone frequency is not near any of the center frequencies. The results from separate analysis of the data from the two third-octave filters are 128.1 db and 127.3 db. This is within the 1 db difference mentioned previously for such cases.

The results of the interaction noise measurements are presented in Figs. 22 through 29. Each figure shows the corrected SPL of a particular blade passage harmonic as a function of rotor speed. The approximate background noise levels are also shown in each figure. The small downward facing arrows in these figures indicate points where the spectrum levels were low enough to be obscured by the background level. Spectrum levels within 3 db of the background contain background level corrections which exceed 1 db and should be considered as highly approximate in view of the method used to estimate the background noise.

Table 2

SAMPLE OF ACOUSTIC DATA REDUCTION FOR
SPECTRUM WITH MULTIPLE HARMONICS OF BLADE PASSAGE FREQUENCY

Rotor RPM = 1695.5 (See Fig. 18a)

Blade Passage Frequency (46 blades) = $46 \times \frac{1695.5}{60} = 1300$ Hz

Blade Passage Harmonic	1	2	3
Harmonic Frequency, f(Hz)	1300	2600	5200
Third-Octave Center Frequency, f_o(Hz)	1250	2500	5000
Frequency Ratio, f/fo	1.040	1.040	1.040
Measured Spectrum Level, S_M (Relative db)	52.2	35.0	34.2
Estimated Background Level, B_M (Relative db)	31.5	30.7	29.7
$S_M - B_M$ (db)	20.7	4.3	4.5
Background Correction (db) (Fig. 19)	0	-2.0	-1.9
S_M Corrected for Background (Relative db)	52.2	33.0	32.3
System Gain Correction (db)	+80.5	+80.5	+80.5
Filter Correction (db) (Fig. 20 for f/f_o=1.040)	+0.2	+0.2	+0.2
Microphone Response Correction (db) (Fig. 21)	+0.2	+0.6	+1.8
Final Corrected Sound Pressure Level (db)	133.1	114.3	114.8

Table 3

SAMPLE OF ACOUSTIC DATA REDUCTION FOR SPECTRUM WITH TWO ADJACENT THIRD-OCTAVE BANDS RESPONDING NEARLY EQUALLY TO THE SAME HARMONIC OF BLADE PASSAGE FREQUENCY

Rotor RPM = 1160.5 (See Fig. 17c)

Blade Passage Frequency (46 blades) = $46 \times \frac{1160.5}{60} = 889.7$ Hz

Fourth Harmonic of BPF, f = 3559 Hz

Third Octave Center Frequency, f_o (Hz)	3150	4000
Frequency Ratio, f/f_o	1.130	0.890
Measured Spectrum Level, S_M, (Relative db)	41.6	43.0
Estimated Background Level, B_M, (Relative db)	23.7	23.3
$S_M - B_M$ (db)	17.9	19.7
Background Correction (db) Fig. 19)	-0.1	0
S_M Corrected for Background (Relative db)	41.5	43.0
System Gain Correction (db	+80.0	+80.0
Filter Correction (db) (Fig. 20)	+5.5	+3.2
Microphone Response Correction (db) (Fig. 21)	+1.1	+1.1
Final Corrected Sound Pressure Level (db)	128.1	127.3

All of the acoustic measurements were made with the rotor stagger angle held constant at 40 degrees. However, two stator stagger angles were used. Figs. 22 through 25 show the data measured with a stator stagger angle of 37.2 degrees while Figs. 26 through 29 show similar data with a stator stagger angle of 28.2 degrees. Data were obtained for the fundamental blade passage frequency and the second, fourth and fifth harmonics. The third harmonic was detected in only two of the 195 spectra obtained in the complete test series. These two data points are shown in Fig. 27 along with the second harmonic data measured with a stator stagger angle of 28.2 degrees. There is evidence that the third harmonic was present at similar rotor speeds ($\approx$ 1675 rpm) with a stator stagger angle of 37.2 degrees. However, its level in that case was not strong enough to analyze with any degree of accuracy.

In Ref. 1, interference noise data were presented for the same rotor-stator configuration in the annular cascade as used in the current test program. The maximum rotor speed attained in those past tests was 1450 rpm. Only the fourth and fifth harmonics of blade passage frequency propagated at these low rotor speeds. However, since the annular cascade had been disassembled, modified to increase available power, and reassembled between tests, it is worth mentioning that the current test results agree quite well with the past test results in the region where the two sets of data overlap.

It is evident from the results that the modified annular cascade attained rotor speeds high enough to excite the fundamental as well as higher harmonics of blade passage frequency. Thus the experimental acoustic study succeeded in its goal of providing data at low harmonics of blade passage frequency for comparison with the rotor-stator interaction noise theory. Comparisons between this theory and the experimental results are presented in the following sub-section.

C. COMPARISONS WITH THEORY

1. Theoretical Model And Input Data

The details of the rotor-stator interaction noise theory were presented in Ref. 1, along with the earlier comparisons to data at the fourth and fifth harmonics of blade passage frequency. The acoustic model assumes that the rows are housed in an infinitely long, hard-walled annular duct of constant hub/tip ratio. Each row is represented by a three-dimensional array of radially-oriented line dipoles, whose strength is fluctuating in time. The resulting acoustic field is represented as a superposition of propagating duct modes of the type studied by Tyler and Sofrin.[15] Reflections from neighboring blade rows or terminations of the duct are thus neglected.

The strength of the fluctuating dipoles is determined from the rotor-stator interaction analysis of Osborne,[33] which is an extension to compressible flow of the classic incompressible model of Kemp and Sears.[34,35] This is a two-dimensional model which assumes that the unsteady aerodynamic response of both the rotor blades and stator vanes can be calculated as though they operate as isolated airfoils.[36] The results of Osborne's analysis are closed form expressions for the fluctuating lift produced by each of three interaction mechanisms: unsteady lift on the rotor produced by the steady field of the stator, unsteady lift on the stator produced by the steady field of the rotor, and unsteady lift on the stator produced by the impingement of the rotor viscous wakes. The first two are usually termed potential interactions, and the last a viscous interaction. These fluctuating lift predictions, since they are two-dimensional, are input on a strip theory basis to the three-dimensional acoustic model described above.

The overall theory that results can predict the total acoustic energy flux away from the stage in either direction, the Sound Pressure Level (SPL) at any point in the duct, and the individual mode amplitudes. The inputs required are the steady loading on both rows, which is used in the potential

interaction calculations, and the drag coefficient of the upstream rotor blades, which is used to infer the wake velocity defect for the viscous interaction. As part of a larger study of rotating stall phenomena,[37] data were obtained on the circumferentially-averaged turning performance and total pressure loss across the rotor operating alone. Viscous losses across the stator were assumed negligible, and its turning performance estimated from the manufacturer's design data. The earlier comparisons used this information to calculate approximate values for the inputs required by the theory, using Eqns. (36)-(43) of Ref. 1.

The same procedure as in Ref. 1 was used in the latest series of comparisons, except that the reliability of our input data was improved in several respects. The main improvement is that we now have data on the total pressure loss across the rotor in the presence of the stator,[38] whereas before our only data was for the isolated rotor. As a result, the predicted C_D of the rotor blades now lies in the range 0.05 - 0.07, which is much more reasonable than the value 0.16 which had been predicted from the isolated rotor data.[1] We also now have data on the total pressure loss across the stator operating as part of the stage,[38] whereas before no data on the stator were available. Although not needed for the viscous interaction calculation, this loss does play an indirect role in estimating the stator steady lift (see Eqn. (42) of Ref. 1). The estimates of stator turning performance are now based on extrapolations of turning data measured on the isolated stator row in the annular cascade,[1] whereas in the earlier study manufacturers design data were used to estimate stator turning.[1] As before, we had to rely on isolated rotor turning performance due to the difficulties involved in trying to instrument the small gap between rotor and stator.

2. Discussion

The present calculations once again indicate that it is the rotor viscous wakes impinging on the stator which is the dominant noise generation mechanism. The SPL predictions for the mean stator stagger angle of 28.2°

are compared with the newly acquired data for the first through fifth harmonics of blade passage frequency in Figs. 30a-d. The gaps in the experimental data are those regions in which the signal was close enough to the background level that no reliable level could be inferred, as discussed in Section III-B. In each figure, the rotor rpm at which the various duct modes first propagate is indicated by a right-facing arrow with a pair of integers which denote the azimuthal and radial mode numbers, respectively. It should be recalled that right at the cut-off rpm the mode amplitude is theoretically infinite, since no attempt was made to include viscous or nonlinear effects in the model.[1] Thus not much significance should be attached to the height of the theoretical peaks in this vicinity, as they are determined primarily by how closely one wishes to approach the cut-off rpm. Generally, the calculations were made at increments of 50 rpm, with closer spacing near the cut-offs to better exhibit where the modes first begin to propagate.

Once again, the highest harmonics are underestimated as shown by Figs. 30c, d, although the agreement is not bad at the higher rpms in these two cases. Note that this is because the theory shows a definite increase in SPL with rotor speed, as one would expect intuitively, whereas the average level of the fourth harmonic data changes little, and the fifth harmonic data show only a slight rise. In general, one can also reasonably correlate the location of the theoretical peaks near cut-off with those in the experiments. However, the data do show much more of a peak/valley structure than does the theory. No firm explanation is apparent for this, although it may be the result of the reflection/transmission of the acoustic signals by the upstream rotor, which is not accounted for in the theory.

Curiously, the comparisons at the lower harmonics, Figs. 30a, b, show a reversal in the levels of theory and experiment. The predictions are now too high over the entire range in which data could be taken, which was limited again by power constraints. The cut-on of the second harmonic is reasonably well predicted; little can be said of the third harmonic because of the very limited range in which it could be distinguished in the third-octave band spectrum. A notable feature of the comparisons appears at the

that the level of the interaction noise at these harmonics, if excited, will be

fundamental blade passage frequency; not only are the predictions too high, but the data show that the fundamental is propagating in the duct well before the theory would predict, at least on the basis of rotor-stator interaction. From the present data one cannot tell whether the fundamental first cuts on at about 1490 rpm, or whether it had been present before, but below the background level (see Fig. 26). In any event, this strongly suggests that another noise generation mechanism besides rotor-stator interaction may be influencing the data. This will be discussed further below.

The comparisons of theory with experimental data at the mean stator stagger angle of 37.2° are shown in Figs. 31a-d. Qualitatively, the comparisons exhibit the same features as those for the other stator setting. The predictions for the fourth and fifth harmonics are too low, though the agreement at the higher rpms is not bad in the case of the fourth. The lower harmonics are overestimated, though to a lesser degree than before. Again, the fundamental is detectable well before the theory indicates it should propagate.

As noted in connection with the comparisons done under the previous program,[1] one plausible explanation for the poor agreement at the higher harmonics is the assumed shape for the viscous wake profiles. At present, the model uses a profile correlation which is based on the isolated airfoil data of Silverstein, et al.[39] It was demonstrated in Ref. 1 that alternate correlations of the same data would produce significant changes in the theoretical SPL levels of the higher harmonics. This is basically because the high harmonic content of the wake profiles, and hence the noise, is determined to a great extent by the rate at which the velocity defect approaches zero near the edges of the wake, and this is difficult to define experimentally. Thus, it may be that reliable predictions of viscous interaction noise in the higher harmonics will have to await the development of means to predict the wake structure with more precision.

In a practical sense, the inability to predict higher harmonic levels is of secondary interest. It is the fundamental, and perhaps second

harmonic, which is most directly responsible for the noise problem at the higher speeds at which aircraft engines operate. Here the theory consistently overestimates the noise levels. This cannot be explained on the basis of inadequate knowledge of the wake profile structure; as demonstrated in Ref. 1, the lowest harmonics are insensitive to the particular choice of profile correlation. They are, however, sensitive to the prediction of the wake centerline velocity defect, i.e., the height of the wake profile. This also was correlated on the basis of the isolated airfoil data in Ref. 39. More recent experimental investigations have been accumulating data on the wake structure of both two-dimensional cascades[40,41] and three-dimensional rotors.[42,43] The cascade data of Ref. 40 indicate that the decay of the wake velocity defect with distance downstream of the trailing edge is slower than would be found behind an isolated airfoil. On the other hand, Kerrebrock et al[41] observed a faster rate of decay in the cascade data when compared with the isolated airfoil case. The studies done on three-dimensional rotor wakes[42,43] thus far have shown that they decay more rapidly than the wakes of either cascades or isolated airfoils.

Clearly, there is ample evidence to suggest that the present theory may be inaccurately modeling the rotor wake structure. Improved correlations with the present acoustic data would result if the centerline velocity defect was weaker than predicted, and the wake profile shape was sharper and narrower than that assumed. However, it is too early to say how generally applicable the data of Refs. 40-43 are to other configurations. In particular, the effects of such parameters as solidity, steady loading, and blade profile all need to be quantified. Lacking this, better knowledge of the wake structure in the present annular cascade facility would require an extensive series of measurements which were felt to be outside the scope of the present program.

Another possible source of error in the theory is the unsteady aerodynamic model. As pointed out earlier, Osborne's[33] model does include compressibility effects provided the Mach number and/or reduced frequency are

were measured on the outer casing upstream of the rotor. In taking these data, the fan system downstream of the annular cascade was turned off and the fan was

not too high. However, when applied at the low speeds of the present experiments, it reduces to the incompressible theory of Kemp and Sears.[34,35] The flow is assumed to be two-dimensional, with each blade or vane behaving as an isolated airfoil. For the high hub/tip ratio of the present experiments, the two-dimensional assumption is not unreasonable. However, the solidity ratio, defined as the ratio of chord length to tangential blade spacing, is approximately 0.85 for the stator at mid-annulus. Thus the effects of interference from neighboring stator vanes may not be negligible. Both of these questions, regarding the importance of three-dimensionality and blade-to-blade interference, could be answered by the type of analysis reported in Section II, which is still under development. The best means of assessing the aerodynamic model would be to make unsteady load measurements on the stator vanes and see how they compared with predictions. This was also felt to be outside the scope of the present work.

Finally, there is the question of why the fundamental blade passage frequency cuts on earlier in the experiments than the theory would indicate (Figs. 30a and 31a). This strongly suggests that noise is being generated through mechanisms other than rotor-stator interaction. The most likely possibility is that the rotor itself is interacting with a distortion in the inlet flow, perhaps the wakes produced by the upstream support struts shown in Fig. 14. Since the struts are streamlined and located about a foot and a half ahead of the rotor, one would expect that their wakes would be sufficiently diffuse by the time they reach it so as to have neglibible influence. Azimuthal surveys of the flow ahead of the rotor have been performed, but only in the presence of distortion screens which were used to study the influence of distortion on rotating stall.[31] Any strut generated distortion would have been masked by the presence of the screens.

Thus it seemed the most expeditious way to test this hypothesis was to remove the stator and see whether the isolated rotor still produced significant tone noise. (In the absence of inflow distortion, it should not radiate any noise at subsonic tip speeds.) When the rig was disassembled for

mechanism to fire on the audio oscillator signal and then adjusting the oscillator

this purpose, it was discovered that the chain drive used to drive the rotor had deteriorated and loosened considerably. Accordingly it was replaced, but the new drive generated sufficiently higher background noise levels than the old that further experiments on isolated rotor noise were not possible.

D. CONCLUSIONS

Our earlier comparisons of the rotor-stator interaction noise theory with experimental data taken in Calspan's annular cascade facility had shown that the theory consistently underestimated SPL at the fourth and fifth harmonics of blade passage frequency.[1] This was felt to be a rather severe test of the theory, as the higher harmonics were shown to be quite sensitive to details of the rotor blade wake profiles. However, power limitations in the rig at that time prevented operating at high enough rpm's to allow the lower harmonics to propagate. The main goal of this portion of the current contract was to provide, with a newly re-powered rig, comparisons between theory and data at the fundamental and first few harmonics. These comparisons have been made, and show that the theory consistently overestimates the noise in the fundamental and second harmonic; experimental data at the third harmonic was also lower than the theory, but was limited to too few points for any general conclusion to be drawn. Interaction of the stator with the viscous wakes shed by the rotor is predicted by the model to be the predominant noise generation mechanism; potential interactions between blade rows were found to be negligible.

The theoretical model was required to predict the viscous interaction noise based only on turning and loss performance data, since this is the type of information the designer is likely to have available. The overall model is thus a composite of three major elements: a model of the viscous wake structure; an aerodynamic model to predict the unsteady response of the downstream row to the wakes; an acoustic model to predict the resulting radiation. At present we know with certainty only that the end results do not

within the boundary layer on the outer wall and by the free-wheeling fan downstream of the annular cascade test section. Figs. 17b and 17c show the sharp

correlate well with the acoustic measurements. We strongly suspect that the weakest links in the model are the viscous wake modeling, and perhaps the unsteady aerodynamic model, for the reasons discussed above. Conclusive answers to these questions can be obtained only by performing extensive measurements of both the rotor wake structure and the unsteady loads produced on the stator vanes; however, such a program was well outside the scope of present effort.

Another surprising feature in the comparisons is that the fundamental blade passage frequency first appears at a lower rpm than predicted by the theory. This suggests that a noise generation mechanism other than rotor-stator interaction may have heavily influenced the data. One possibility is that the rotor itself may be interacting with a distortion in the flow, such as wakes from the upstream support struts, or perhaps a distortion in the inlet flow itself. No surveys have been made as yet of the flow uniformity ahead of the rotor, and attempts at measuring the noise output of the rotor with the stator removed were thwarted by high background levels from a newly installed drive mechanism. It is felt that one or both of these measurements should be made before conducting any further experiments on rotor-stator interaction in the annular cascade.

blade passage frequency. An example of the procedure is shown in Fig. 18a. In this case, the relative background level for the third-octave band centered at 1250 Hz is estimated

SECTION IV

SUMMARY

In Section I, a method is presented for computing the steady loading on a three-dimensional annular blade row in compressible flow, given the blade camber line. A kernel-function procedure is used to solve the linearized integral equation relating the unknown loading to the camber line slope. The greatest advantage of the solution procedure presented here is that it allows analytical expressions to be derived for both the spanwise and chordwise integrals which are required. It also allows the various aerodynamic and performance parameters of the rotor to be expressed as simple algebraic functions of the loading expansion coefficients.

Comparisons are presented between the predictions of the present theory and those of two-dimensional strip theory, as well as with the results of an inverse three-dimensional analysis. The three-dimensional and strip theories show consistently good agreement at mid-annulus, but the three-dimensional theory predicts loadings which are significantly higher near the hub and lower near the tip than the strip theory, thus giving much lower radial variations. Such behavior can be attributed to the induced angle of attack distribution generated by the trailing vortex wakes, which is not accounted for in strip theory; this smoothing appears to be the principle effect of three-dimensionality, at least for subsonic relative Mach numbers.

When coupled with the analogous treatment of the disturbance flowfield produced by blade thickness, the loading analysis presented here should provide an efficient means of studying three-dimensional effects in turbomachinery rows. The program should prove particularly advantageous for evaluating alternate blade camber lines at a given operating condition; thus, it could serve to narrow down the number of candidate blade profiles before going to a finite-difference solution of the full nonlinear equations. It could also prove useful in providing better initial conditions to a difference scheme, allowing the latter to converge in fewer iterations.

frequency ratio, f/f_o . When two third-octave bands responded at

In Section II, the linearized analysis is extended to the study of unsteady flow through a rotor, such as might be produced by inflow distortion or blade vibrations. An integral equation is derived which relates the unknown loading to the prescribed variations in normal velocity at the blade surfaces. Terms can be identified in the integral equation which represent the blade wakes. These include elements of both trailing vorticity, produced by spanwise loading gradients, and shed vorticity, which results from the temporal fluctuations in loading. Also included are terms which represent waves propagating unattenuated away from the blade row in both directions. This acoustic radiation field would be predicted as a by-product of the solution, with regard to both total acoustic energy flux, and its distribution among the various propagating duct modes. Though somewhat more complicated than the analogous steady flow equation, the form of the required integrations suggests that it can be solved by a suitable extension of the procedure developed in Section I.

Section III presents comparisons between a theoretical model of rotor-stator interaction noise, developed under a previous program, and a current series of acoustic measurements made in an annular cascade facility. Inputs required by the theory are the steady loading on both rows, which is used to predict the potential interactions, and the drag coefficient of the upstream row, which is used to infer the wake velocity defect for the viscous interaction. These were inferred from experimental measurements of the circumferentially-averaged turning performance and total pressure losses, respectively, across the blade rows.

Theoretical and experimental Sound Pressure Levels at one point in the duct upstream of a rotor-stator pair were compared from the fundamental blade passage frequency up through the fifth harmonic. The calculations indicate that the viscous wake interaction is the dominant noise generation mechanism. The theory overestimates the noise in the fundamental and second harmonic, while its predictions are too low for the fourth and fifth. The most likely sources of error in the theory are felt to be in the modeling of

the rotor viscous wakes and the unsteady aerodynamic response of the downstream stator vanes; the wake model is based on isolated airfoil data, while the aerodynamic analysis neglects the influence of neighboring vanes in the stator. Detailed wake survey and unsteady load measurements against which to test this hypothesis were outside the scope of the present effort. It also appeared that the experimental data may have been heavily influenced by noise generation mechanisms other than those considered in the rotor-stator interaction theory, including the possibility of the rotor interacting with the wakes shed by upstream support struts.

Appendix A.

EQUIVALENCE OF THE PRESSURE DIPOLE AND HORSESHOE VORTEX REPRESENTATIONS OF THE STEADY LOADING ON AN ANNULAR BLADE ROW.

The pressure dipole representation of the rotor used in the steady lifting-surface calculations can be shown to be equivalent to the vortex representation used by Okurounmu and McCune[5-7]. In order to demonstrate this, the present dipole representation is reinterpreted as a vortex representation, to which it must be equivalent if both are valid. The resulting vortex representation is then shown to be the same as that of Okurounmu and McCune.

First, the perturbation velocity potential of a lifting rotor is written in terms of the perturbation pressure, p , as follows:

$$\varphi = -\int_{-\infty}^{z} \frac{p(z', \zeta, r)}{\rho_\infty U} \, dz' \tag{A-1}$$

Writing the perturbation pressure as the superposition of dipole solutions and then interchanging the order of integration gives

$$\varphi = -\frac{1}{\rho_\infty U} \int_{-\infty}^{z} \int_{S_B} \Delta p(r_o, z_o) \, p_D(z', \zeta, r, z_o, r_o, \zeta_o) \, dS_B \, dz' \tag{A-2}$$

or

$$\varphi = -\frac{1}{\rho_\infty U} \int_{S_B} \Delta p(r_o, z_o) \left[\int_{-\infty}^{z} p_D \, dz' \right] dS_B \tag{A-3}$$

where S_B means all blade surfaces .

PRECEDING PAGE BLANK

Introducing the bound vorticity, γ , which is related to the blade loading by $\gamma = -\Delta p / \rho_\infty U_R$,

$$\phi = \int_{S_B} \gamma(r_o, z_o) \sqrt{1+\left(\frac{\omega r_o}{U}\right)^2} \left[\int_{-\infty}^{z} p_D\,(z', \zeta, r, z_o, r_o, \zeta_o)\, dz' \right] dS_B \tag{A-4}$$

The sign of the vorticity is defined opposite to that in the main body of the report to be consistent with Okurounmu and McCune. Now it can be shown that

$$\int_{-\infty}^{z} p_D\,(z', \zeta, r\,;\, z_o, r_o, \zeta_o)\, dz' = \int_{z_o}^{\infty} p\,(z, \zeta, r\,;\, z_o', \zeta_o, r_o)\, dz_o'$$

Also, the perturbation pressure and potential fields both must satisfy the same partial differential equation and boundary conditions (see Eqns. (55) and (56) of Ref. 1). Thus, it follows that the solution for a pressure dipole, p_D , is mathematically the same as that for a potential doublet, ϕ_D , although the two represent physically different flows. Analogous to the situation in wing theory (Ref. 16, Chapt. 5), we can then derive the potential due to an elementary horsehoe vortex as:

$$\phi_\gamma = \sqrt{1+\left(\frac{\omega r_o}{U}\right)^2} \int_{z_o}^{\infty} \phi_D\,(z, \zeta, r\,;\, z_o', \zeta_o, r_o)\, dz_o' \tag{A-5}$$

Then Eqn. (A-4) becomes

$$\phi = \int_{S_B} \gamma(r_o, z_o)\, \phi_\gamma\, dS_B \tag{A-6}$$

This equation expresses the potential due to a lifting rotor as the superposition of elementary horseshoe vortices. Each vortex has an infinitesimally long, radially oriented bound element located at z_o , r_o and a pair of trailing vortex filaments lying along the helical undisturbed streamlines.

In Ref. 5, Okurounmu and McCune developed the solution for equally spaced, radially oriented vortex lines (and their associated trailing vortex wakes) which span the annulus. To show that their solution is equivalent to that based on a dipole formulation, we proceed as follows. First, we substitute our pressure dipole solution, Eqn. (91) of Ref. 1, for q_D in Eqn. (A-5). The required integration has already been performed in Ref. 1, and is quoted there as Eqn. (100a). This elementary horseshoe vortex solution can then be used in (A-6) to construct the potential field due to B radially-oriented line vortices whose strength, Γ , varies with span:

$$q_r = \sum_{j=0}^{B-1} \int_{r_H}^{r_T} \Gamma(r_o)\, q_y\left(r, \zeta, z, r_o, \frac{2\pi j}{B}, z_o\right) d r_o \qquad \text{(A-7)}$$

Carrying out the required substitutions and the sum over j , we obtain:

$$\begin{aligned} q_r = {} & \frac{1}{2\pi\beta^2 r_T^2}\left(\frac{\omega B}{U}\right)\left(\frac{2}{1-h^2}\right)(z-z_o)\,H(z-z_o)\int_{r_H}^{r_T}\Gamma(r_o)\,r_o\,d r_o \\ & + \frac{B}{2\pi\beta^2 r_T^2}\sum_{\substack{m=-\infty \\ \neq 0}}^{\infty}\sum_{k=1}^{\infty} R_{mBk}(\sigma)\,e^{imB\zeta}\,\frac{imB\,H(z-z_o)}{\left[\frac{(mB)^2}{\beta^4}+\lambda_{mBk}^2\right]} \\ & \cdot \int_{r_H}^{r_T} R_{mBk}(\sigma_o)\,\Gamma(r_o)\left[\frac{1+\left(\frac{\omega r_o}{U}\right)^2}{\left(\frac{\omega r_o}{U}\right)^2}\right] r_o\,d r_o \\ & + \frac{B}{4\pi\beta^2 r_T^2}\sum_{m=-\infty}^{\infty}\sum_{k=1}^{\infty}\frac{R_{mBk}(\sigma)\,e^{imB\zeta}}{\left(\frac{\omega\lambda_{mBk}}{U}\right)\left[\frac{(mB)^2}{\beta^4}+\lambda_{mBk}^2\right]} \\ & \cdot \exp\left[\frac{imB}{\beta^2}\,\frac{\omega}{U}(z-z_o)-\frac{\omega\lambda_{mBk}}{U}|z-z_o|\right]\int_{r_H}^{r_T} R_{mBk}(\sigma_o)\,\Gamma(r_o) \\ & \cdot \left\{\frac{(mB)^2}{\beta^2\left(\frac{\omega r_o}{U}\right)}-\frac{\omega r_o}{U}\left[\frac{(mB)^2 M^2}{\beta^4}+\lambda_{mBk}^2\right]-\left[\frac{1+\left(\frac{\omega r_o}{U}\right)^2}{\frac{\omega r_o}{U}}\right] imB\,\lambda_{mBk}\right. \\ & \cdot \left.\left[2H(z-z_o)-1\right]\right\} d r_o \end{aligned} \qquad \text{(A-8)}$$

This solution will now be shown to be equivalent to that derived by Okurounmu and McCune[5] for the same problem, though they worked from a different point of view. When notational differences are accounted for the $m = o$ terms in the above expression are easily shown to be identical to those in Eqn. (8) of Ref. 5. However, the key step in demonstrating that the two solutions are equivalent is in showing that the terms representing the trailing vortex wakes are the same. These are the $m \neq 0$ terms in ϕ_r which appear in the second and third lines of Eqn. (A-8); they will be denoted by ϕ_w for convenience. Using Eqn. (2a), the wake potential ϕ_w may be written:

$$\phi_w = -\frac{B}{\pi r_T^2} \int_{r_H}^{r_T} \sum_{m=1}^{\infty} \sum_{k=1}^{\infty} R_{mBk}(\sigma) R_{mBk}(\sigma_o) \frac{\sin(mB\zeta)}{mB} \Gamma(r_o)$$

$$\cdot \left[\frac{\left(\frac{\omega r_T}{U}\right)^2}{\left(\frac{K_{mBk}}{mB}\right)^2 + \left(\frac{\omega r_T}{U}\right)^2} \right] \left[\frac{1 + \left(\frac{\omega r_o}{U}\right)^2}{\left(\frac{\omega r_o}{U}\right)^2} \right] r_o \, d r_o \qquad \text{(A-9)}$$

We now employ the addition and subtraction manipulation used in Section IV-C of Ref. 1 to demonstrate that the expressions for the velocity components contained the correct discontinuities. Then ϕ_w becomes

$$\phi_w = -\frac{B}{\pi r_T^2} \sum_{m=1}^{\infty} \sum_{k=1}^{\infty} \frac{\sin(mB\zeta)}{mB} R_{mBk}(\sigma) \int_{r_H}^{r_T} \Gamma(r_o) R_{mBk}(\sigma_o) \, r_o \, d r_o$$

$$- \frac{B}{\pi r_T^2} \int_{r_H}^{r_T} \sum_{m=1}^{\infty} \frac{\sin(mB\zeta)}{mB} \sum_{k=1}^{\infty} R_{mBk}(\sigma_o) R_{mBk}(\sigma)$$

$$\cdot \frac{\Gamma(r_o)\left[r_T^2 - r_o^2 \left(\frac{K_{mBk}}{mB}\right)^2\right]}{r_o \left[\left(\frac{K_{mBk}}{mB}\right)^2 + \left(\frac{\omega r_T}{U}\right)^2\right]} \, d r_o \qquad \text{(A-10)}$$

The sum over k in the first line is the Fourier-Bessel expansion for $\Gamma(r)$; the sum over m yields the sawtooth function ζ_j defined by:

$$\zeta_j = -2\sum_{m=1}^{\infty} \frac{\sin(mB\zeta)}{mB} \qquad \text{(A-11)}$$

$$= \zeta - \frac{(2j+1)\pi}{B} \qquad \frac{2\pi j}{B} \le \zeta \le \frac{2\pi}{B}(j+1) \qquad j = 0, 1, \ldots, B-1$$

Note that ζ_j has a discontinuity of $\left(-\frac{2\pi}{B}\right)$ as one crosses a blade surface, $\zeta = \frac{2\pi j}{B}$, in the positive ζ direction. By substituting from Bessel's equation, the second line of (A-10) can be written in terms of derivatives of the series $S_n(r, r_o)$ defined by:

$$S_n(r, r_o) = \sum_{k=1}^{\infty} \frac{R_{nk}(K_{nk}\sigma)\, R_{nk}(K_{nk}\sigma_o)}{\left[\left(\frac{K_{nk}}{r_T}\right)^2 + \left(\frac{\omega n}{U}\right)^2\right]} \qquad \text{(A-12)}$$

The wake potential then reads

$$\phi_\omega = \frac{B}{2\pi}\Gamma(r)\zeta_j - \frac{B}{\pi r_T^2}\sum_{m=1}^{\infty}\frac{\sin(mB\zeta)}{mB}\int_{r_H}^{r_T}\Gamma(r_o)\frac{d}{dr_o}\left(r_o\frac{dS_{mB}}{dr_o}\right)dr_o \qquad \text{(A-13)}$$

The series defined in (A-12) has been summed by Salaun[13] in terms of modified Bessel functions using the following technique. If we differentiate the series twice with respect to σ , and use the Fourier-Bessel expansion for $\delta(\sigma-\sigma_o)$,

$$\frac{\delta(\sigma-\sigma_o)}{\sigma_o} = \sum_{k=1}^{\infty} R_{nk}(\sigma)\, R_{nk}(\sigma_o) \qquad n \neq 0 \qquad \text{(A-14)}$$

then the following differential equation is obtained for S_n :

$$\frac{1}{\sigma_n}\frac{d}{d\sigma_n}\left(\sigma_n \frac{dS_n}{d\sigma_n}\right) - \left[\left(\frac{n}{\sigma_n}\right)^2 + 1\right] S_n = -r_T^2 \frac{\delta(\sigma_n - \sigma_{n_o})}{\sigma_n} \qquad \text{(A-15)}$$

where the notation $\sigma_n = n\omega r/U$ has been introduced. (Note that the addition and subtraction manipulation used in Section IV-C of Ref. 1 is equivalent to substituting for S_n from Eqn. (A-15)). This equation is solved subject to the hard-wall boundary conditions, i.e. that $dS_n/d\sigma_n$ vanish at the inner and outer duct walls $\sigma_n = \sigma_{n_H} = n\omega r_H/U$ and $\sigma_{n_T} = n\omega r_T/U$. Moreover, S_n is required to be continuous at $\sigma_n = \sigma_{n_o}$ and $dS_n/d\sigma_n$ must satisfy the following jump condition there:

$$\left[\left(\frac{dS_n}{d\sigma_n}\right)_{\sigma_{n_o}^+} - \left(\frac{dS_n}{d\sigma_n}\right)_{\sigma_{n_o}^-}\right] = -\frac{r_T^2}{\sigma_{n_o}} \qquad \text{(A-16)}$$

This was derived by integrating Eqn. (A-15) from $\sigma_{n_o} - \varepsilon$ to $\sigma_{n_o} + \varepsilon$.

The modified Bessel functions $I_n(\sigma_n)$ and $K_n(\sigma_n)$ are linearly independent solutions of the homogeneous equation for S_n . For $\sigma_n < \sigma_{n_o}$ assume

$$S_n(\sigma_n, \sigma_{n_o}) = C_1(\sigma_{n_o}) I_n(\sigma_n) + C_2(\sigma_{n_o}) K_n(\sigma_n) \qquad \text{(A-17a)}$$

while for $\sigma_n > \sigma_{n_o}$ set

$$S_n(\sigma_n, \sigma_{n_o}) = C_3(\sigma_{n_o}) I_n(\sigma_n) + C_4(\sigma_{n_o}) K_n(\sigma_n) \qquad \text{(A-17b)}$$

The coefficients C_1 thru C_4 are chosen so as to satisfy the boundary conditions cited above, and the results are:

$$C_1 = \frac{-r_T^2 K_n'(\sigma_{n_H})}{Z} \left[K_n'(\sigma_{n_T}) I_n(\sigma_{n_o}) - I_n'(\sigma_{n_T}) K_n(\sigma_{n_o})\right]$$

$$C_2 = \frac{r_T^2 I_n'(\sigma_{n_H})}{Z} \left[K_n'(\sigma_{n_T}) I_n(\sigma_{n_o}) - I_n'(\sigma_{n_T}) K_n(\sigma_{n_o})\right]$$

$$C_3 = \frac{-r_T^2 K_n'(\sigma_{n_T})}{Z} \left[K_n'(\sigma_{n_H}) I_n(\sigma_{n_o}) - I_n'(\sigma_{n_H}) K_n(\sigma_{n_o})\right]$$

$$C_4 = \frac{r_T^2 I_n'(\sigma_{n_T})}{Z} \left[K_n'(\sigma_{n_H}) I_n(\sigma_{n_o}) - I_n'(\sigma_{n_H}) K_n(\sigma_{n_o})\right]$$

where

$$Z \equiv I_n'(\sigma_{n_T}) K_n'(\sigma_{n_H}) - I_n'(\sigma_{n_H}) K_n'(\sigma_{n_T}) \qquad \text{(A-18)}$$

and primes denote differentiation with respect to the argument.

Returning to Eqn. (A-13), if we integrate by parts once in the second term, make use of the fact that $d S_{mB}/d r_o$ vanishes at the hub and tip, and then substitute for S_{mB} from the results given in (A-17) and (A-18), we obtain for the wake potential:

$$\varphi_\omega = \frac{B}{2\pi} \Gamma(r) \zeta_j + \frac{B}{\pi r_T^2} \sum_{m=1}^{\infty} \frac{\sin(mB\zeta)}{mB}$$

$$\cdot \left\{ C_1(\sigma_{mB}) \int_{\sigma_{mB_H}}^{\sigma_{mB}} \sigma_{mB_o} \frac{d\Gamma}{d\sigma_{mB_o}} I'_{mB}(\sigma_{mB_o}) d\sigma_{mB_o} \right.$$

$$+ C_2(\sigma_{mB}) \int_{\sigma_{mB_H}}^{\sigma_{mB}} \sigma_{mB_o} \frac{d\Gamma}{d\sigma_{mB_o}} K'_{mB}(\sigma_{mB_o}) d\sigma_{mB_o}$$

$$+ C_3(\sigma_{mB}) \int_{\sigma_{mB}}^{\sigma_{mB_T}} \sigma_{mB_o} \frac{d\Gamma}{d\sigma_{mB_o}} I'_{mB}(\sigma_{mB_o}) d\sigma_{mB_o}$$

$$\left. + C_4(\sigma_{mB}) \int_{\sigma_{mB}}^{\sigma_{mB_T}} \sigma_{mB_o} \frac{d\Gamma}{d\sigma_{mB_o}} K'_{mB}(\sigma_{mB_o}) d\sigma_{mB_o} \right\} \qquad \text{(A-19)}$$

After reorganizing the ranges of the integrals above, the expression in braces can be shown to be $-r_T^2 \chi_{mB}$, where χ_{mB} is the wake function defined in Eqn. (5) of Ref. 5. (Okurounmu and McCune placed their blades at $\zeta = \frac{(2j+1)\pi}{B}$ rather than $\frac{2\pi j}{B}$, which results in an extra factor of $(-1)^m$ in their result.) The above representation for the wake potential is thus equivalent to that given by Okurounmu and McCune[5] in Eqn. (4).

It remains to be shown that the last four lines in Eqn. (A-8), which contain the exponential factors in $(z - z_o)$, are the same as the corresponding ones in the line vortex solution of Okurounmu and McCune. The equivalence of the $m=0$ terms is straightforward, as noted earlier. For $m \neq 0$, the factors in the braces in Eqn. (A-8) are first rearranged, using the same addition and subtraction manipulation referred to above. Then, the following two radial integrals which arise,

$$\int_h^1 \Gamma(\sigma_o) R_{mBk}(\sigma_o) \sigma_o \, d\sigma_o$$

$$\int_h^1 \frac{\Gamma(r_o)\left[r_T^2 - r_o^2 \left(\frac{K_{mBk}}{mB}\right)^2\right]}{r_o^2\left[\left(\frac{K_{mBk}}{mB}\right)^2 + \left(\frac{\omega r_T}{U}\right)^2\right]} R_{mBk}(\sigma_o) \sigma_o \, d\sigma_o$$

can be identified as the coefficients of $R_{mBk}(\sigma)$ in the Fourier-Bessel expansions of the bound vorticity, $\Gamma(\sigma)$, and the wake functions, χ_{mB}, respectively. The latter follows from the above demonstration that the k series in the second term of Eqn. (A-10) is indeed proportional to χ_{mB} . Okurounmu and McCune refer to the coefficients defined by the above integrals as Γ_{mBk} and h_{mBk} , respectively. Once these identifications are made, the equivalence between these terms and their counterparts in Eqn. (8) of Ref. 5 is evident.

Thus, we have been able to show that the singularity solutions used to represent a lifting rotor in the present work can be put in the same form as those used by Okurounmu and McCune[5]. On this basis, we have concluded that the lifting-surface formulations based on the pressure dipole and vortex representations, though in markedly different forms, are indeed equivalent.

Appendix B
EVALUATION OF RADIAL INTEGRALS

This appendix presents the analytical evaluation of the set of radial integrals defined by:

$$I^{j}_{nk} = \int_{h}^{1} \sigma^{j} R_{nk}(K_{nk}\sigma)\, d\sigma \tag{B-1}$$

where j, k and $n = m\beta$ are all integers. The R_{nk} are linear combinations of the J_n and Y_n Bessel functions:

$$R_{nk}(K_{nk}\sigma) = \frac{J_n(K_{nk}\sigma) - \delta_{nk} Y_n(K_{nk}\sigma)}{N_{nk}} \tag{B-2}$$

where δ_{nk} and N_{nk} are phase and normalization factors, respectively, which vary from mode to mode, but are independent of σ. These functions are discussed at length in Refs. 2-4, and 15. The procedure used in evaluating the eigenvalues and eigenfunctions for large values of n is described in Ref. 22.

The above integral can be evaluated by using the following indefinite integral given by Watson:[23]

$$\int \xi^{j} Z_n(\xi)\, d\xi = (j+n-1) \int \xi^{j-1} Z_n(\xi)\, S_{j-1,n-1}(\xi) - \xi^{j} Z_{n-1}(\xi)\, S_{j,n}(\xi) \tag{B-3}$$

where Z_n represents either J_n or Y_n and the $S_{j,n}$ are Lommel's functions. Substitution of Eqns. (B-2) and (B-3) into (B-1) yields:

$$I^{j}_{nk} = \left[\frac{\sigma}{K_{nk}} \left\{ (j+n-1) R_{nk}(K_{nk}\sigma)\, S_{j-1,n-1}(K_{nk}\sigma) - \frac{[J_{n-1}(K_{nk}\sigma) - \delta_{nk} Y_{n-1}(K_{nk}\sigma)]}{N_{nk}}\, S_{j,n}(K_{nk}\sigma) \right\} \right]_{h}^{1}$$

This can be simplified by making use of the Bessel function recursion relation,

$$\Xi_{n-1}(\xi) = \Xi_n'(\xi) + \frac{n}{\xi}\Xi_n(\xi)$$

where a prime indicates differentiation with respect to the argument. Also, by definition:

$$\frac{\partial}{\partial\sigma} R_{nk}(K_{nk}\sigma) = 0 \qquad \sigma = h, 1$$

This gives

$$I_{nk}^{j} = \left[\frac{\sigma R_{nk}(K_{nk}\sigma)}{K_{nk}^{j}}\left\{(j+n-1)S_{j-1,n-1}(K_{nk}\sigma) - \frac{n}{K_{nk}\sigma}S_{jn}(K_{nk}\sigma)\right\}\right]_{h} \quad \text{(B-4)}$$

Watson[23] also gives the following recursion formula satisfied by Lommel's function:

$$S_{j,n}'(\xi) = (j+n-1)S_{j-1,n-1}(\xi) - \frac{n}{\xi}S_{j,n}(\xi)$$

which allows Eqn. (B-4) to be put in its simplest form:

$$I_{nk}^{j} = \left[\frac{\sigma R_{nk}(K_{nk}\sigma)\, S_{j,n}'(K_{nk}\sigma)}{K_{nk}^{j}}\right]_{h}^{1} \quad \text{(B-5)}$$

Since R_{nk} at the hub and tip will have already been evaluated as part of determining K_{nk}, the only new quantities introduced above are the Lommel functions. They may be easily evaluated using the formulae cited by Watson;[23] since these are all given for $S_{j,n}$ rather than its derivative, in practice Eqn. (B-4) was used rather than (B-5). The calculated values were checked by recognizing that I_{nk}^{j} as defined in Eqn. (B-1) is just the k th coefficient in the Fourier-Bessel expansion of σ^{j-1}, i.e.

$$\sigma^{j-1} = \sum_{k=1}^{\infty} I_{nk}^{j} R_{nk}(K_{nk}\sigma) \quad \text{(B-6)}$$

Satisfaction of Eqn. (B-6) was verified for several values of j, n and σ.

Appendix C
EVALUATION OF AXIAL INTEGRALS

This appendix presents the analytical evaluation of the axial integrals defined by Eqn. (14). $C^i(x)$ is easily evaluated after making the substitution

$$x_o = \cos\phi_o \qquad x = \cos\phi \tag{C-1}$$

The results are:

$$C^i(x) = \begin{cases} \pi - \phi + \sin\phi & i = 1 \\ (\pi - \phi)/2 + \sin 2\phi/4 & i = 2 \\ \sin i\phi/2i - \sin(i-2)\phi/2(i-2) & i > 2 \end{cases} \tag{C-2}$$

The derivation of the results for C^i_{mBk} and S^i_{mBk} is rather lengthy, although the procedure is straightforward once a few key relations are given. Only an outline of the principal steps is given below, followed by the final results:

1) The cosines and sines appearing in the integrands of Eqn. (14) are written as either the real or imaginary parts of complex exponentials, and the region of integration is split in two, according to whether x_o is greater or less than x.

2) Use is made again of the substitution in Eqn. (C-1); this reduces the integrands to trigonometric forms involving only sines and cosines of multiples of ϕ_o. For $i > 1$, set

$$\sin\phi_o \sin(i-1)\phi_o = \frac{1}{2}[\cos(i-2)\phi_o - \cos i\phi_o]$$

3) Each integrand will contain an exponential of the form $e^{z\cos\phi_o}$ where z is in general complex. It takes on the values $z = \pm a - ib$ where

$$a = \begin{cases} \eta_T K_{0K}/\beta & m = 0 \\ m\beta\eta_T \beta_{m\beta K}/\beta & m > 0 \end{cases} \qquad \text{(C-3a)}$$

$$b = \begin{cases} 0 & m = 0 \\ m\beta\phi_T \eta_T/\beta^2 & m > 0 \end{cases} \qquad \text{(C-3b)}$$

The exponential is expanded in a simple cosine series using Eqn. (9.6.34) of Ref. 24:

$$e^{z\cos\phi_0} = I_0(z) + 2\sum_{n=1}^{\infty} I_n(z)\cos n\phi_0 \qquad \text{(C-4)}$$

Here $I_n(z)$ is the modified Bessel function of the first kind of integer order n. Noting that $|I_n(z)| = |J_n(z)|$, where $J_n(z)$ is the regular Bessel function, and that $J_n(z)$ decays exponentially with n once $n \gtrsim |z|$ (see, e.g., Michels,[25]) the series in Eqn. (C-4) can be expected to converge rapidly once n exceeds this value.

4) The integrand will now contain a series of terms, each of which involves at worst the product of two cosines. Since we know the series converge as discussed in 3), the integration over ϕ_0 may be carried out term-by-term.

5) The series of integrated terms which result from 4) will have different arguments for I_n, depending on whether the series arose from the integral for x_0 greater or less than x. However, the two are related through

$$I_n[-a - ib] = (-1)^n I_n^*(a - ib) \qquad \text{(C-5)}$$

where the asterisk denotes the complex conjugate. This allows most of the terms in the series arising from the two integrals to be combined in a single series, considerably simplifying the results.

The final results are given below, where the symbols $\mathcal{R}e$ and $\mathcal{I}m$ denote real and imaginary parts, respectively:

$i = 1$

$$C'_{mBk}(z) = \pi e^{-ax}\left[\cos bx\,(\mathcal{R}e\,I_0 - \mathcal{R}e\,I_1) - \sin bx\,(\mathcal{I}m\,I_0 - \mathcal{I}m\,I_1)\right]$$

$$+ 2(\sin\phi - \phi)(\cosh ax\cos bx\,\mathcal{R}e\,I_0 + \sinh ax\sin bx\,\mathcal{I}m\,I_0)$$

$$+ 4\sum_{n=1}^{\infty}(-1)^n\left[\frac{\sin(n-1)\phi}{2(n-1)} - \frac{\sin n\phi}{n} + \frac{\sin(n+1)\phi}{2(n+1)}\right]$$

$$\cdot\left[\begin{Bmatrix}\cosh ax\\ \sinh ax\end{Bmatrix}\cos bx\,\mathcal{R}e\,I_n + \begin{Bmatrix}\sinh ax\\ \cosh ax\end{Bmatrix}\sin bx\,\mathcal{I}m\,I_n\right]\begin{Bmatrix}n\ \text{EVEN}\\ n\ \text{ODD}\end{Bmatrix} \qquad \text{(C-6a)}$$

$$S'_{mBk}(x) = \pi e^{-ax}\left[\cos bx\,(\mathcal{I}m\,I_0 - \mathcal{I}m\,I_1) + \sin bx\,(\mathcal{R}e\,I_0 - \mathcal{R}e\,I_1)\right]$$

$$+ 2(\sin\phi - \phi)(\cosh ax\cos bx\,\mathcal{I}m\,I_0 - \sinh ax\sin bx\,\mathcal{R}e\,I_0)$$

$$+ 4\sum_{n=1}^{\infty}(-1)^n\left[\frac{\sin(n-1)\phi}{2(n-1)} - \frac{\sin n\phi}{n} + \frac{\sin(n+1)\phi}{2(n+1)}\right]$$

$$\cdot\left[\begin{Bmatrix}\cosh ax\\ \sinh ax\end{Bmatrix}\cos bx\,\mathcal{I}m\,I_n - \begin{Bmatrix}\sinh ax\\ \cosh ax\end{Bmatrix}\sin bx\,\mathcal{R}e\,I_n\right]\begin{Bmatrix}n\ \text{EVEN}\\ n\ \text{ODD}\end{Bmatrix} \qquad \text{(C-6b)}$$

$i \geq 2$

$$C^i_{mBk}(x) = \frac{\pi}{2}e^{-ax}\left[\delta_{i,2}\,T_0 + (1-\delta_{i,2})\,T_{i-2} - T_i\right]$$

$$+ \left[\frac{\sin i\phi}{i} - \frac{\sin(i-2)\phi}{(i-2)}\right]\left[\cosh ax\cos bx\,\mathcal{R}e\,I_0 + \sinh ax\sin bx\,\mathcal{I}m\,I_0\right]$$

$$+ \sum_{n=1}^{\infty}(-1)^n\left[\frac{\sin(n-i)\phi}{(n-i)} + \frac{\sin(n+i)\phi}{(n+i)} - \frac{\sin(n-i+2)\phi}{(n-i+2)} - \frac{\sin(n+i-2)\phi}{(n+i-2)}\right]$$

$$\cdot\left[\begin{Bmatrix}\cosh ax\\ \sinh ax\end{Bmatrix}\cos bx\,\mathcal{R}e\,I_n + \begin{Bmatrix}\sinh ax\\ \cosh ax\end{Bmatrix}\sin bx\,\mathcal{I}m\,I_n\right]\begin{Bmatrix}n\ \text{EVEN}\\ n\ \text{ODD}\end{Bmatrix} \qquad \text{(C-6c)}$$

AD-A077 712 CALSPAN ADVANCED TECHNOLOGY CENTER BUFFALO NY AERODYN--ETC F/G 21/5
AERODYNAMIC AND ACOUSTIC INVESTIGATIONS OF AXIAL FLOW FAN AND C--ETC(U)
AUG 79 G F HOMICZ , J A LORDI , G R LUDWIG F33615-76-C-2092
UNCLASSIFIED CALSPAN-XE-5933-A-103 AFAPL-TR-79-2061 NL

2 OF 2
AD
A077712

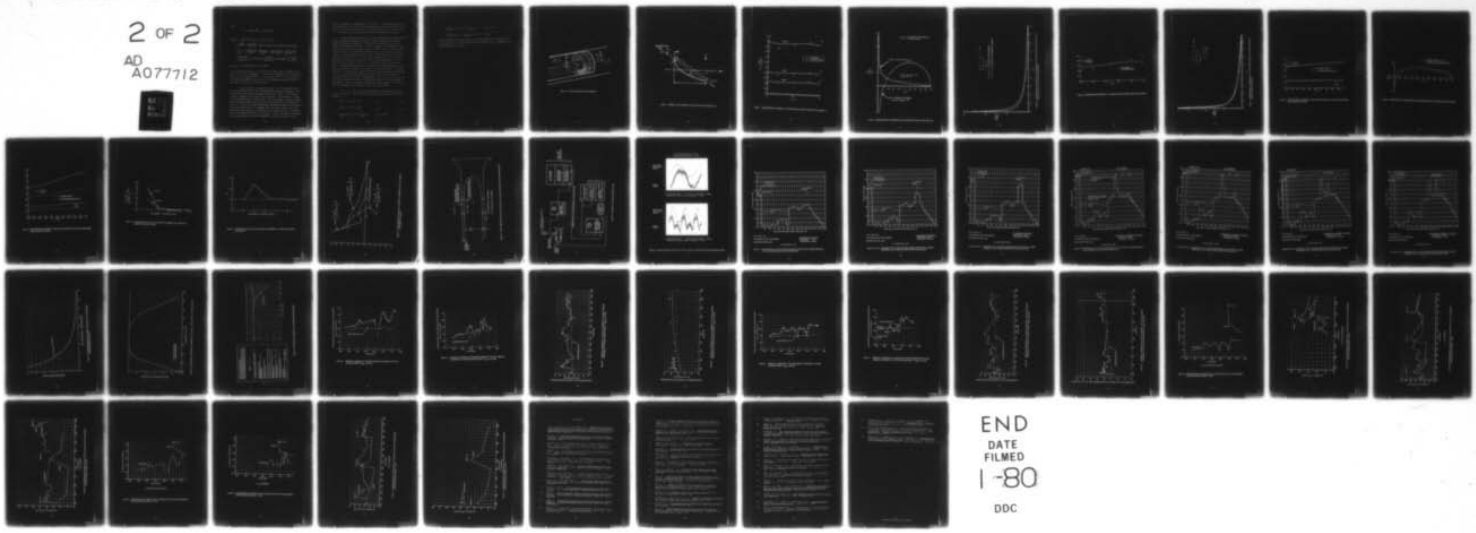

END
DATE
FILMED
1-80
DDC

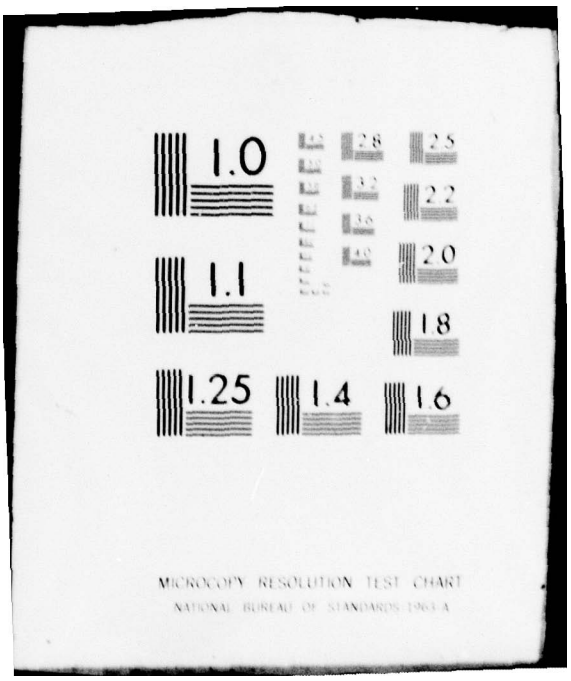
1.0
1.1
1.25
1.4
1.6
2.8
3.2
3.6
4.0
2.5
2.2
2.0
1.8
MICROCOPY RESOLUTION TEST CHART
NATIONAL BUREAU OF STANDARDS 1963-A

where

$$T_n = \cos bx \; Re\, I_n - \sin bx \; Im\, I_n$$

$$S^{i}_{m3k}(x) = \frac{\pi}{2} e^{-ax} \left[\delta_{i,2} T_0 + (1 - \delta_{i,2}) T_{i-2} - T_i \right]$$

$$+ \left[\frac{\sin i\phi}{i} - \frac{\sin (i-2)\phi}{(i-2)} \right] \left[\cosh ax \cos bx \; Im\, I_0 - \sinh ax \sin bx \; Re\, I_0 \right]$$

$$+ \sum_{n=1}^{\infty} (-1)^n \left[\frac{\sin (n-i)\phi}{(n-i)} + \frac{\sin (n+i)\phi}{(n+i)} - \frac{\sin (n-i+2)\phi}{(n-i+2)} - \frac{\sin (n+i-2)\phi}{(n+i-2)} \right]$$

$$\cdot \left[\begin{Bmatrix} \cosh ax \\ \sinh ax \end{Bmatrix} \cos bx \; Im\, I_n - \begin{Bmatrix} \sinh ax \\ \cosh ax \end{Bmatrix} \sin bx \; Re\, I_n \right] \begin{Bmatrix} n \text{ EVEN} \\ n \text{ ODD} \end{Bmatrix} \qquad \text{(C-6d)}$$

where now $T_n = \cos bx \; Im\, I_n + \sin bx \; Re\, I_n$.

In the above expressions $\delta_{i,j}$ is the Kronecker delta symbol, defined as one when $i = j$, and zero otherwise. It must also be remembered in evaluating the sums over n that $\lim_{n \to 0} \frac{\sin n\phi}{n} = \phi$. The special case $m = 0$ can be obtained from the above results by setting $b = 0$ and recognizing that this implies the Bessel functions will be purely real.

At first glance, the evaluation of Eqn. (C-6) might appear even more time-consuming than a more straightforward numerical integration. But, in addition to the obvious advantage that they are "exact" to any desired accuracy, depending on how many terms one retains in the sum over n, there is one overriding point in their favor. That is, whereas a numerical integration scheme must repeat every step of the calculation for all combinations of m, k, i and l, the above expressions conveniently separate the influence of each of these indices. For example, once the x_l are chosen, the values of ϕ and all the sines can be determined; also, functions such as $\cosh ax$ need to be computed only NM x NK x NL times. Finally, note that the argument of the complex Bessel function I_n depends only on the two indices m and k.

Since this argument is independent of the order, n, of the Bessel functions, one can make use of a very efficient algorithm based on the recursion relation (Ref. 26) to calculate all orders of the function at once, for a given m and k. This part of the calculation need only be performed NM x NK times.

Results computed from Eqn. (C-6) were compared against those obtained using the numerical integration scheme of O'Hara and Smith[27] for several hundred representative integrals. The analytical evaluation proved much faster, and agreement within the 1% accuracy required of the quadrature calculation was exhibited in the great majority of cases. However, for the higher values of m and k, the analytical evaluation gave results which were grossly in error. This was traced to the fact that for large values of a and $\cos\phi_o$ negative, the left side of Eqn. (C-4) decays exponentially with a, while each term in the series on the right side is growing exponentially.[24] This leads to similar behavior in Eqn. (C-6), resulting in excessive round-off error. The calculations were done on an IBM 360/65 in double precision arithmetic, which can be expected to yield about 16 significant digits. For these conditions it was found that round-off error became a significant problem when $a \geq 11$, in which case the program automatically reverts to the numerical integration method cited above. Unfortunately, when a is large b is also, and the resulting highly oscillatory integrand again leads to a time-consuming calculation. Clearly an asymptotic evaluation of the integrals in this limit would be preferable; work along these lines has been initiated.

For $i \geq 2$, there is yet a further means of streamlining the axial integral evaluations. This is based on the following easily proven symmetry properties:

$$C^2(-x) = \pi/2 - C^2(x) \qquad i = 2 \qquad \text{(C-7a)}$$

$$C^i(-x) = (-1)^{i+1} C^i(x) \qquad i > 2 \qquad \text{(C-7b)}$$

$$C^i_{mBk}(-x) = (-1)^{i+1} C^i_{mBk}(x) \qquad i \geq 2,\ m \geq 0 \qquad \text{(C-7c)}$$

$$S^{i}_{m\beta k}(-x) = (-1)^{i+1} S^{i}_{m\beta k}(x) \qquad i \geq 2,\ m \geq 1 \tag{C-7d}$$

$$C^{i}_{m\beta k}(x=0) = S^{i}_{m\beta k}(x=0) = 0 \qquad i \text{ even} \tag{C-7e}$$

If the chordwise collocation points, x_ℓ, are symmetrically disposed about the mid-chord, $x = 0$, then use of the above relations can cut computing time and storage almost in half.

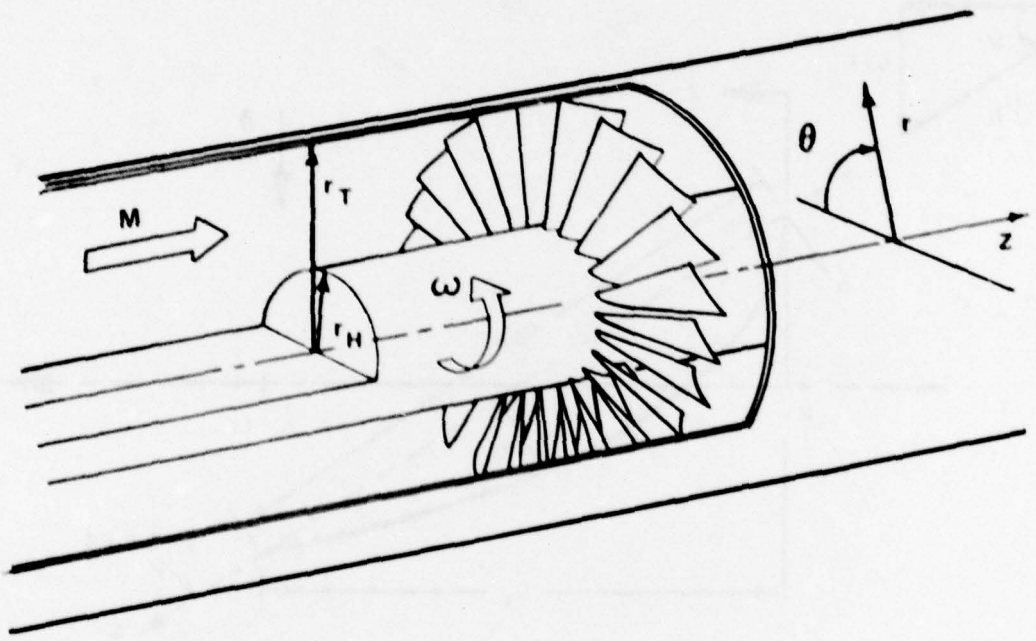

Figure 1 BLADE ROW AND DUCT GEOMETRY

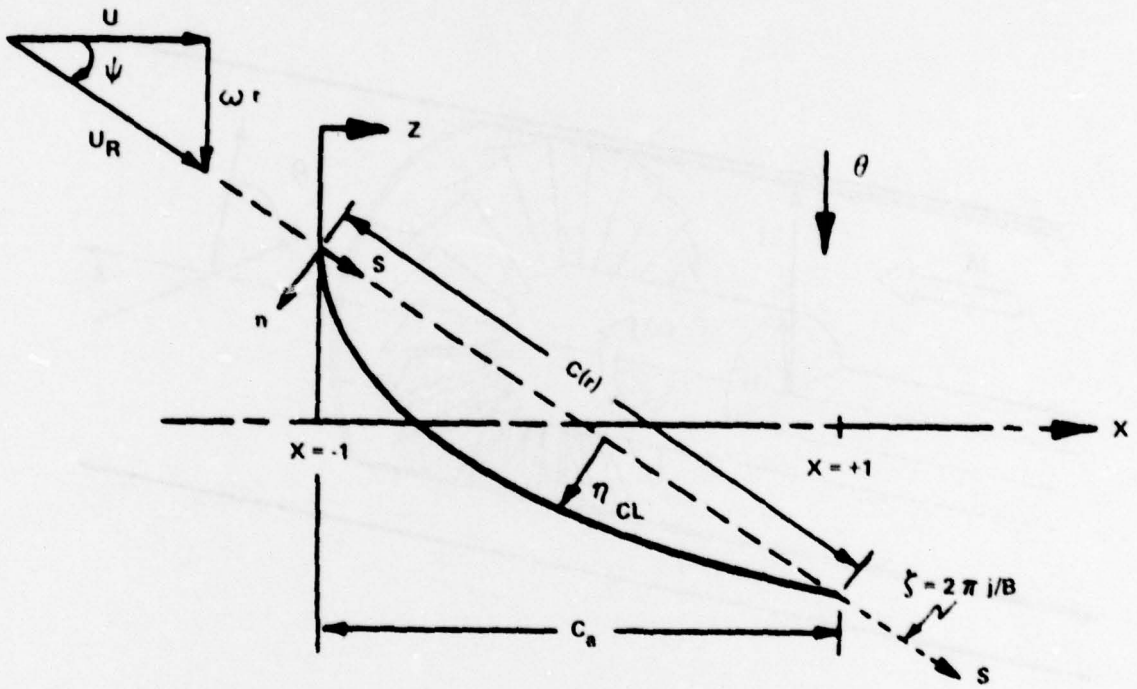

Figure 2 CAMBER LINE GEOMETRY IN BLADE-FIXED COORDINATES

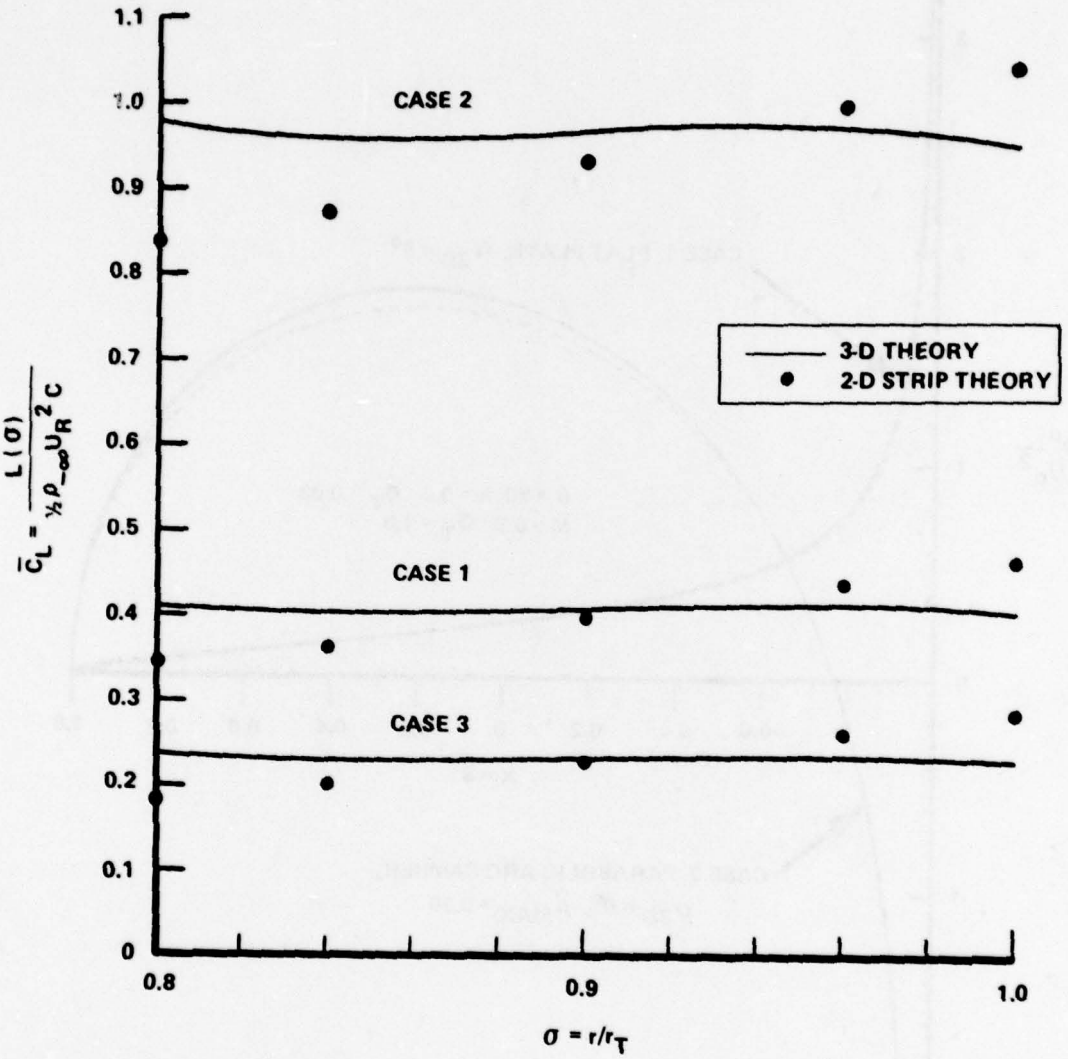

Figure 3 COMPARISON OF PRESENT 3-D THEORY AND 2-D STRIP THEORY FOR CASES 1-3

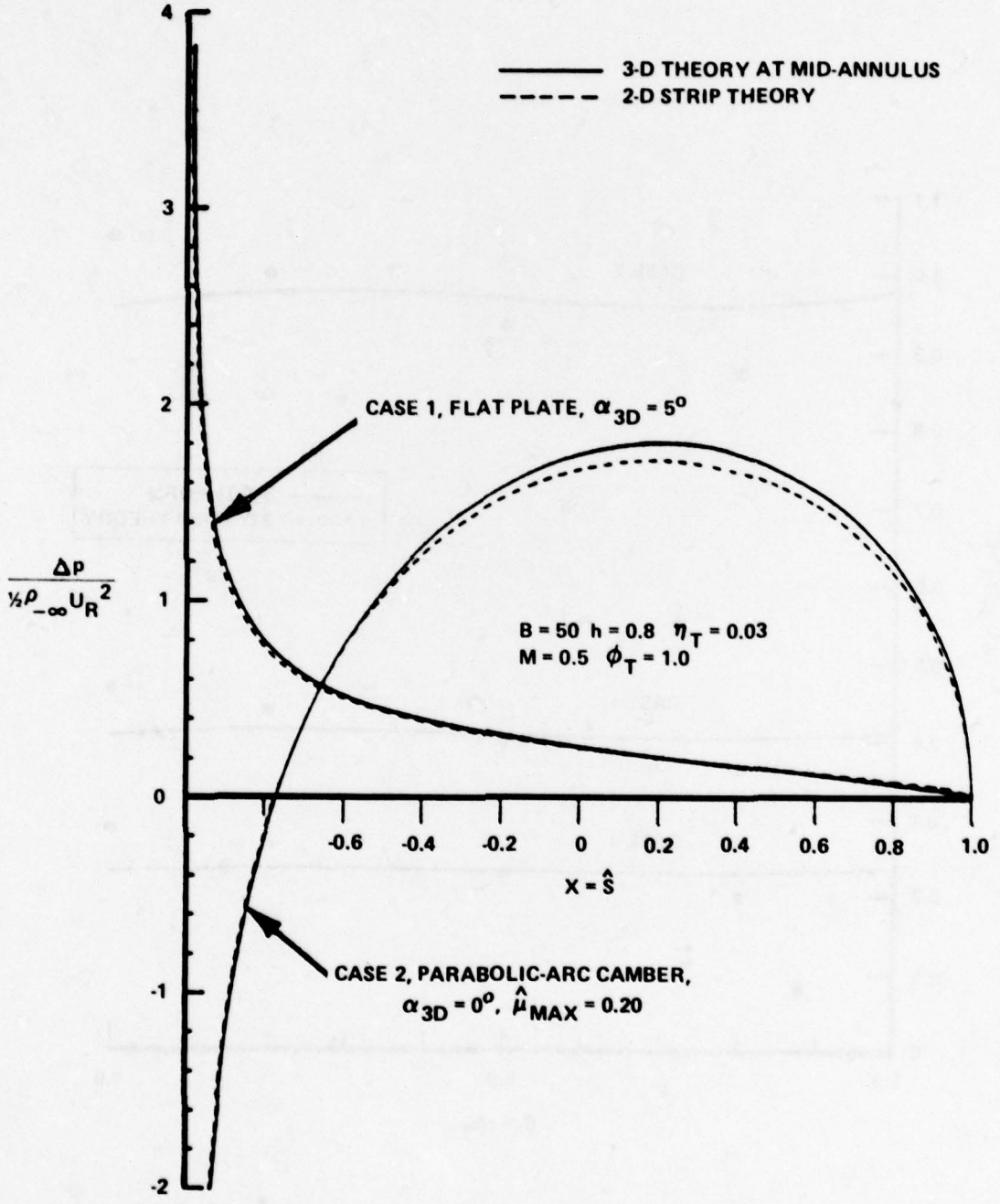

Figure 4 COMPARISON OF CHORDWISE LOAD DISTRIBUTIONS AT MID-ANNULUS

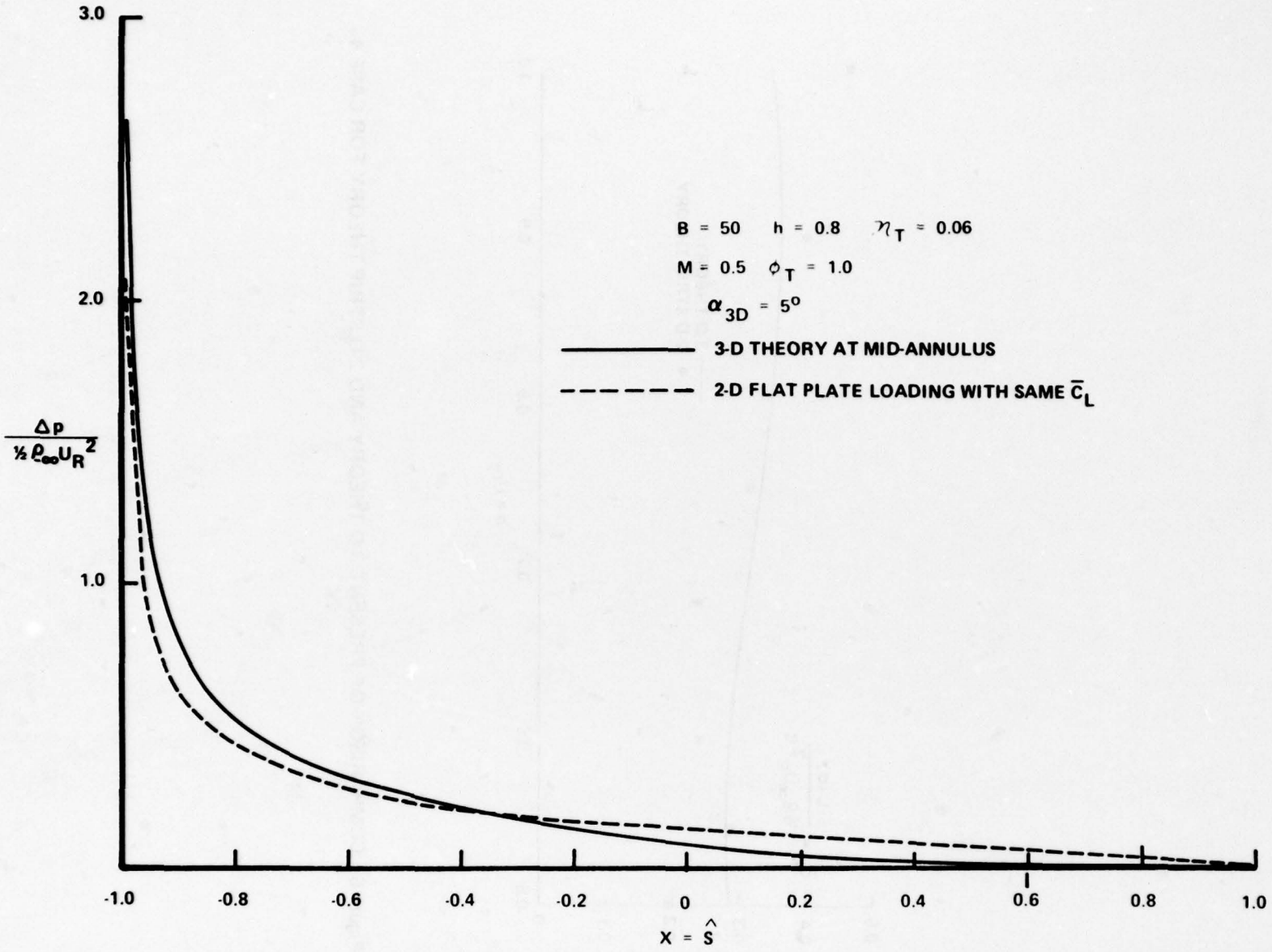

Figure 5 COMPARISON OF CHORDWISE LOAD DISTRIBUTION AT MID-ANNULUS FOR CASE 3 WITH ISOLATED FLAT PLATE DISTRIBUTION

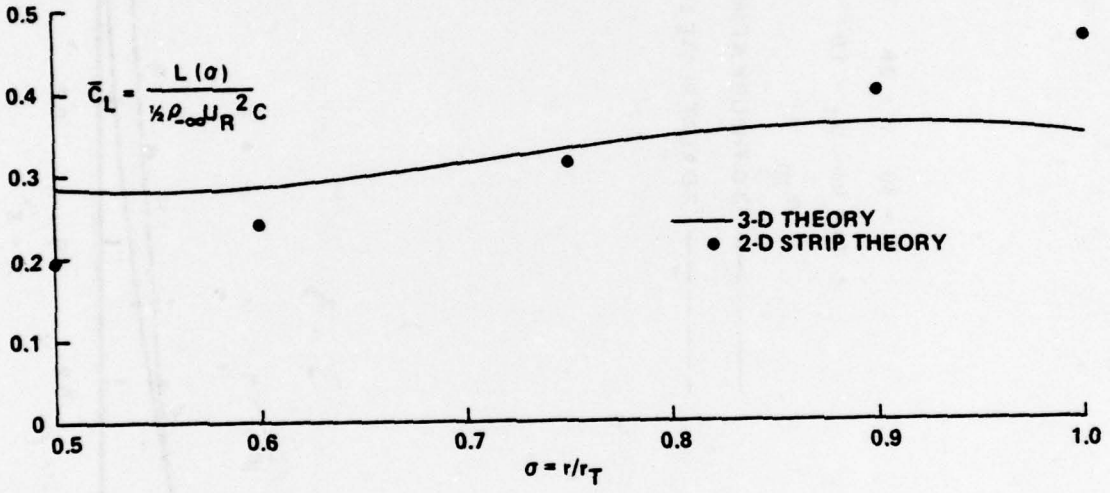

Figure 6 COMPARISON OF PRESENT 3-D THEORY AND 2-D STRIP THEORY FOR CASE 4

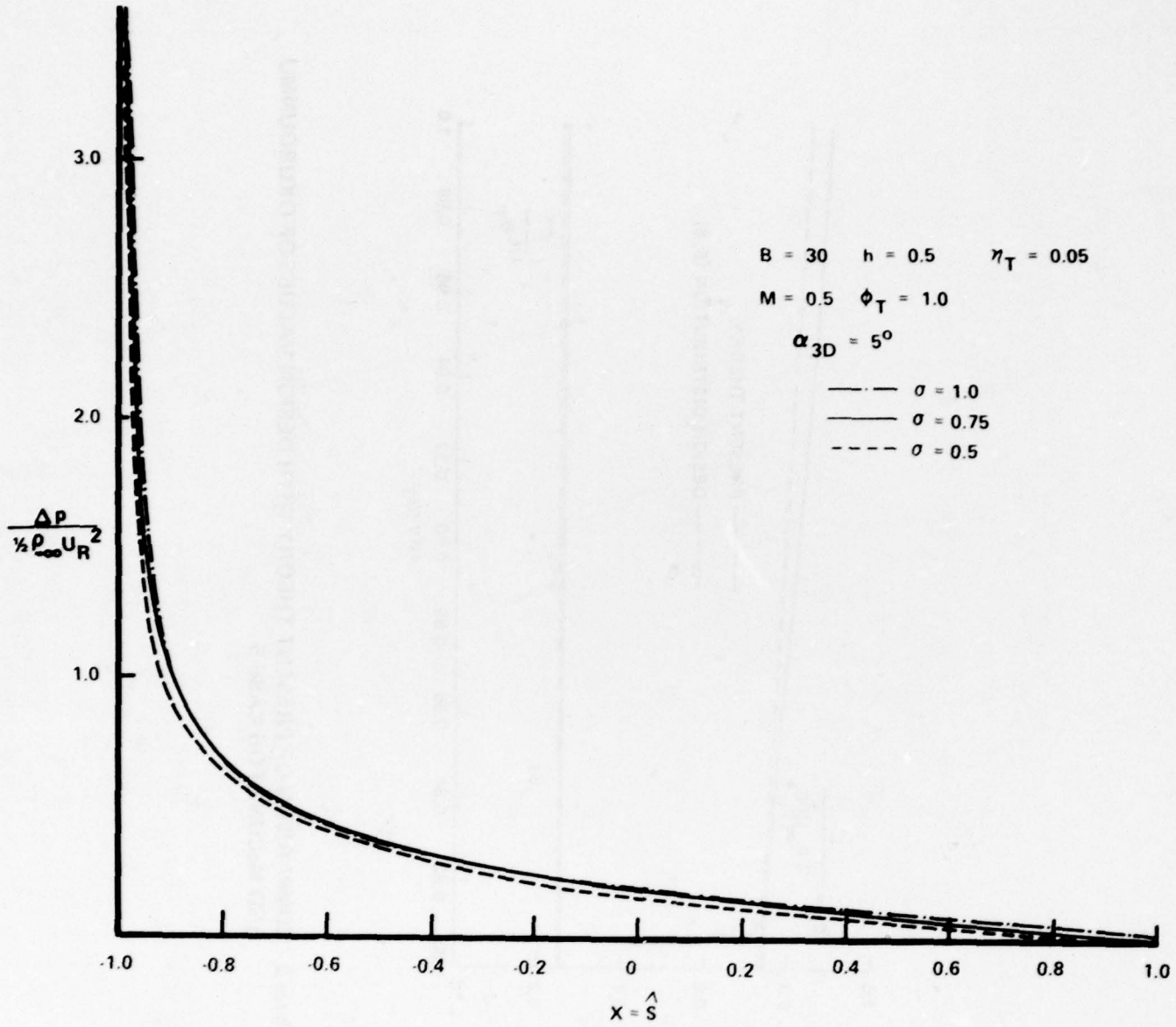

Figure 7 COMPARISON OF CHORDWISE LOAD DISTRIBUTIONS AT HUB, MID-ANNULUS, AND TIP RADII FOR CASE 4

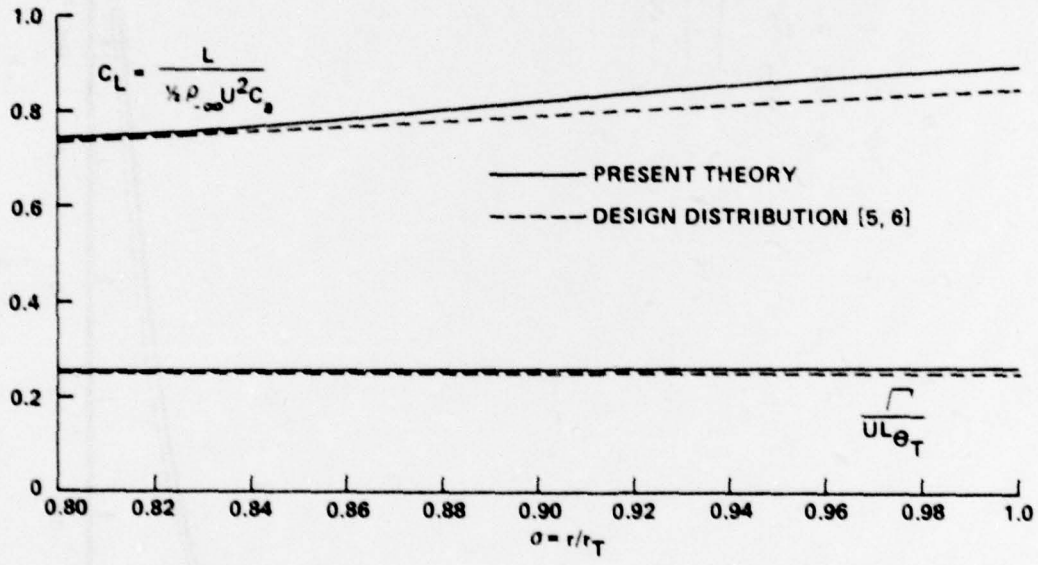

Figure 8 COMPARISON OF PRESENT THEORY WITH DESIGN VALUES OF OKUROUNMU AND McCUNE FOR CASE 5

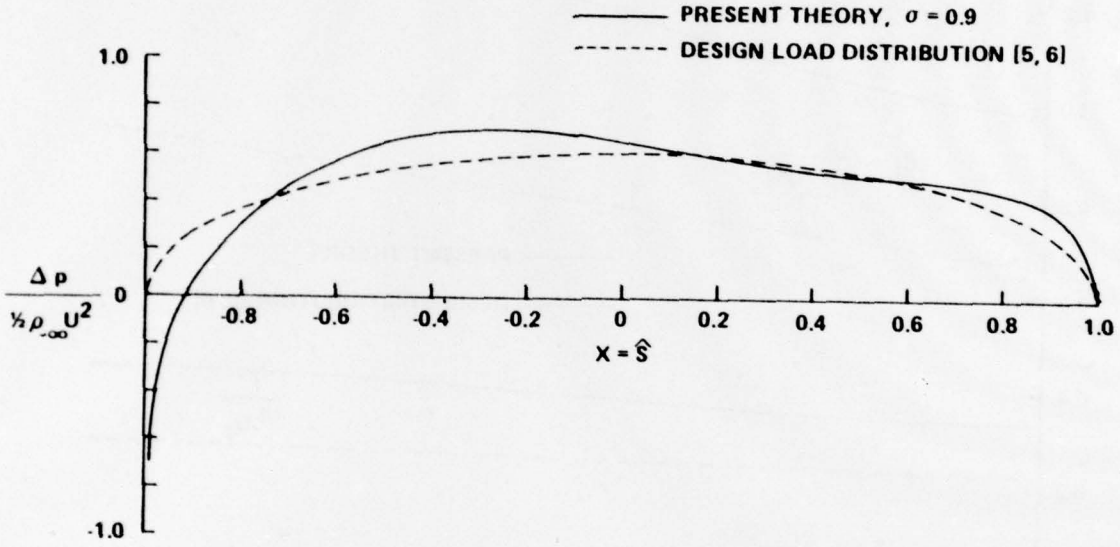

Figure 9 COMPARISON OF CHORDWISE LOAD DISTRIBUTIONS AT MID-ANNULUS FOR CASE 5

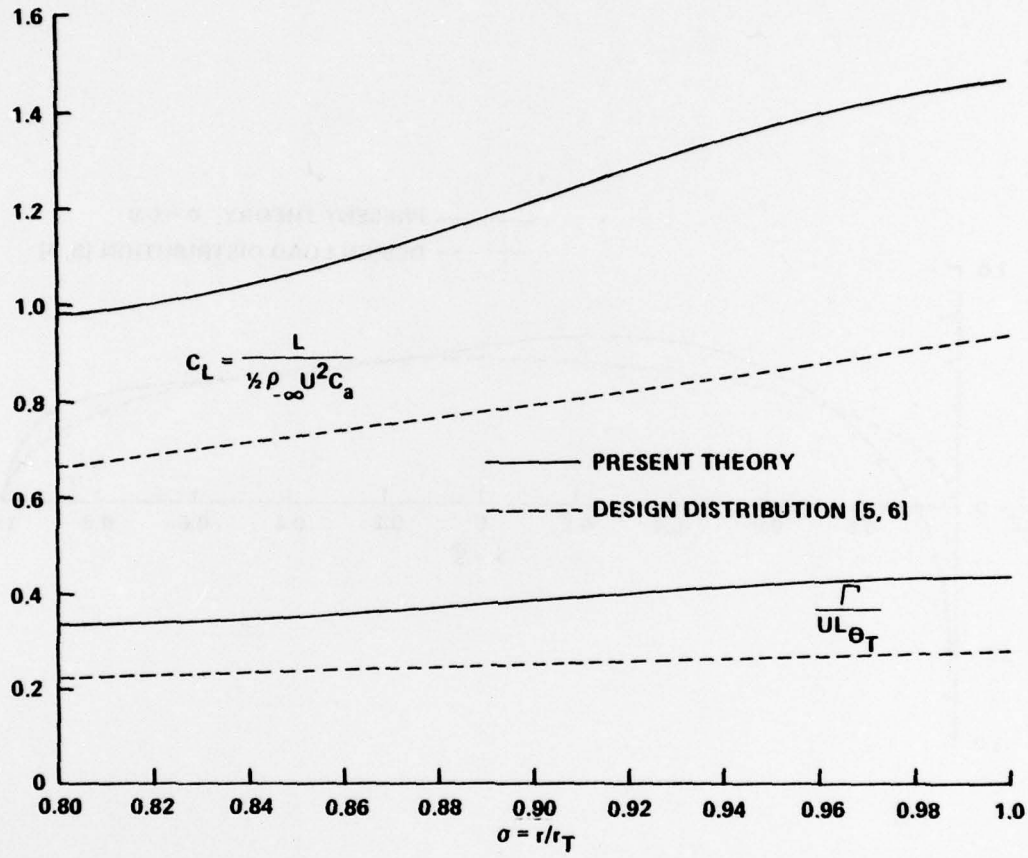

Figure 10 COMPARISON OF PRESENT THEORY WITH DESIGN VALUES OF OKUROUNMU AND McCUNE FOR CASE 6

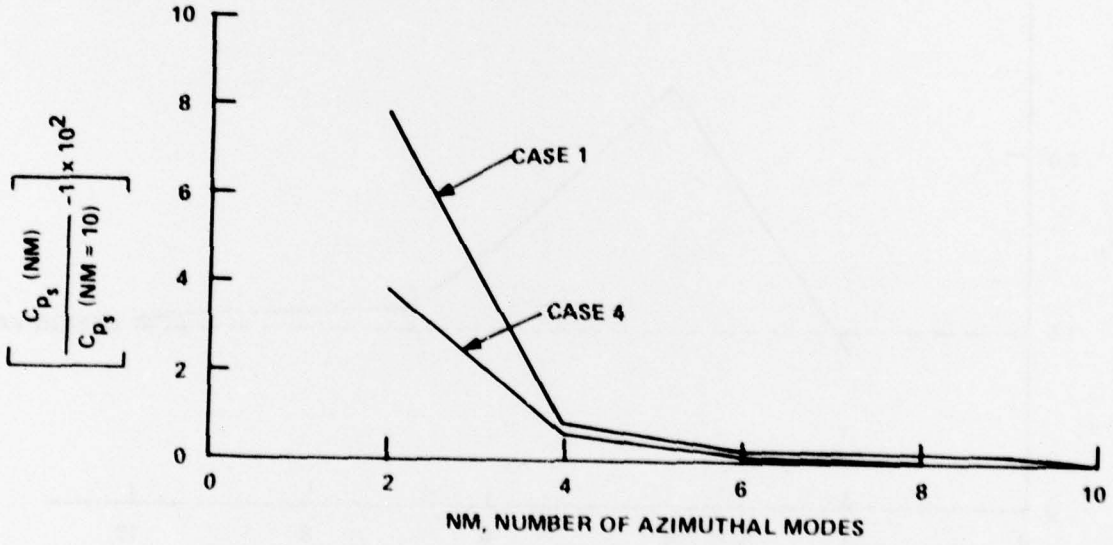

Figure 11 CONVERGENCE OF CALCULATIONS VS. NUMBER OF AZIMUTHAL MODES FOR CASES 1 AND 4

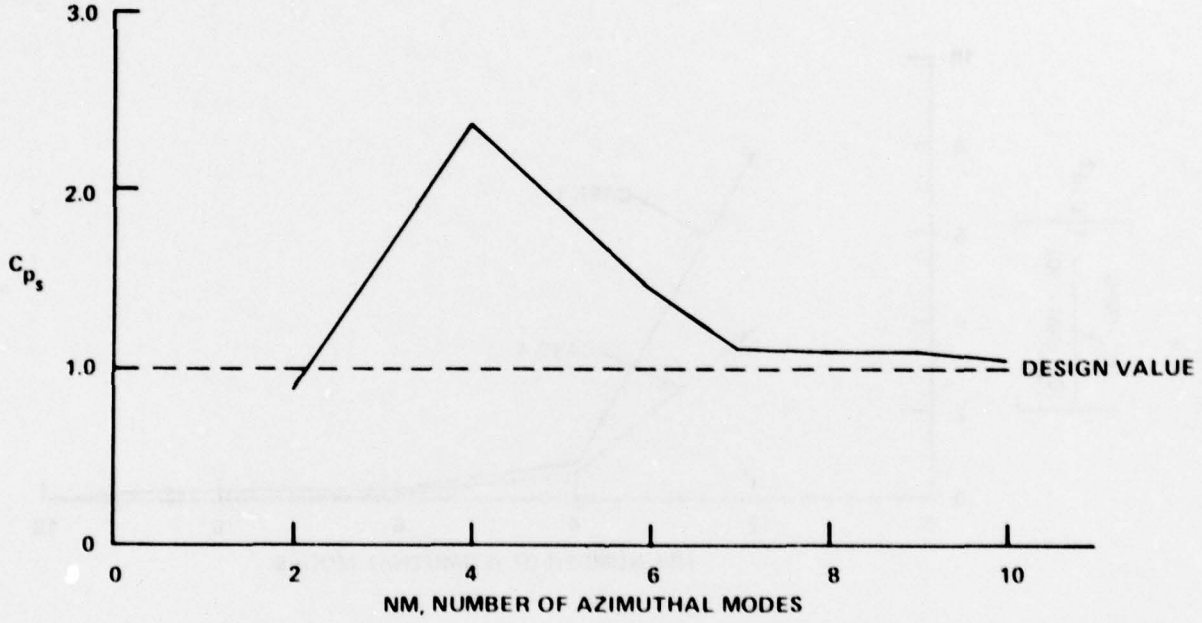

Figure 12 CONVERGENCE OF CALCULATIONS VS. NUMBER OF AZIMUTHAL MODES FOR CASE 5

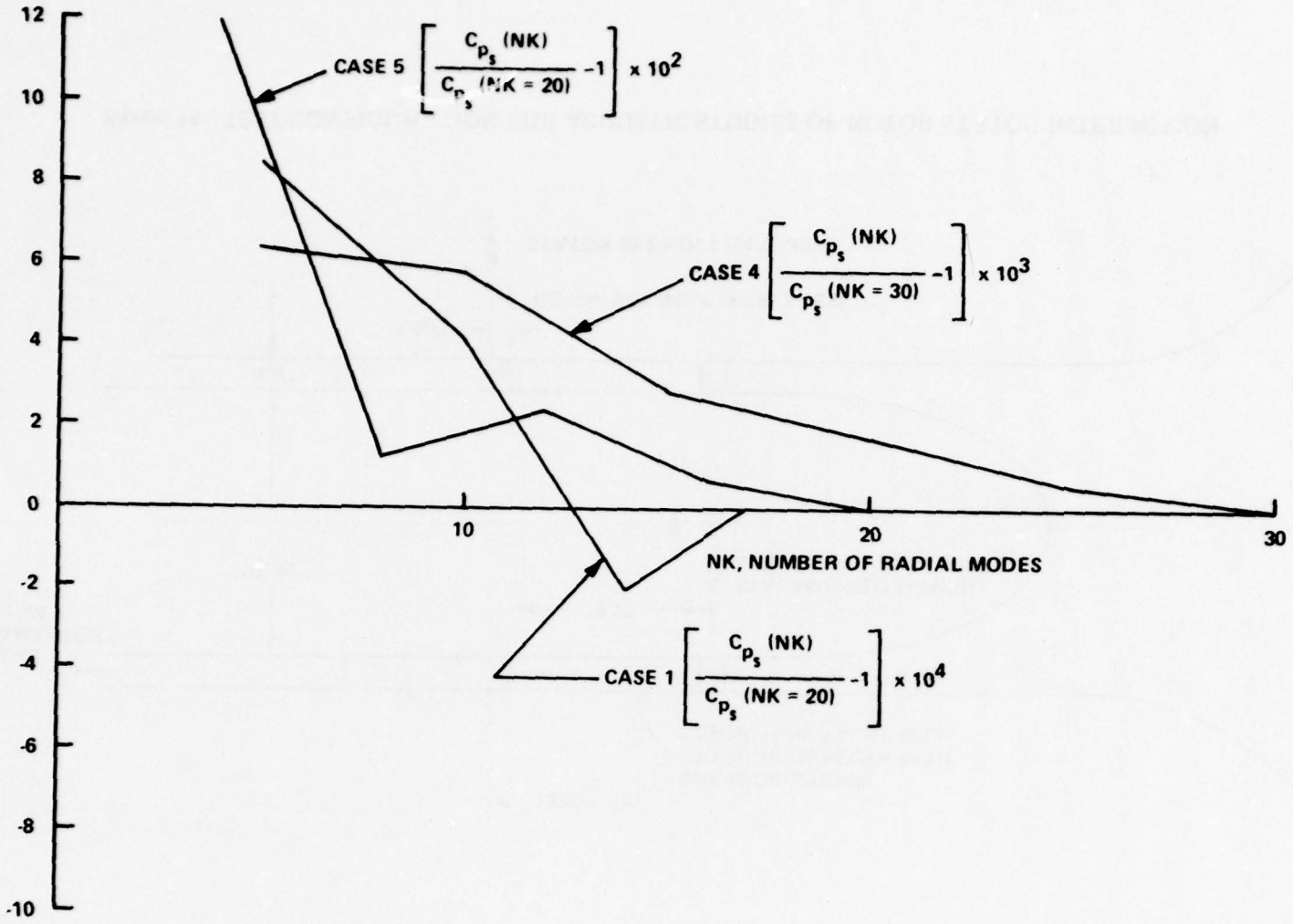

Figure 13 CONVERGENCE OF CALCULATIONS VS. NUMBER OF RADIAL MODES FOR CASES 1, 4 AND 5

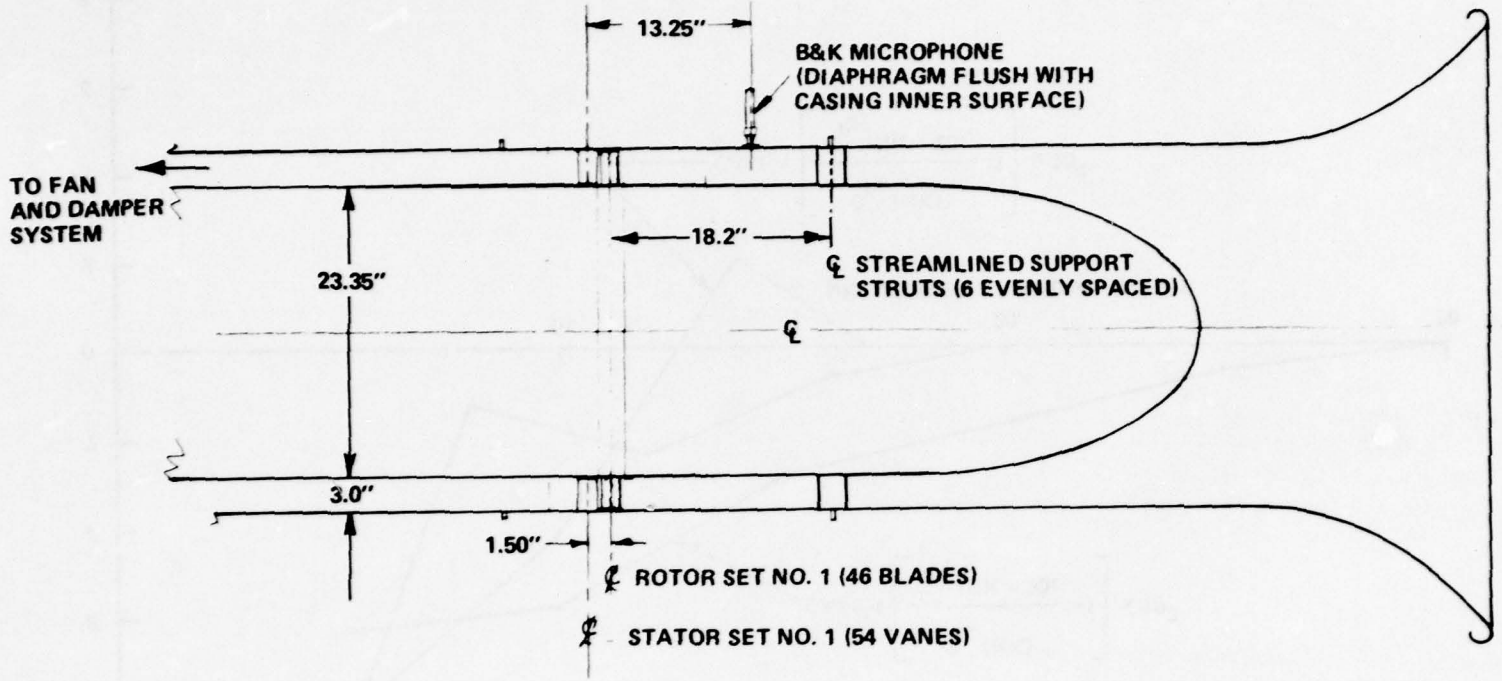

Figure 14 TEST CONFIGURATION FOR ACOUSTIC STUDIES OF ROTOR-STATOR INTERACTION

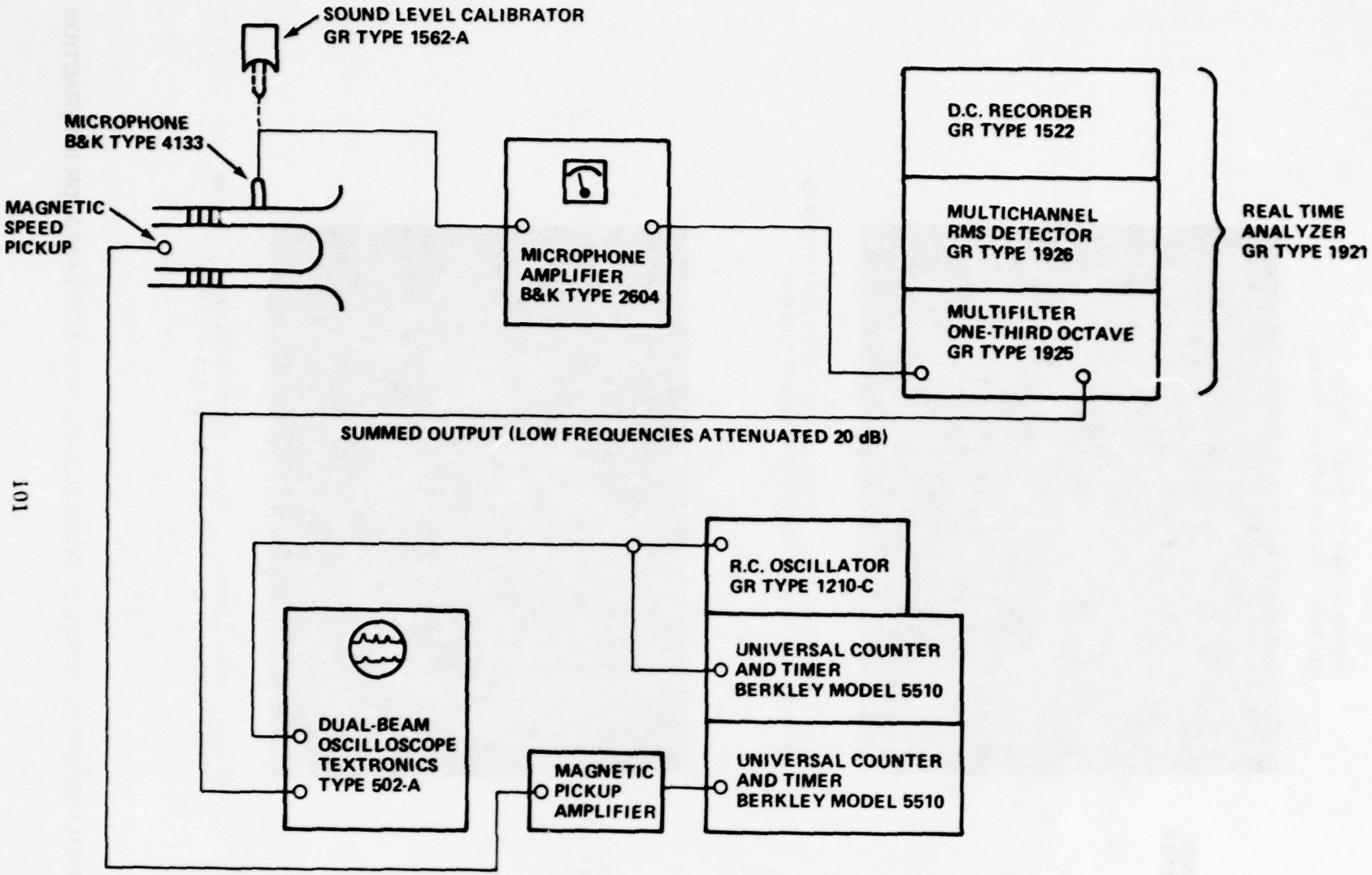

Figure 15 ACOUSTIC TEST INSTRUMENTATION

ROTOR STAGGER ANGLE - 40.0 deg
STATOR STAGGER ANGLE = 37.2 deg

REFERENCE OSCILLATOR SIGNAL

NOISE SIGNAL

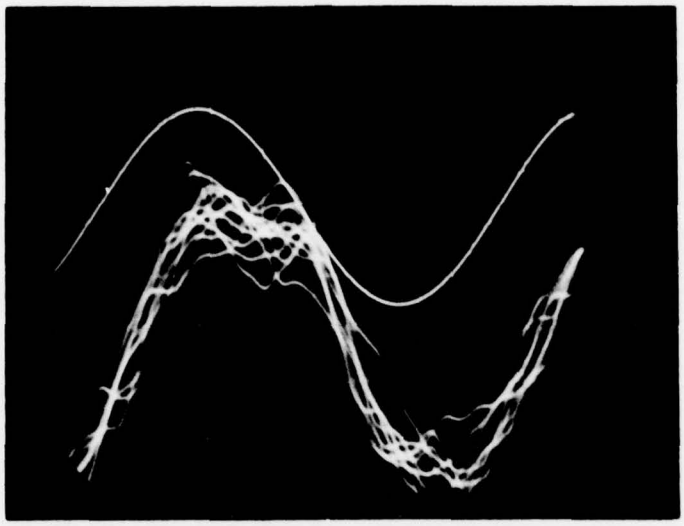

a) ROTOR RPM = 1695.5 OSCILLATOR FREQUENCY = 1300 Hz
CALCULATED BLADE PASSAGE FREQUENCY = 1300 Hz

REFERENCE OSCILLATOR SIGNAL

NOISE SIGNAL

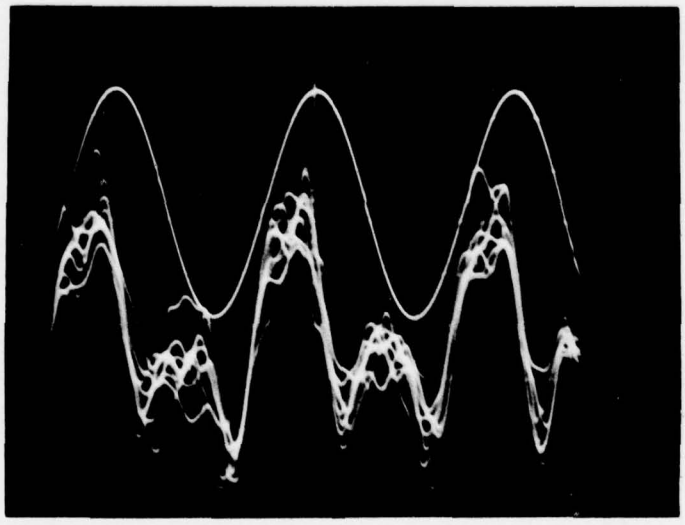

b) ROTOR RPM = 1710.5 OSCILLATOR FREQUENCY = 1312 Hz
CALCULATED BLADE PASSAGE FREQUENCY = 1311 Hz

Figure 16 OSCILLOSCOPE RECORDS OF NOISE SIGNAL FROM ROTOR-STATOR INTERACTION

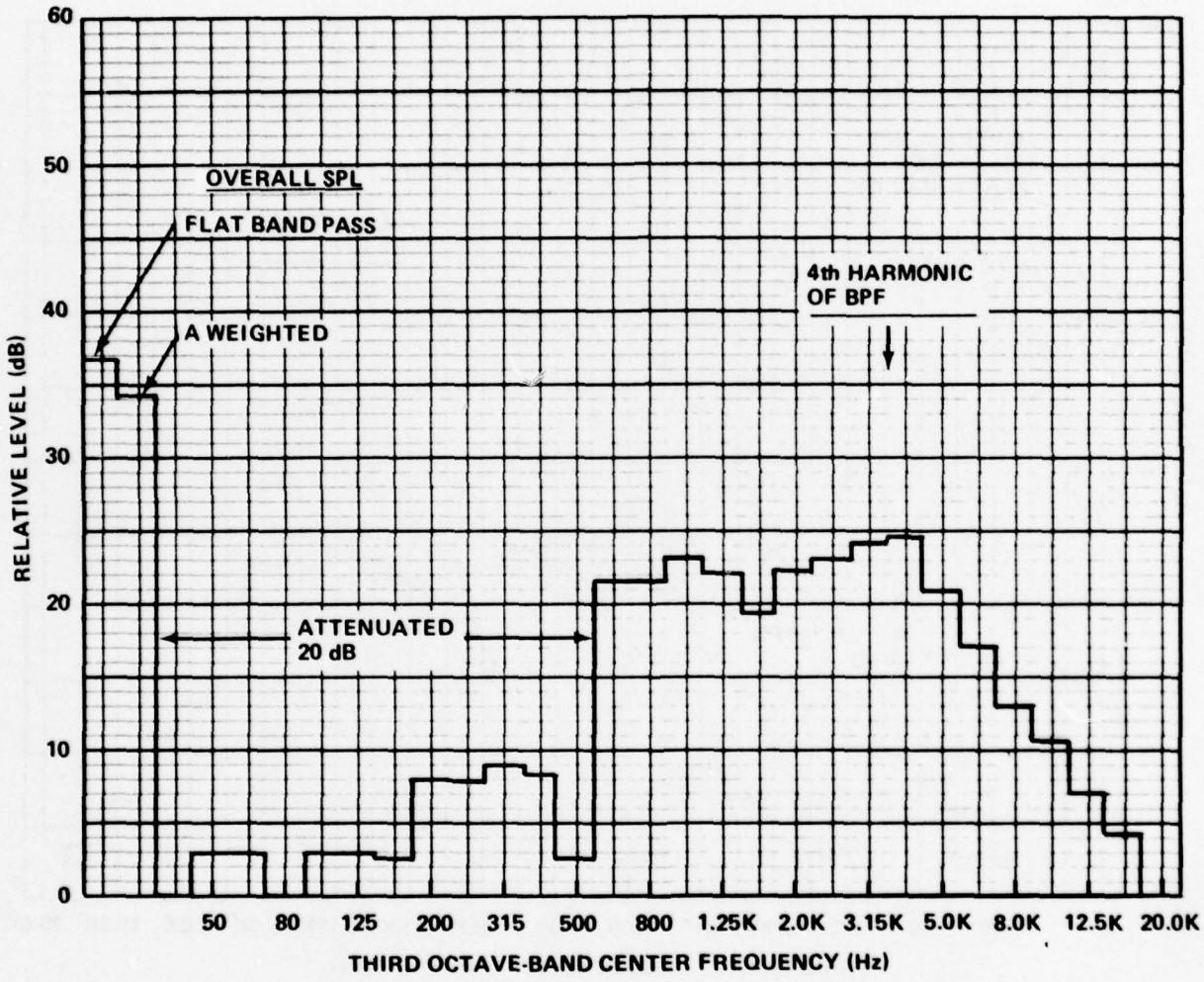

ID No. 01/15 – 28

FOR ABSOLUTE LEVEL ADD 80.0 dB

INTEGRATION TIME 4 SEC

4th HARMONIC FREQUENCY
MEASURED = ? Hz
CALCULATED = 3496 Hz

a) ROTOR RPM = 1140

Figure 17 UNCORRECTED 1/3 OCTAVE SPECTRUM OF OUTER WALL SOUND PRESSURE LEVEL FROM ROTOR-STATOR INTERACTION

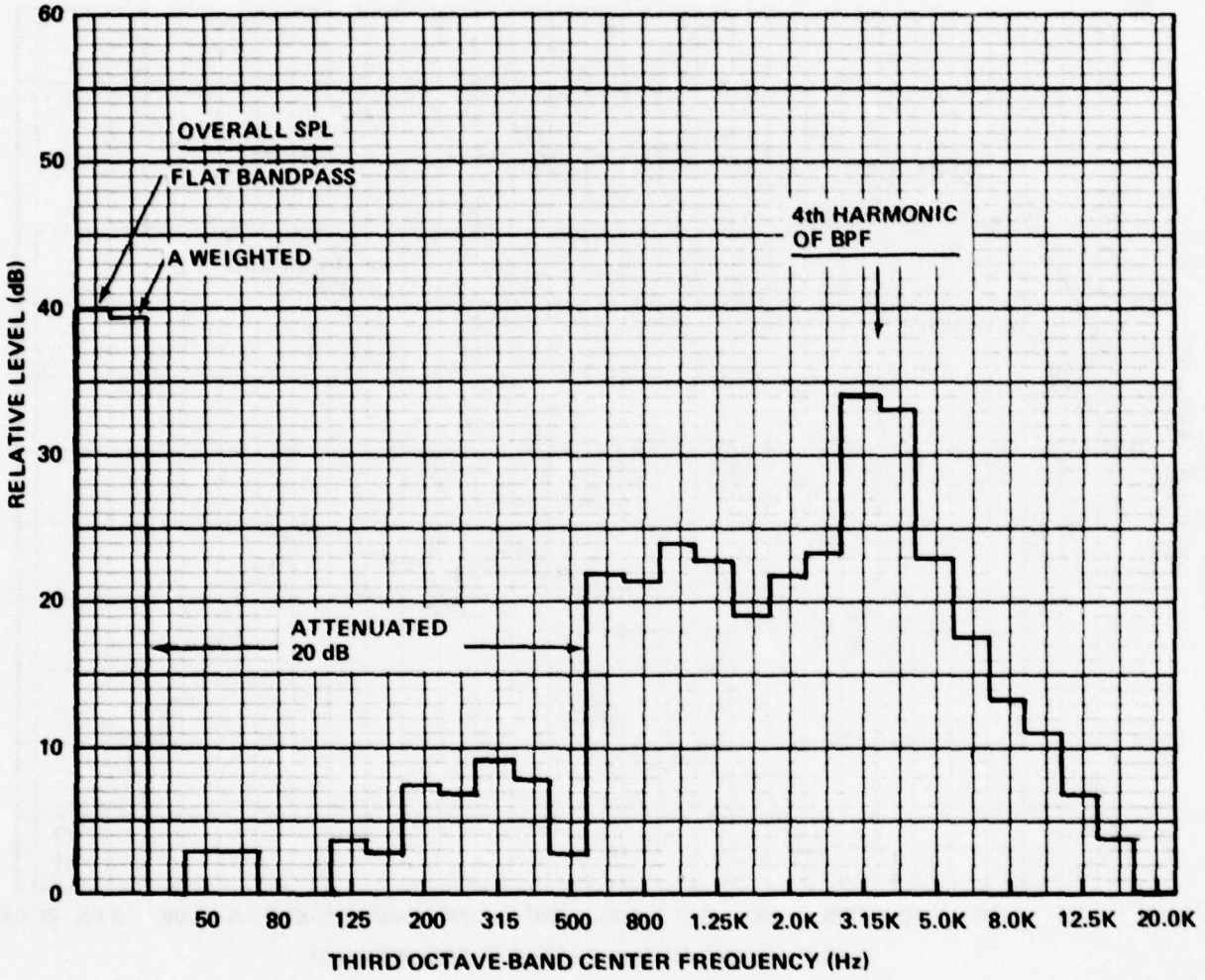

ID No. 01/15 -- 30

FOR ABSOLUTE LEVEL ADD 80.0 dB

INTEGRATION TIME 4 SEC

4th HARMONIC FREQUENCY
MEASURED = 3524 Hz
CALCULATED = 3527 Hz

b) ROTOR RPM = 1150

Figure 17 (Cont.) UNCORRECTED 1/3 OCTAVE SPECTRUM OF OUTER WALL SOUND PRESSURE LEVEL FROM ROTOR-STATOR INTERACTION

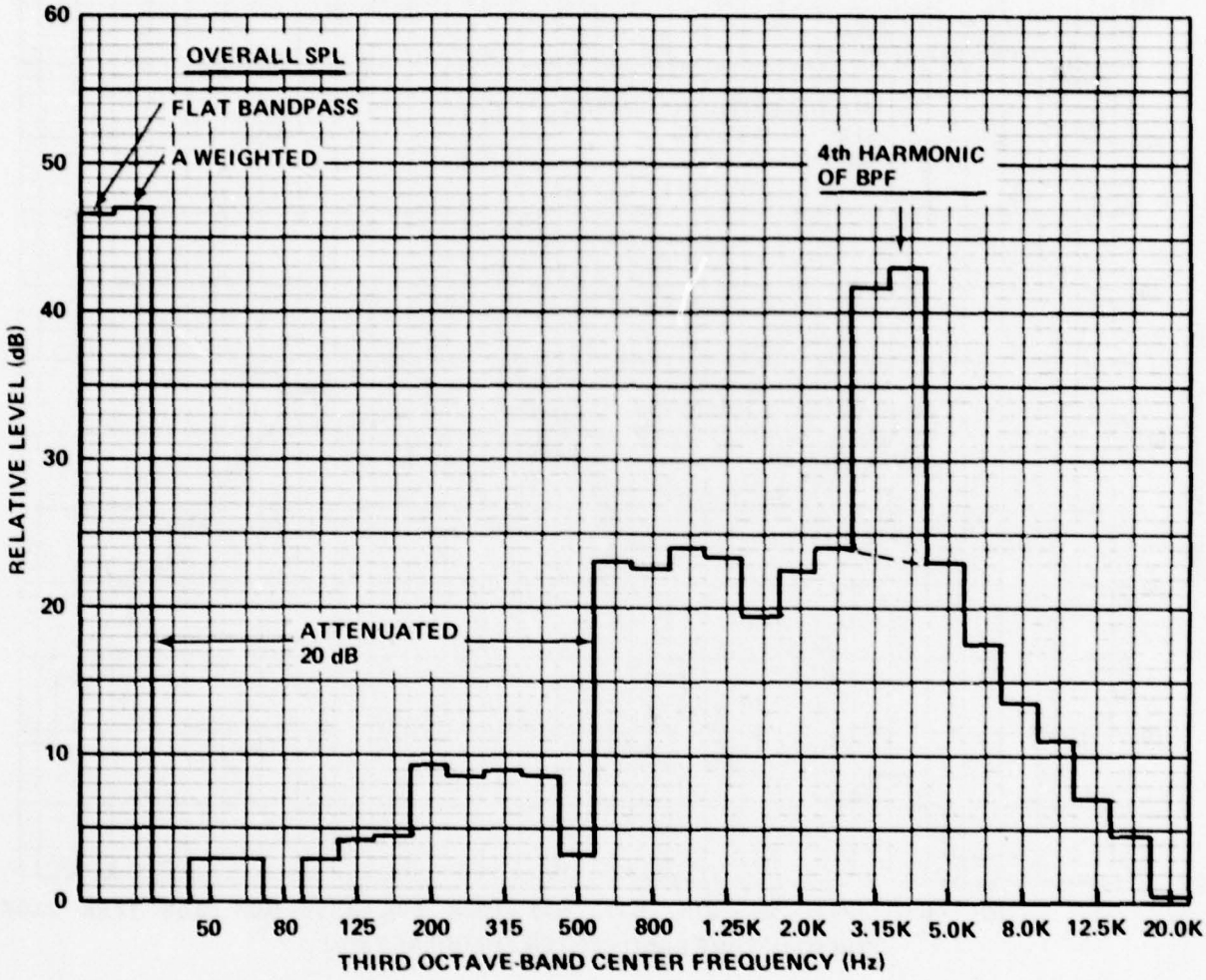

ID No. 01/15 – 32

FOR ABSOLUTE LEVEL ADD 80.0 dB

INTEGRATION TIME 4 SEC

4th HARMONIC FREQUENCY
MEASURED = 3560 Hz
CALCULATED = 3559 Hz

c) ROTOR RPM = 1160.5

Figure 17 (Cont.) UNCORRECTED 1/3 OCTAVE SPECTRUM OF OUTER WALL SOUND PRESSURE LEVEL FROM ROTOR-STATOR INTERACTION

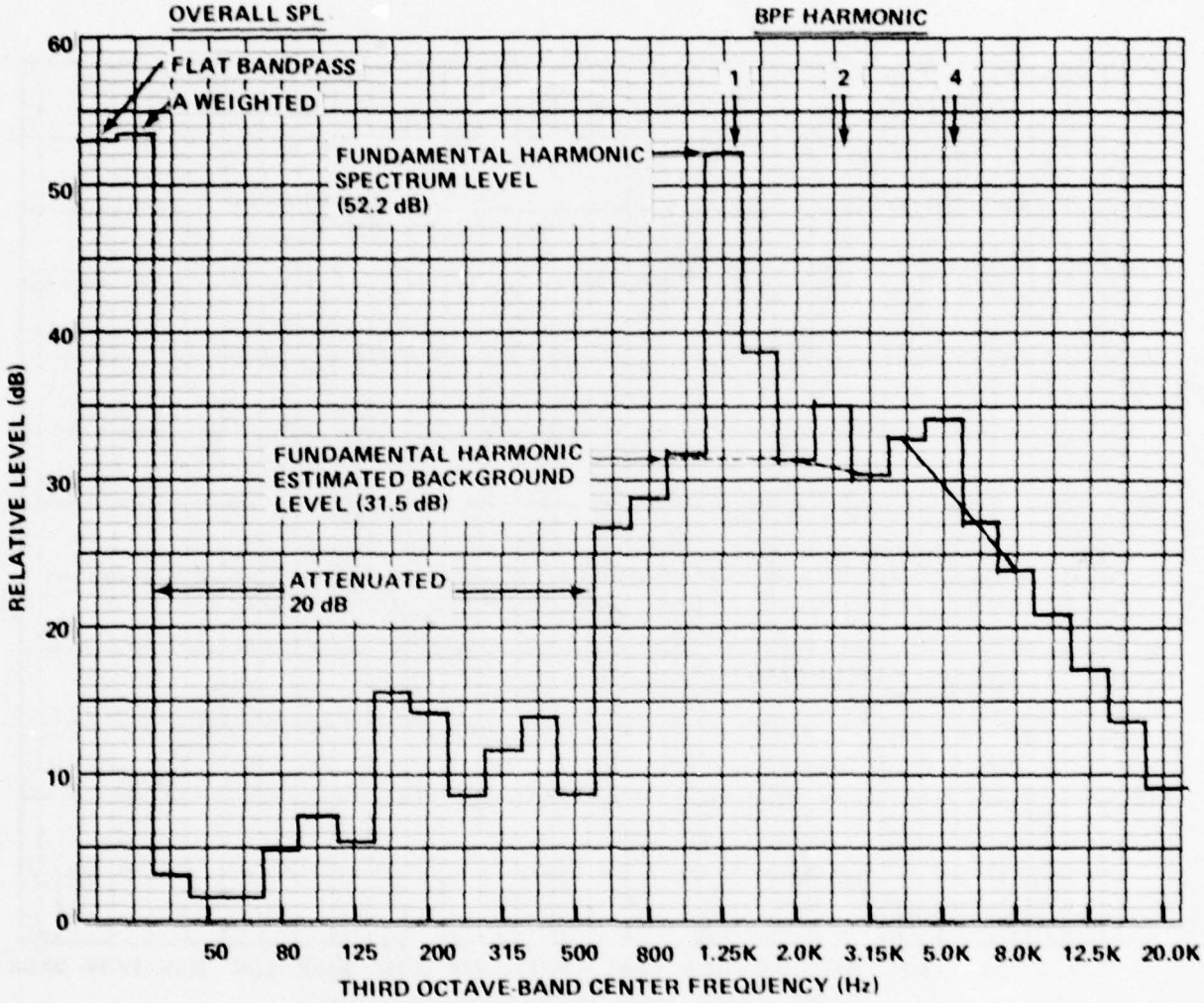

ID No. 01/25 – 6

FOR ABSOLUTE LEVEL ADD 80.5 dB

INTEGRATION TIME 4 SEC

FUNDAMENTAL HARMONIC FREQUENCY
MEASURED = 1300 Hz
CALCULATED = 1300 Hz

a) ROTOR RPM = 1695.5

Figure 18 UNCORRECTED 1/3 OCTAVE SPECTRUM OF OUTER WALL SOUND PRESSURE LEVEL FROM ROTOR-STATOR INTERACTION

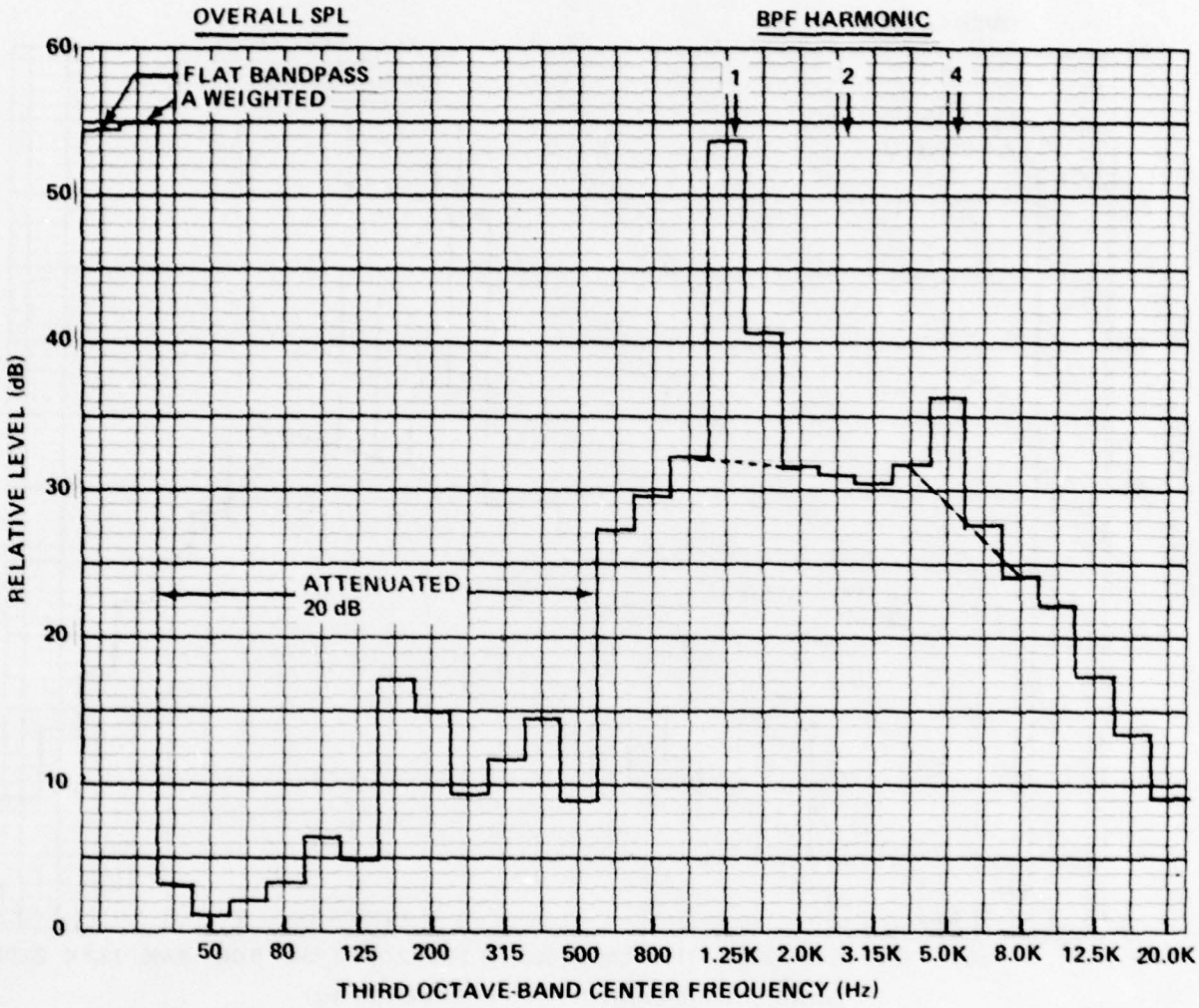

ID No. 01/25 – 7

FOR ABSOLUTE LEVEL ADD 80.5 dB

INTEGRATION TIME 4 SEC

FUNDAMENTAL HARMONIC FREQUENCY
MEASURED = 1303 Hz
CALCULATED = 1304 Hz

b) ROTOR RPM = 1700.5

Figure 18 (Cont.) UNCORRECTED 1/3 OCTAVE SPECTRUM OF OUTER WALL SOUND PRESSURE LEVEL FROM ROTOR-STATOR INTERACTION

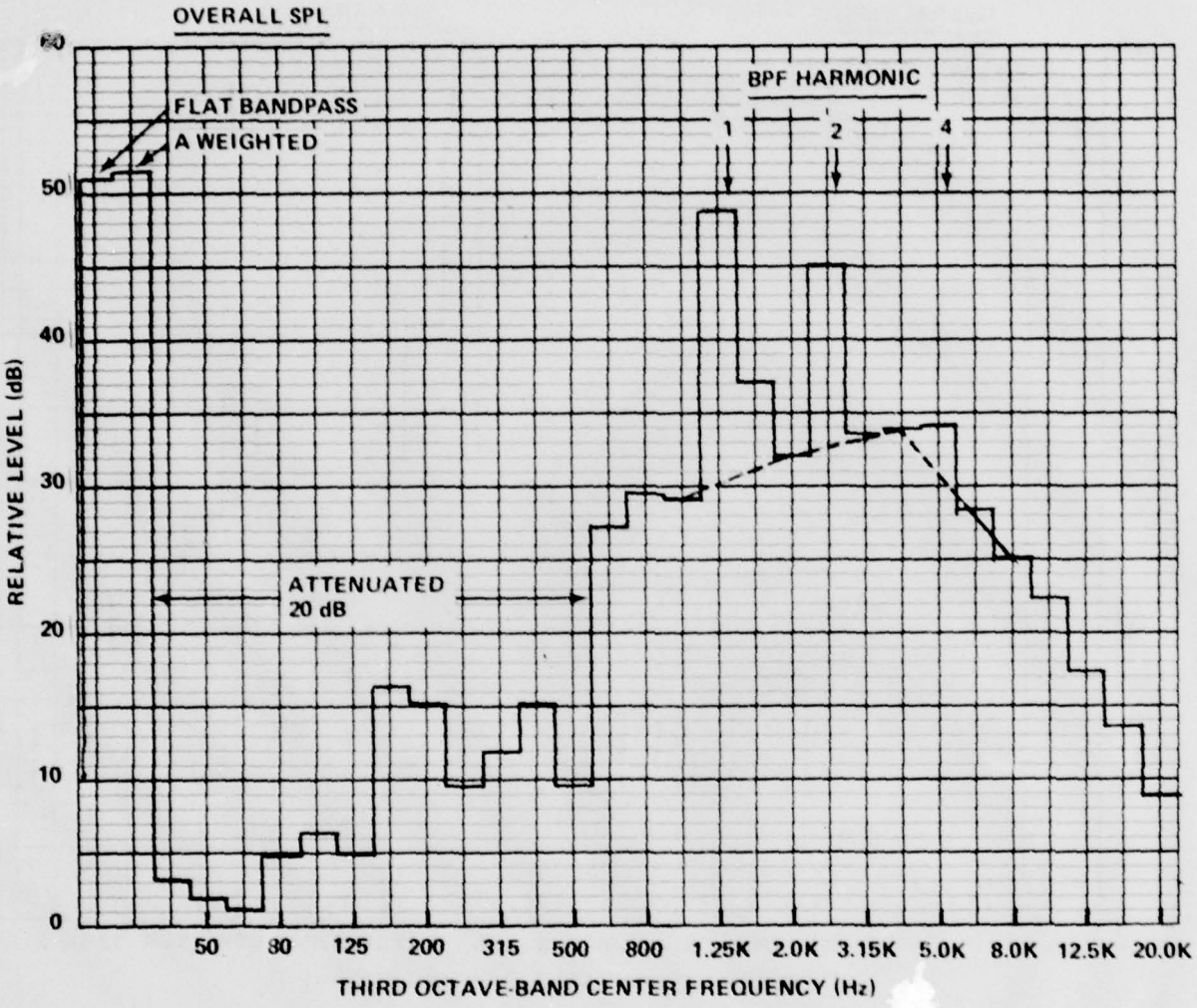

ID No. 01/25 – 8

FOR ABSOLUTE LEVEL ADD 80.5 dB

INTEGRATION TIME 4 SEC

FUNDAMENTAL HARMONIC FREQUENCY
MEASURED = 1312 Hz
CALCULATED = 1311 Hz

c) ROTOR RPM = 1710.5

Figure 18 (Cont.) UNCORRECTED 1/3 OCTAVE SPECTRUM OF OUTER WALL SOUND PRESSURE LEVEL FROM ROTOR-STATOR INTERACTION

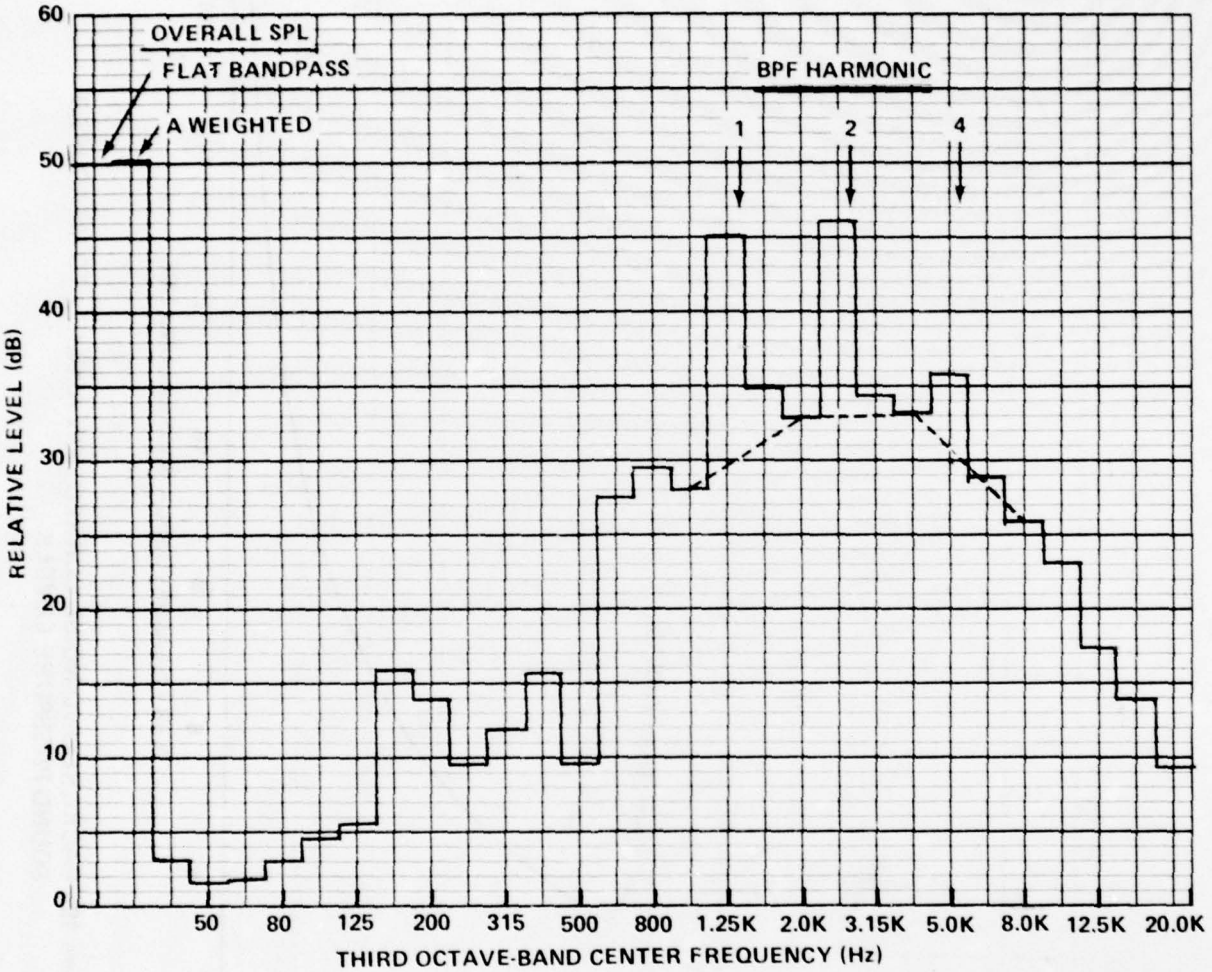

ID No. 01/25 – 9

FOR ABSOLUTE LEVEL ADD 80.5 dB

INTEGRATION TIME 4 SEC

FUNDAMENTAL HARMONIC FREQUENCY
MEASURED = 1316 Hz
CALCULATED = 1316 Hz

d) ROTOR RPM = 1716

Figure 18 (Cont.) UNCORRECTED 1/3 OCTAVE SPECTRUM OF OUTER WALL SOUND PRESSURE LEVEL FROM ROTOR-STATOR INTERACTION

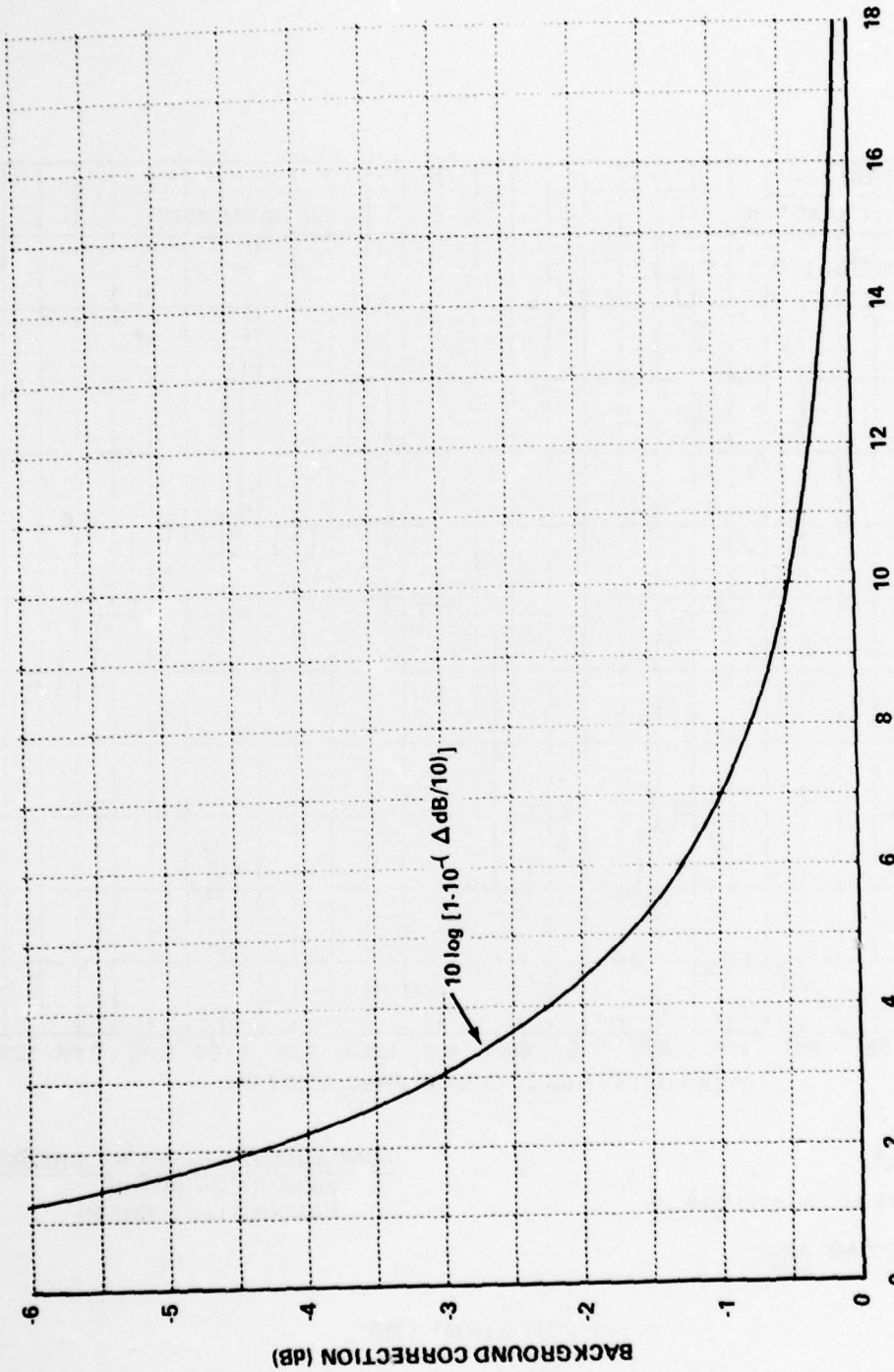

Figure 19 BACKGROUND NOISE CORRECTION APPLIED TO MEASURED SOUND PRESSURE LEVELS

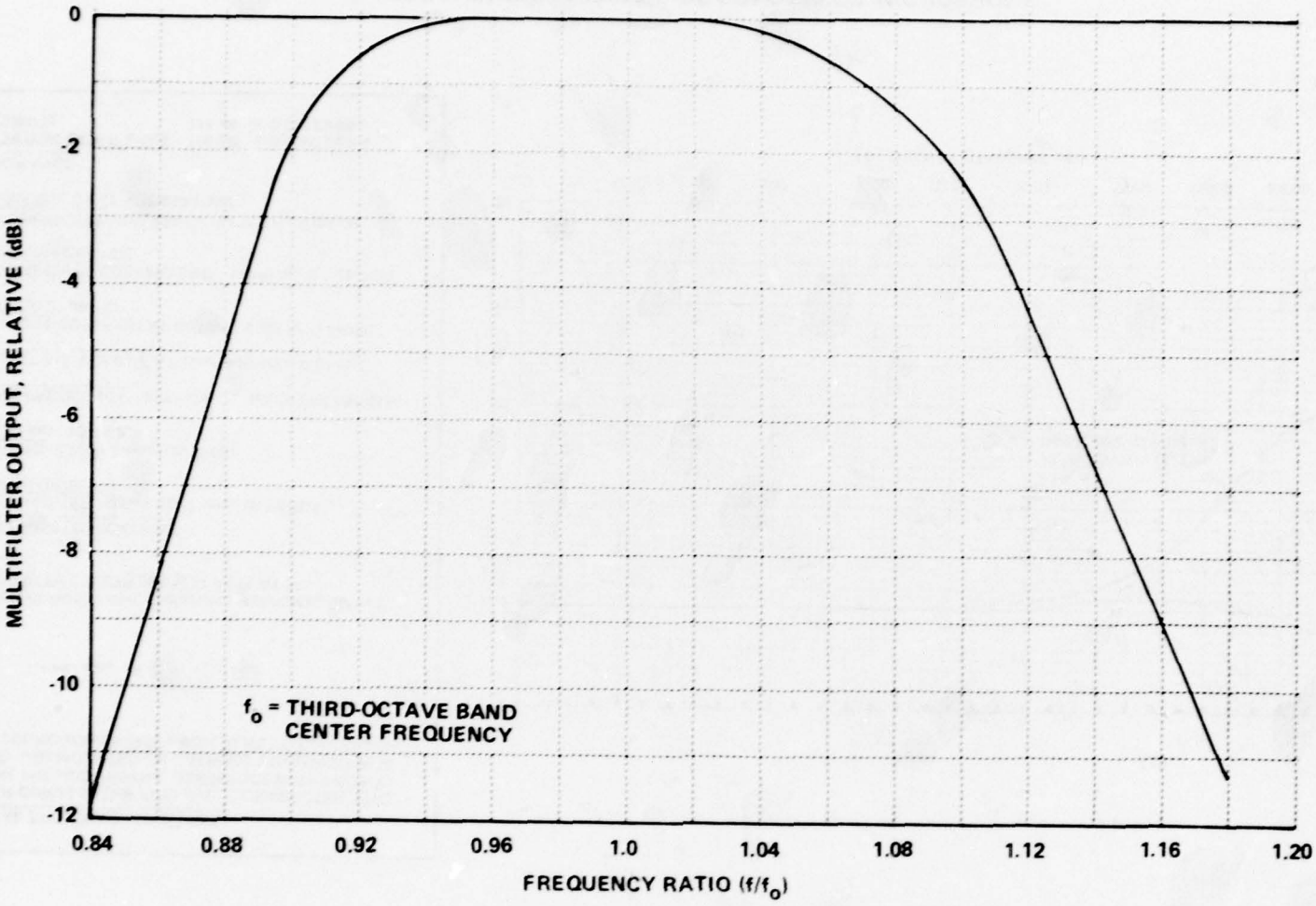

Figure 20 MEASURED FREQUENCY RESPONSE OF MULTIFILTERS IN REAL TIME ANALYZER

INDIVIDUAL FREQUENCY RESPONSE:

THE UPPER CURVE IS THE FREE FIELD CHARACTERISTIC, VALID FOR THE MICROPHONE CARTRIDGE WITH PROTECTION GRID AND MOUNTED ON CATHODE FOLLOWER 2614 OR 2615. SOUND WAVES PERPENDICULAR TO DIAPHRAGM.

THE LOWER CURVE IS THE PRESSURE RESPONSE CURVE RECORDED WITH ELECTROSTATIC ACTUATOR.

SUMMARIZED SPECIFICATIONS

OUTSIDE DIAMETER: 0.5 in. (12.7 mm), WITHOUT PROTECTING GRID.

GRID THREAD (COUPLER MOUNTING): 0.5 in. (12.7 mm) - 60-NS 2.

RESONANT FREQUENCY: APPROX. 25 Hz (OVERDAMPED).

EQUIVALENT AIR VOLUME AT atm: APPROX. 0.01 cm^3.

TEMPERATURE COEFFICIENT BETWEEN -50 AND +60°C: LESS THAN ±0.01 dB/°C.

AMBIENT PRESSURE COEFFICIENT: APPROX. -0.1 dB FOR +10% PRESSURE CHANGE.

RELATIVE HUMIDITY INFLUENCE: LESS THAN 0.1 dB, IN THE ABSENCE OF CONDENSATION.

DYNAMIC RANGE:

4% DISTORTION UPPER LIMIT: 160 dB, re. 0.0002 μBAR
SAFETY LIMIT: 174 dB, re. 0.0002 μBAR

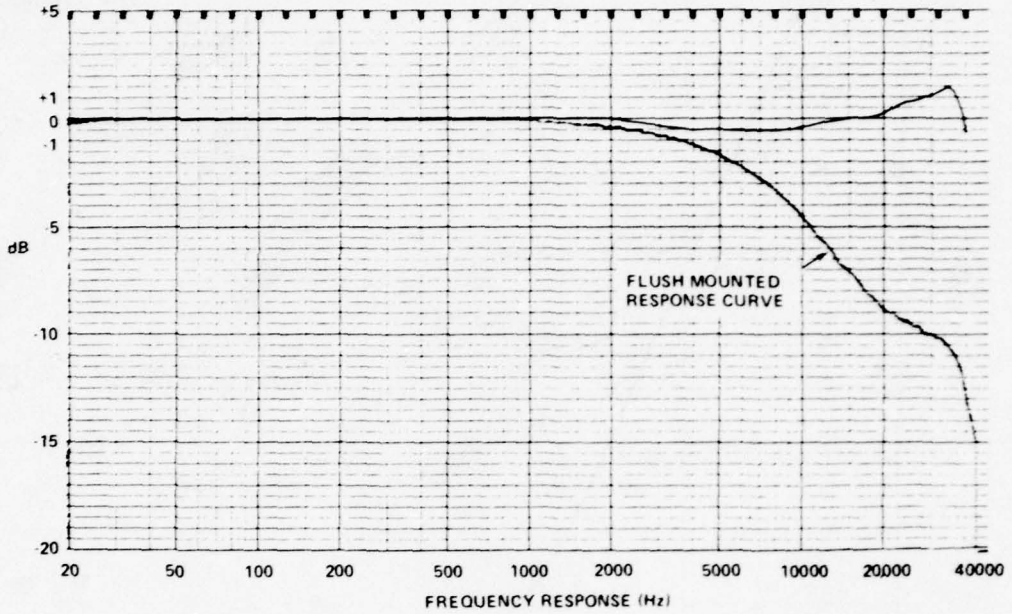

Figure 21 FREQUENCY RESPONSE OF CONDENSER MICROPHONE

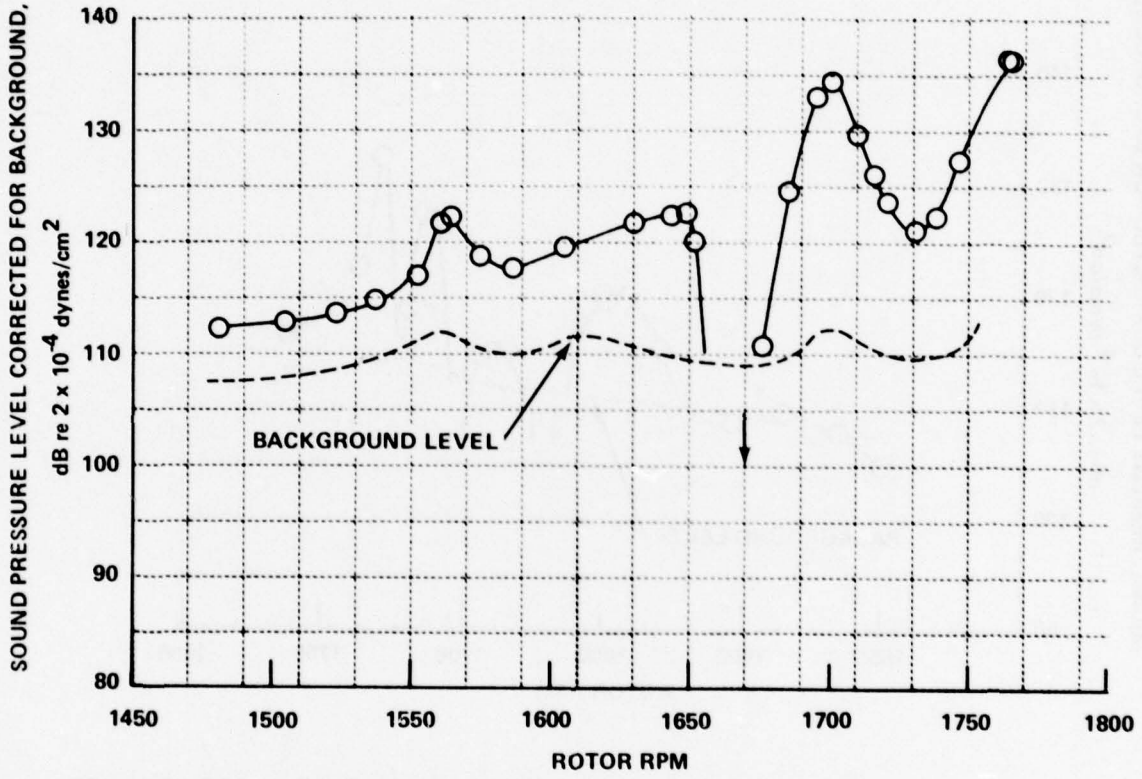

Figure 22 RMS WALL PRESSURE AT BLADE PASSAGE FREQUENCY, STATOR STAGGER ANGLE δ_{SM} = 37.2 deg

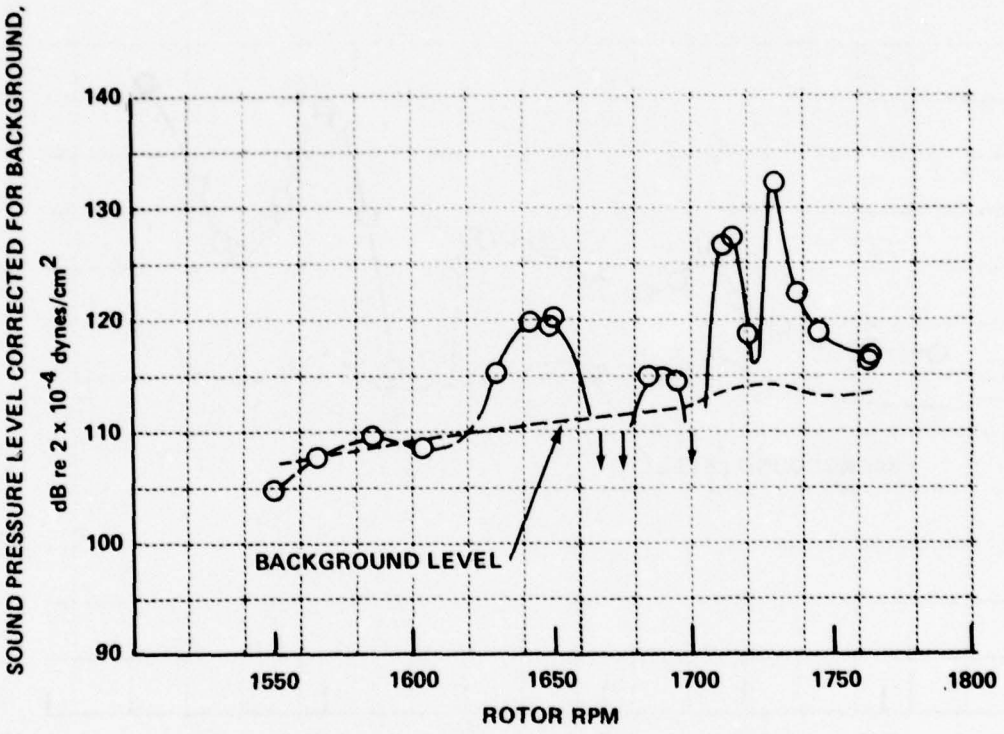

Figure 23 RMS WALL PRESSURE AT SECOND HARMONIC OF BLADE PASSAGE FREQUENCY, STATOR STAGGER ANGLE, δ_{SM} = 37.2 deg

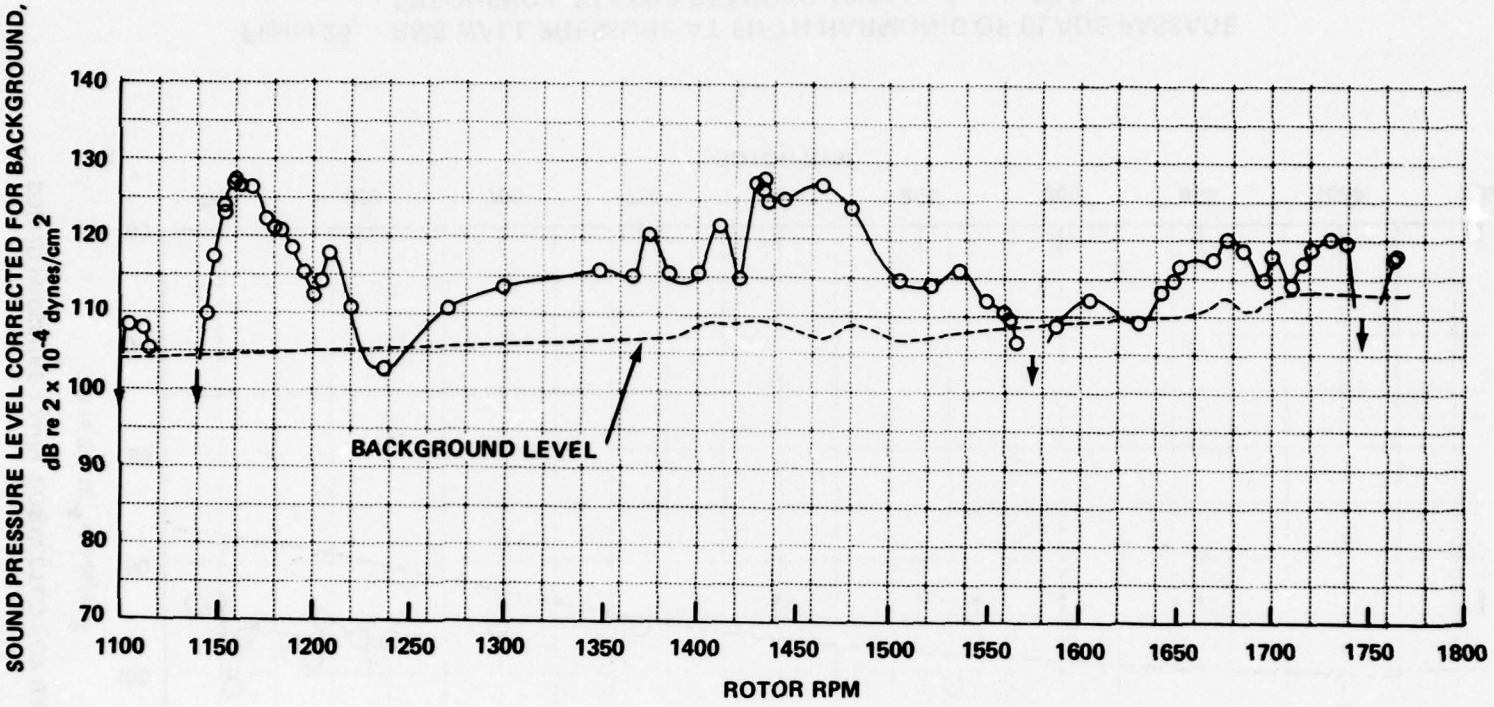

Figure 24 RMS WALL PRESSURE AT FOURTH HARMONIC OF BLADE PASSAGE FREQUENCY, STATOR STAGGER ANGLE, δ_{SM} = 37.2 deg

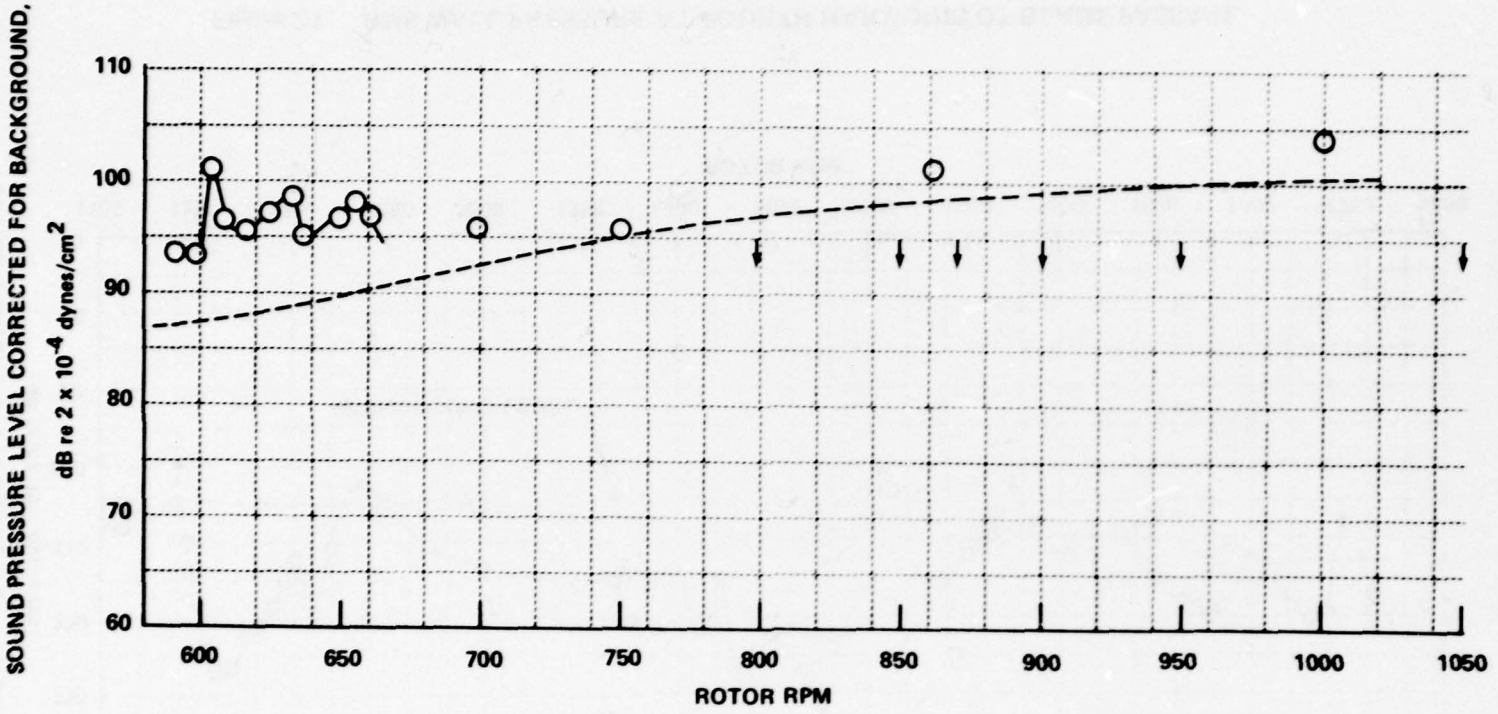

Figure 25 RMS WALL PRESSURE AT FIFTH HARMONIC OF BLADE PASSAGE FREQUENCY, STATOR STAGGER ANGLE, δ_{SM} = 37.2 deg

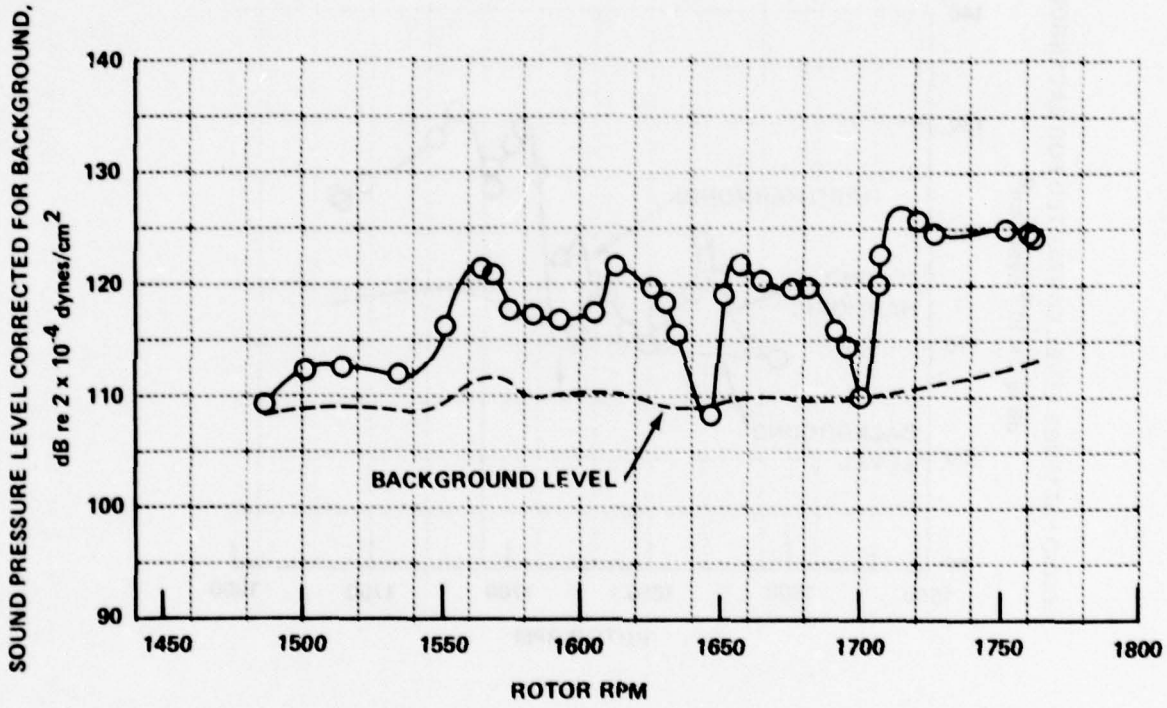

Figure 26 RMS WALL PRESSURE AT BLADE PASSAGE FREQUENCY, STATOR STAGGER ANGLE δ_{SM} = 28.2 deg

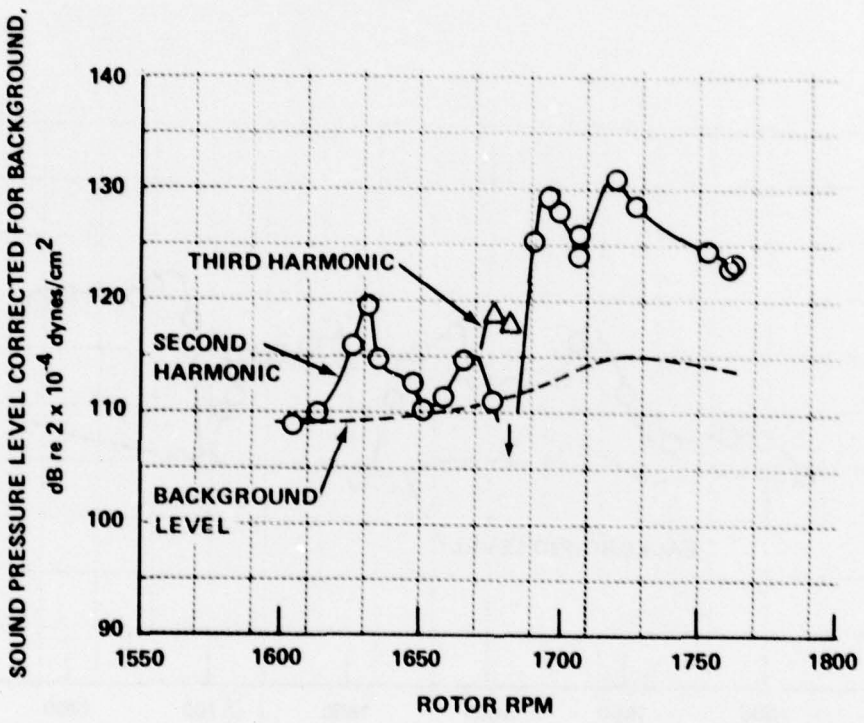

Figure 27 RMS WALL PRESSURE AT SECOND AND THIRD HARMONICS OF BLADE PASSAGE FREQUENCY, STATOR STAGGER ANGLE, δ_{SM} = 28.2 deg

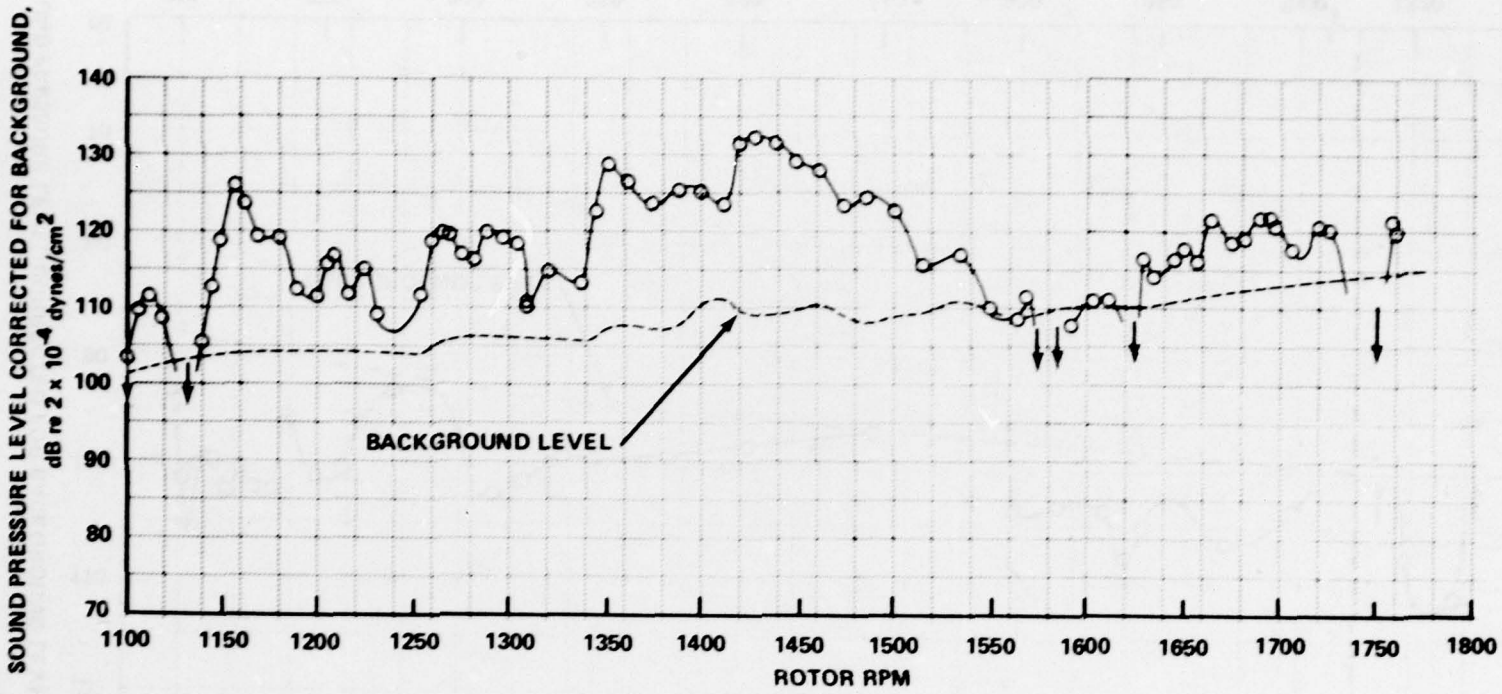

Figure 28 RMS WALL PRESSURE AT FOURTH HARMONIC OF BLADE PASSAGE FREQUENCY, STATOR STAGGER ANGLE, δ_{SM} = 28.2 deg

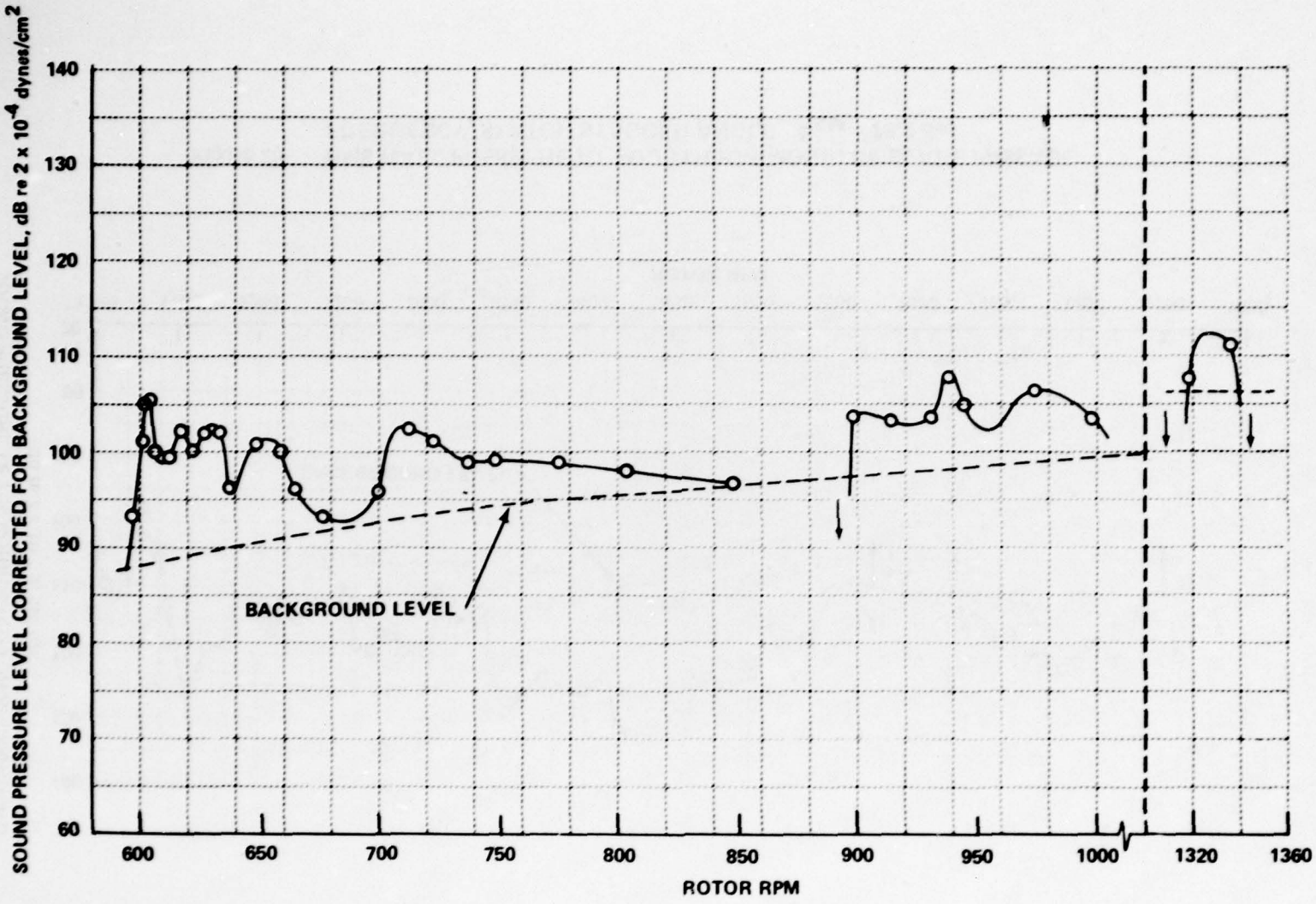

Figure 29 RMS WALL PRESSURE AT FIFTH HARMONIC OF BLADE PASSAGE FREQUENCY, STATOR STAGGER ANGLE, δ_{SM} = 28.2 deg

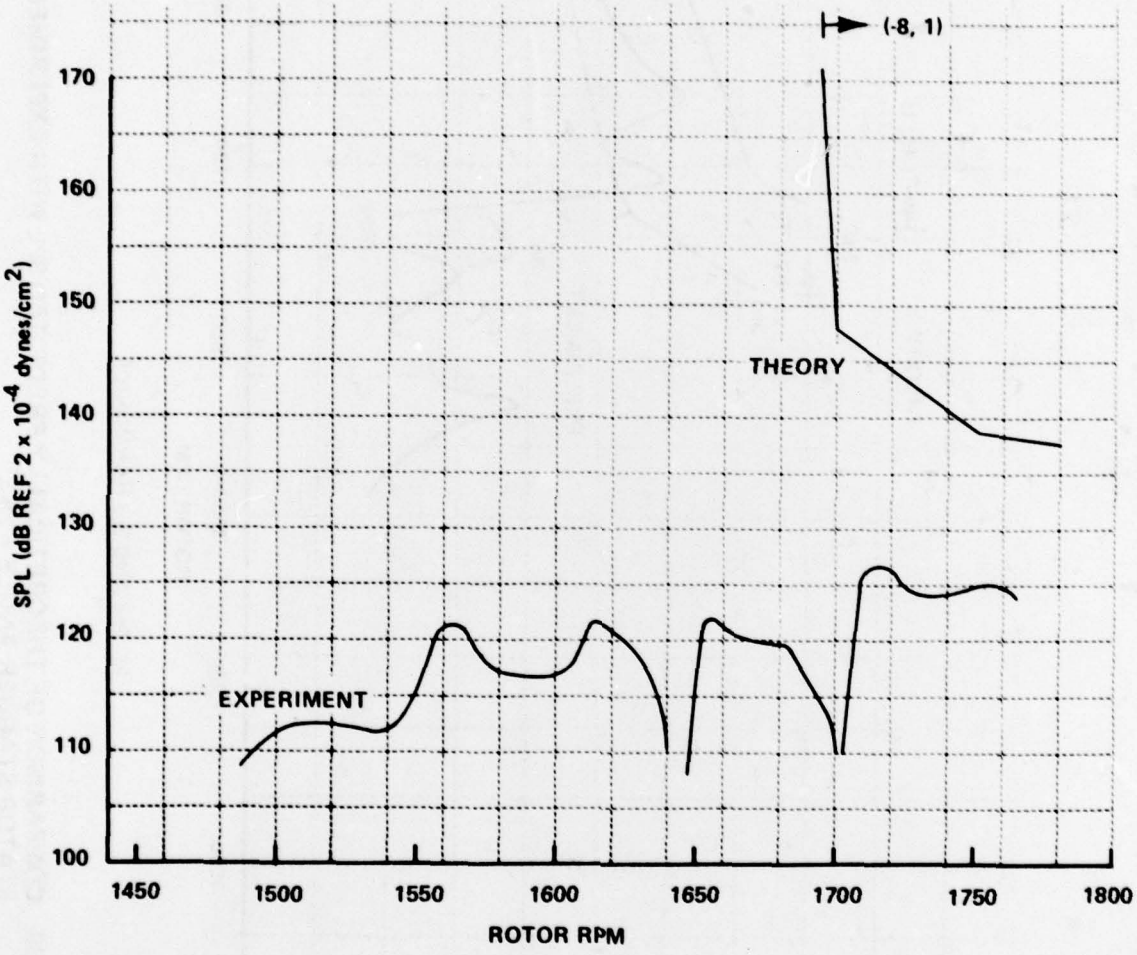

a) BLADE PASSAGE FREQUENCY

Figure 30 COMPARISON OF THEORETICALLY PREDICTED SPL WITH EXPERIMENT; STATOR STAGGER ANGLE = 28.2°

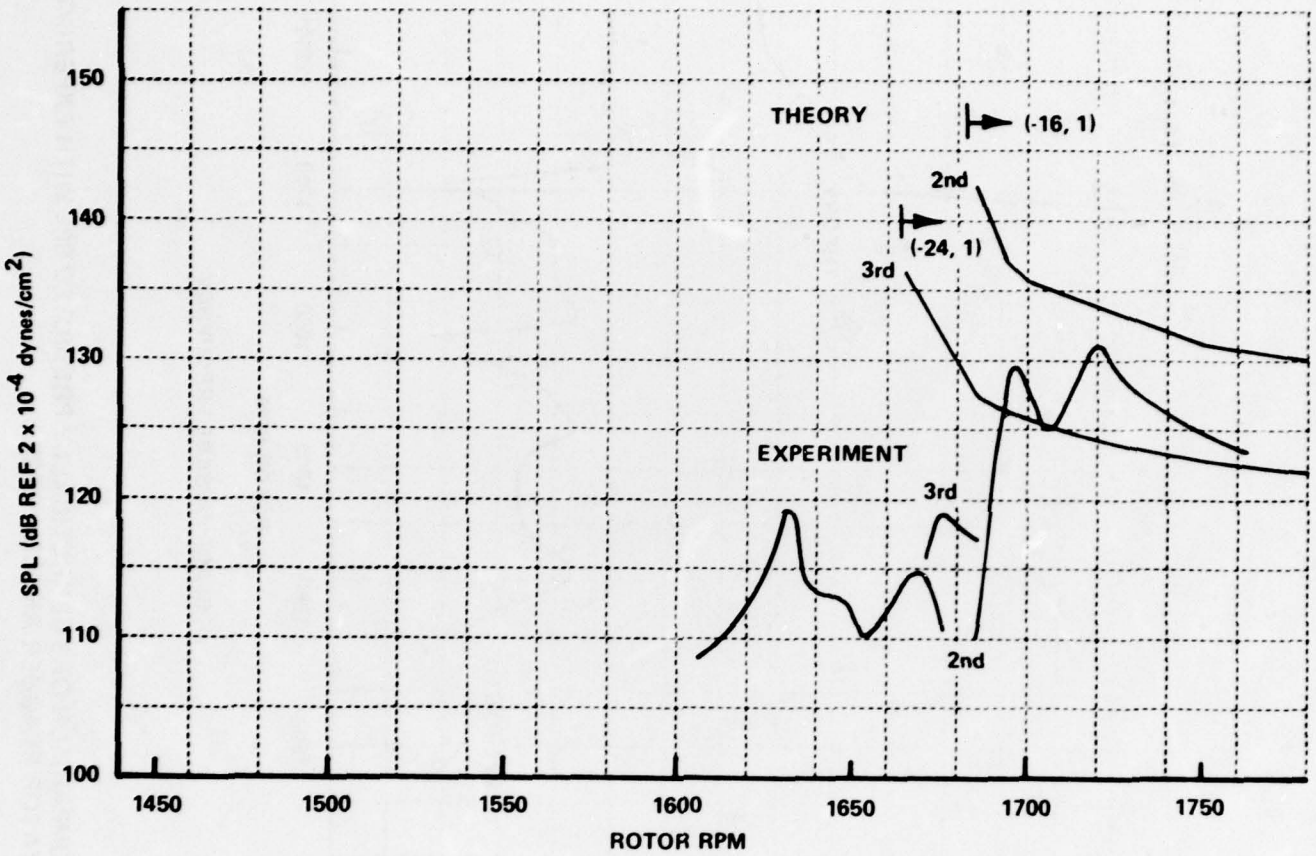

b) 2nd AND 3rd HARMONICS

Figure 30 COMPARISON OF THEORETICALLY PREDICTED SPL WITH EXPERIMENT; STATOR STAGGER ANGLE = 28.2°

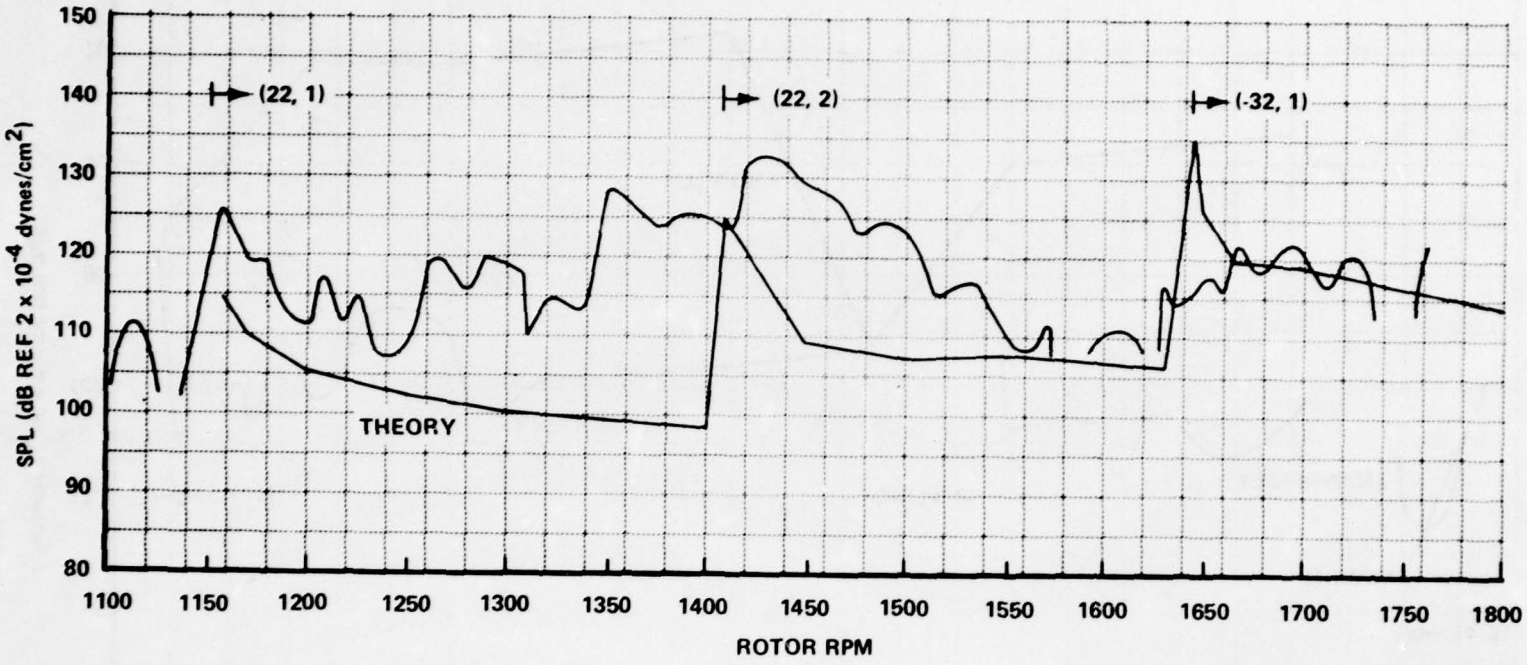

c) 4th HARMONIC

Figure 30 COMPARISON OF THEORETICALLY PREDICTED SPL WITH EXPERIMENT; STATOR STAGGER ANGLE = 28.2°

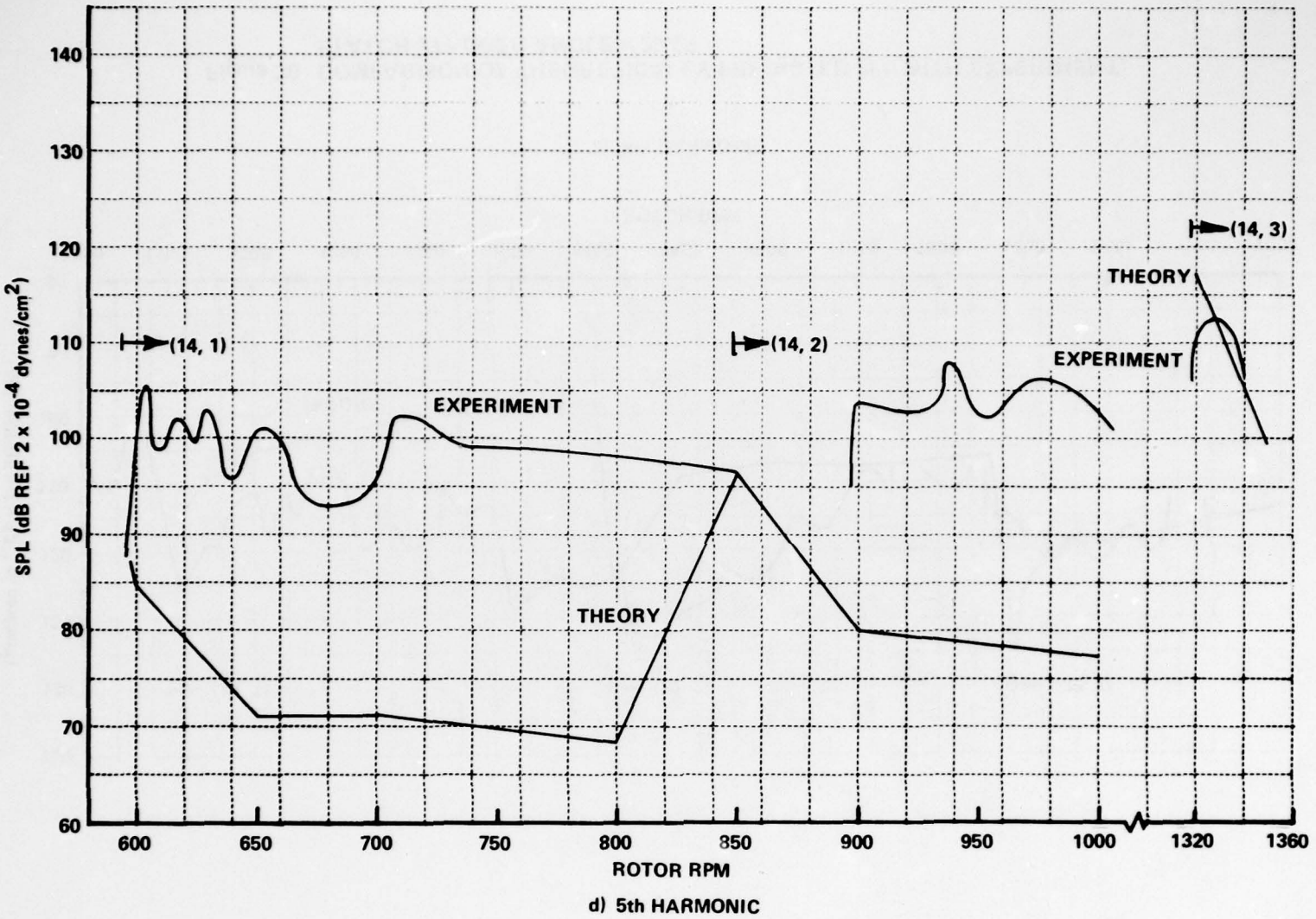

d) 5th HARMONIC

Figure 30 COMPARISON OF THEORETICALLY PREDICTED SPL WITH EXPERIMENT; STATOR STAGGER ANGLE = 28.2°

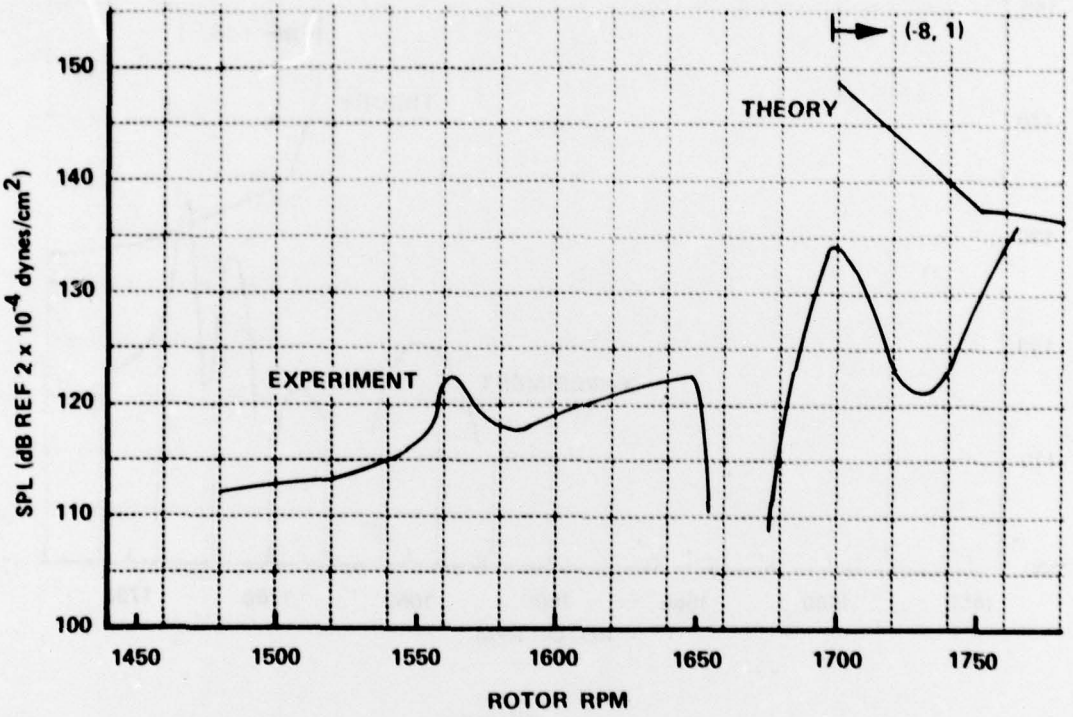

a) BLADE PASSAGE FREQUENCY

Figure 31 COMPARISON OF THEORETICALLY PREDICTED SPL WITH EXPERIMENT; STATOR STAGGER ANGLE = 37.2°

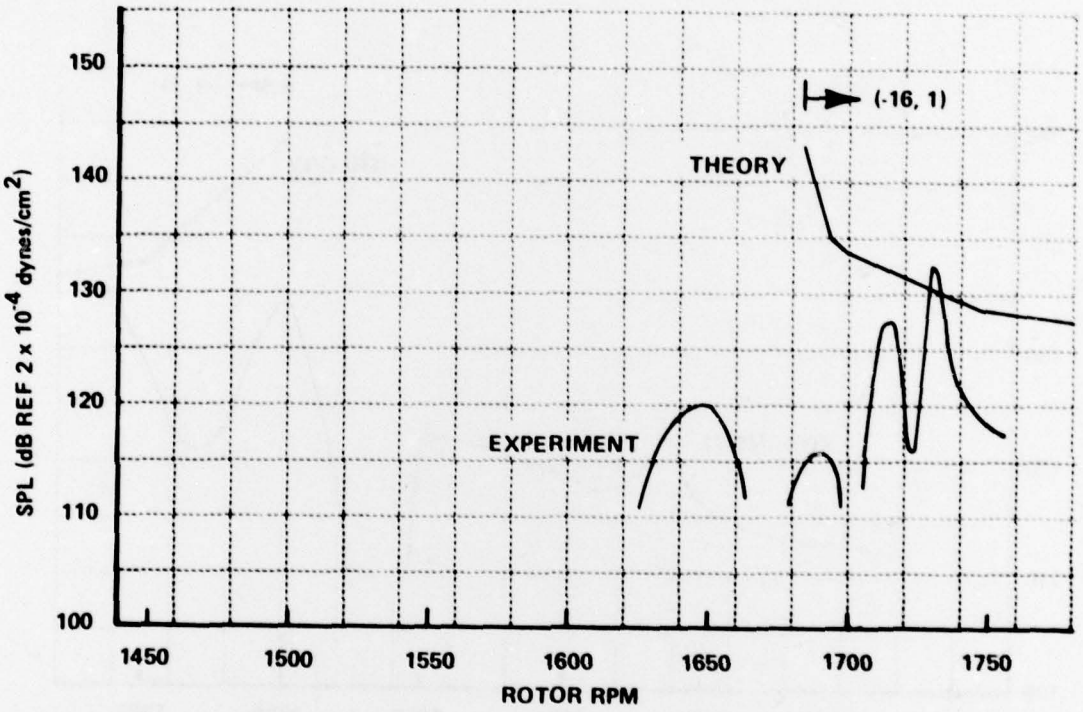

b) 2nd HARMONIC

Figure 31 COMPARISON OF THEORETICALLY PREDICTED SPL WITH EXPERIMENT; STATOR STAGGER ANGLE = 37.2°

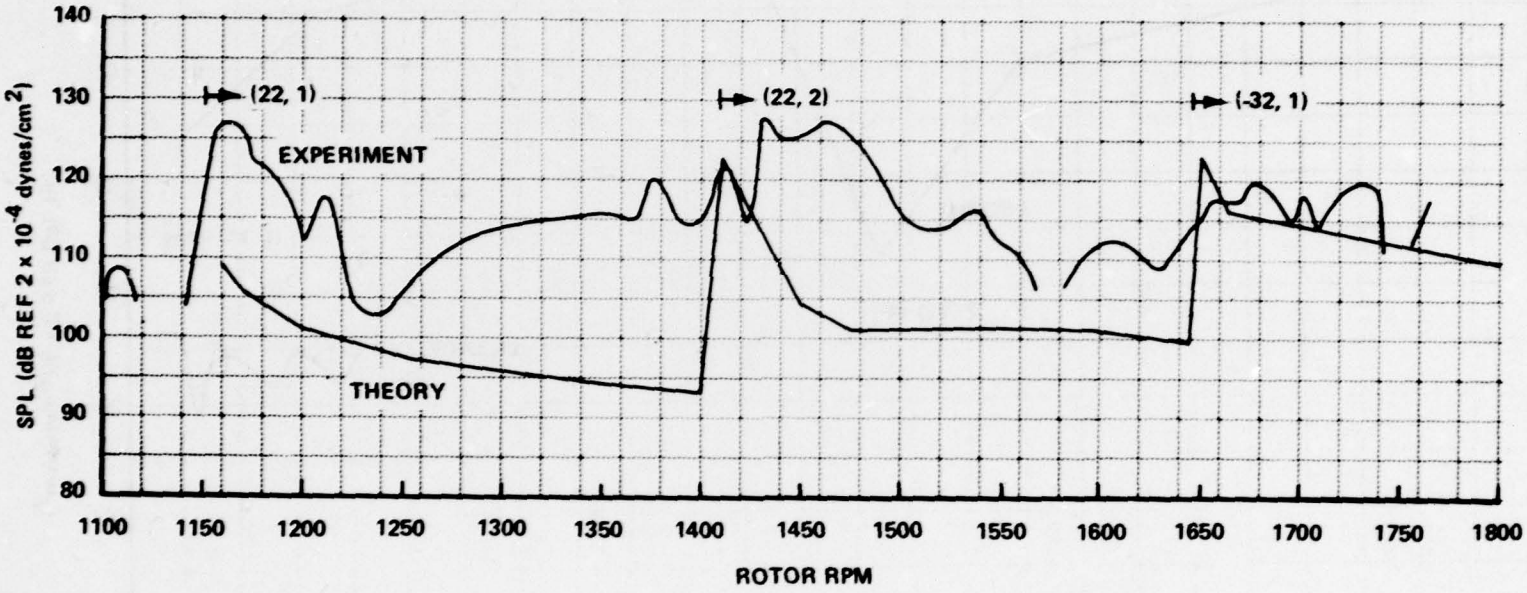

c) 4th HARMONIC

Figure 31 COMPARISON OF THEORETICALLY PREDICTED SPL WITH EXPERIMENT; STATOR STAGGER ANGLE = 37.2°

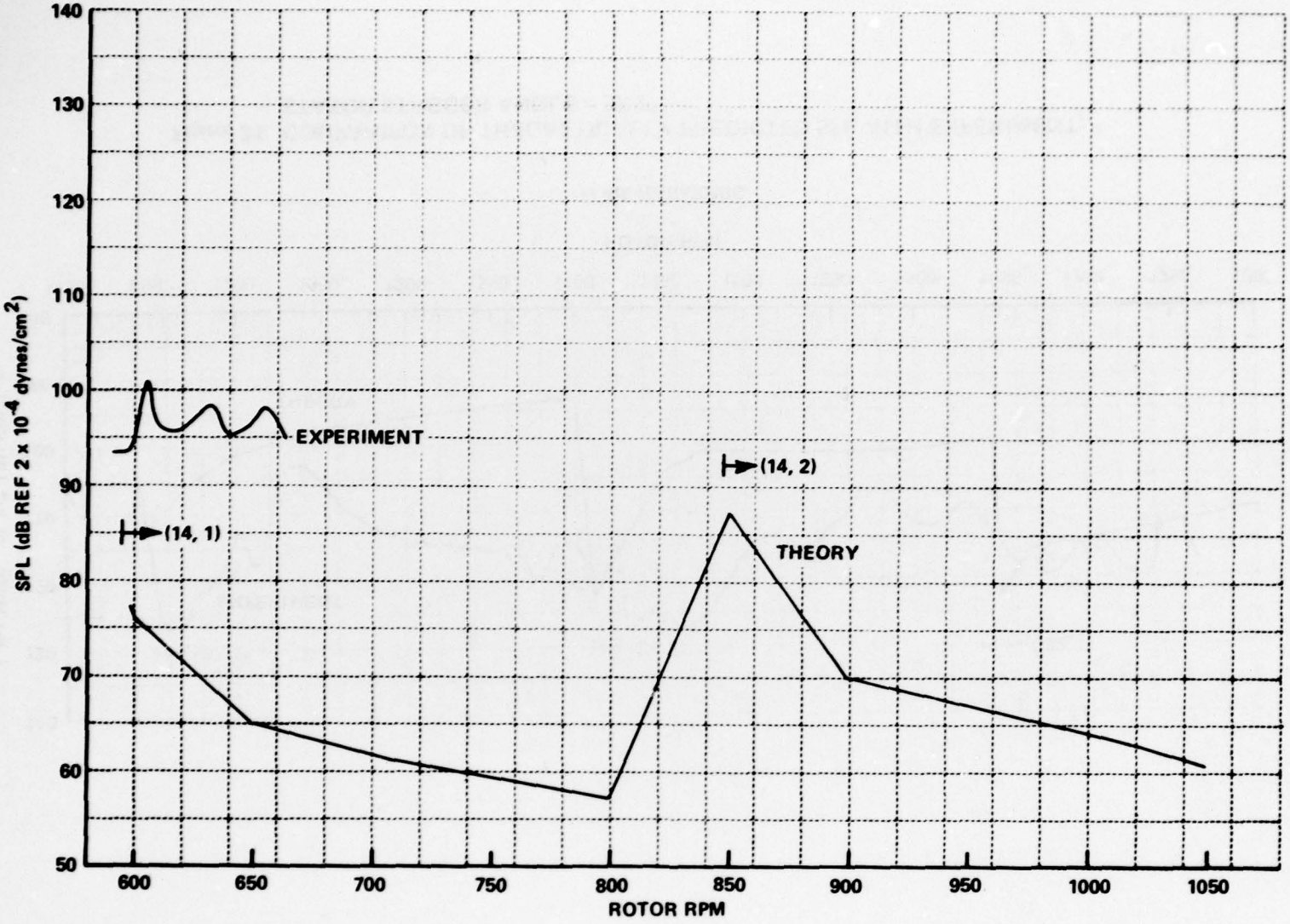

d) 5th HARMONIC

Figure 31 COMPARISON OF THEORETICALLY PREDICTED SPL WITH EXPERIMENT; STATOR STAGGER ANGLE = 37.2°

REFERENCES

1. Lordi, J.A., Homicz, G.F. and Ludwig, G.R., Investigation of Rotating Stall Phenomena in Axial Flow Compressors, Volume II - Investigation of Rotor-Stator Interaction Noise and Lifting-Surface Theory for a Rotor, AFAPL-TR-76-48, June 1976.

2. McCune, J.E., The Three-Dimensional Flow Field of an Axial Compressor Blade Row - Subsonic Transonic, and Supersonic, Ph.D. Thesis, Cornell University, 1958.

3. McCune, J.E., "A Three-Dimensional Theory of Axial Compressor Blade Rows - Application in Subsonic and Supersonic Flows," Journal of the Aeronautical Sciences, Vol. 25, No. 9, Sept. 1958, pp. 544-560.

4. McCune, J.E., "The Transonic Flow Field of an Axial Compressor Blade Row," Journal of the Aeronautical Sciences, Vol. 25, No. 10, Oct. 1958, pp. 616-626.

5. Okurounmu, O., and McCune, J.E., "Three-Dimensional Vortex Theory of Axial Compressor Blade Rows at Subsonic and Transonic Speeds," AIAA Journal, Vol. 8, No. 7, July 1970, pp. 1275-1283.

6. Okurounmu, O. and McCune, J.E., Transonic Lifting Surface Theory for Axial Flow Compressors, United Aircraft Research Laboratories Report K213580-1, March 1971.

7. Okurounmu, O., and McCune, J.E., "Lifting Surface Theory of Axial Compressor Blade Rows: Part I - Subsonic Compressor; Part II - Transonic Compressor," AIAA Journal, Vol. 12, No. 10, Oct. 1974, pp. 1363-1380.

8. McCune, J.E., and Dharwadkar, S.P., Lifting-Line Theory for Subsonic Axial Compressor Rotors, MIT Gas Turbine Laboratory GTL Report No. 110, July 1972.

9. Falcao, A.F. de O., Three-Dimensional Flow Analysis in Axial Turbomachines, Ph.D. Thesis, Eng. Dept., Cambridge University, Aug. 1970.

10. Namba, M., Small Disturbance Theory of Rotating Subsonic and Transonic Cascades, 1st Int. Symp. on Air-Breathing Engines, Marseille, France, June 1972.

11. Namba, M., Lifting Surface Theory for a Rotating Subsonic or Transonic Blade Row, Aeronautical Research Council R & M No. 3740, Nov. 1972, Great Britain.

12. Salaun, P., "Calculation of the Unsteady Subsonic Aerodynamic Pressures on Compressor Blades," La Recherche Aerospatiale, No. 1, Jan. - Feb. 1973, pp. 41-49.

13. Salaun, P., Unsteady Aerodynamic Pressure on an Annular Cascade in Subsonic Flow, Office National d'Etudes et de Recherches Aerospatiale Publication No. 158, 1974. Translated as European Space Agency Technical Translation ESA-TT-173, July 1975.

14. Erickson, J.C., Lordi, J.A., and Rae, W.J., On the Transonic Aerodynamics of a Compressor Blade Row, Cornell Aeroanutical Laboratory Report CAL No. AI-3003-A-1, Oct. 1971.

15. Tyler, J.M., and Sofrin, T.G., "Axial Flow Compressor Noise Studies," SAE Transactions, Vol. 70, 1962, pp. 309-332.

16. Ashley, H. and Landahl, M., Aerodynamics of Wings and Bodies, Addison-Wesley, Reading, Mass., 1965, pp. 132-133.

17. Pistolesi, E., On the Calculation of Flow Past an Infinite Screen of Thin Airfoils, NACA TM 968, 1941.

18. Woolard, H.W., "A Note on the Subsonic Compressible Flow About Airfoils in a Cascade," Journal of Aeronautical Sciences, Vol. 17, No. 6, June 1950, pp. 379-381.

19. Rae, W.J., "Calculations of Three-Dimensional Transonic Compressor Flowfields by a Relaxation Method", Journal of Energy, Vol. 1, No. 5, Sept. - Oct. 1977, pp. 284-296.

20. Rae, W.J. and Lordi, J.A., A Study of Inlet Conditions for Three-Dimensional Transonic Compressor Flows, Naval Air Systems Command, June 1978.

21. Rae, W.J., Theoretical Studies of Three Dimensional Transonic Flow Through a Compressor Blade Row, Air Force Office of Scientific Research Contract No. F49620-78-C-0057, 2nd Quarterly Progress Report, July 1, 1978 - Sept. 30, 1978.

22. Lordi, J.A., Report on a Study of Noise Generation by a Rotating Blade Row in an Infinite Annulus, Cornell Aeronautical Laboratory Report CAL No. AI-2836-A-1, or AFOSR TR-71-1485, May 1971.

23. Watson, G.N., A Treatise on the Theory of Bessel Functions, 2nd Ed., Cambridge University Press, London, 1966.

24. Abramowitz, M., and Stegun, I.A., ed., Handbook of Mathematical Functions with Formulas, Graphs, and Mathematical Tables, Dover, 1965.

25. Michels, T.E., The Backward Recurrence Method for Computing the Regular Bessel Function, NASA TN D-2141, 1964.

26. Luke, Y.L., On Generating Bessel Functions by Use of the Backward Recurrence Formula, Aerospace Research Laboratories, Wright-Patterson Air Force Base, ARL 72-0030, 1972.

27. O'Hara, H., and Smith, F.J., "The Evaluation of Definite Integrals by Internal Subdivision," Computer Journal, Vol. 12, 1969, pp. 179-182.

28. Namba, M., "Three-Dimensional Analysis of Blade Force and Sound Generation for an Annular Cascade in Distorted Flows", Journal of Sound and Vibration, Vol. 50, No. 4, 1977, pp. 479-508.

29. Kobayashi, H., Three Dimensional Effects on Pure Tone Fan Noise Due to Inflow Distortion, AIAA Paper 78-1120, AIAA 11th Fluid and Plasma Dynamics Conference, July 10-12, 1978, Seattle, Washington.

30. Cochran, J.A., "Remarks on the Zeroes of Cross-Product Bessel Functions", Journal of the Society of Industrial and Applied Mathematics, Vol. 12, No. 3, September 1964, pp. 580-587.

31. Ludwig, G.R., Nenni, J.P. and Erickson, J.C., Jr., Investigation of Rotating Stall Phenomena in Axial Flow Compressors, Volume I - Basic Studies of Rotating Stall, AFAPL-TR-76-48, June 1976.

32. Peterson, A.P.G. and Gross, E.E., Jr., Handbook of Noise Measurement (Sixth Edition), General Radio Company, Massachusetts, 1967.

33. Osborne, C., "Compressible Unsteady Interactions Between Blade Rows", AIAA Journal, Vol. 11, No. 3, March 1973, pp. 340-346.

34. Kemp, N.H. and Sears, W.R., "Aerodynamic Interference Between Moving Blade Rows", Journal of Aeronautical Sciences, Vol. 20, No. 9, Sept. 1953, pp. 585-598.

35. Kemp, N.H. and Sears, W.R., " The Unsteady Forces Due to Viscous Wakes in Turbomachines", Journal of Aeronautical Sciences, Vol. 22, No. 7, July 1955, pp. 478-483.

36. Osborne, C., "Unsteady Thin Airfoil Theory for Subsonic Flow", AIAA Journal, Vol. 11, No. 2, February 1973, pp. 205-209.

37. Ludwig, G.R., Nenni, J.P. and Arendt, R.H., Investigation of Rotating Stall in Axial Flow Compressors and the Development of a Prototype Rotating Stall Control System, AFAPL-TR-73-45, May 1973.

38. Ludwig, G.R. and Nenni, J.P., Basic Studies of Rotating Stall In Axial Flow Compressors, AFAPL-TR-79-2083 September 1979.

39. Silverstein, A., Katzoff, S. and Bullivant, W.K., Downwash and Wake Behind Plain and Flapped Airfoils, NACA TR 651, 1939.

40. Raj, R. and Lakshminarayana, B., "Characteristics of the Wake Behind a Cascade of Airfoils", Journal of Fluid Mechanics, Vol. 61, No. 4, December 1973, pp. 707-730.

41. Kerrebrock, J.L., Epstein, A.H., Haines, D.M., and Thompkins, W.T., "The MIT Blowdown Compressor Facility", ASME Transactions, Journal of Engineering for Power, Vo. 96, No. 4, Oct. 1974, pp. 394-406.

42. Raj, R. and Lakshminarayana, B., "Three Dimensional Characteristics of Turbulent Wakes Behind Rotors of Axial Flow Turbomachinery", ASME Transactions, Journal of Engineering for Power, Vol. 98, No. 2, April 1976, pp. 218-228.

43. Reynolds, B., Lakshminarayana, B. and Ravindranath, A., Characteristics of the Near Wake of a Compressor Rotor, AIAA Paper 78-1141, AIAA 11th Fluid and Plasma Dynamics Conference, Seattle, Washington, July 10-12, 1978.

*U.S.Government Printing Office: 1979 — 657-084/248